Josephson Junction Arrays with d-wave-induced π-phase-shifts

Josephson junction arrays with d-wave-induced π-phase-shifts

§ Ph.D. thesis, Universiteit Twente, Enschede, The Netherlands

§ Ariando

The work described in this thesis was carried out in the Low Temperature Division of the Faculty of Science & Technology and the MESA$^+$ Research Institute at the Universiteit Twente, in collaboration with IBM T.J. Watson Research Center, Yorktown Heights, USA, and Universität Tübingen, Germany. The project was supported by the Dutch Foundation for Fundamental Research on Matter (FOM), the Royal Dutch Academy of Arts and Sciences (KNAW), the Netherlands Organization for Scientific Research (NWO), and the European Science Foundation (ESF) PiShift programme.

Ph.D. committee:

prof.dr. A. Bliek, Universiteit Twente, NL
dr. J.R. Kirtley, IBM T.J. Watson Research Center, USA
prof.dr. F. Tafuri, University of Napoli, IT
prof.dr. S.A. van Gils, Universiteit Twente, NL
prof.dr. D.H.A. Blank, Universiteit Twente, NL
prof.dr. H. Hilgenkamp, Universiteit Twente, NL
prof.dr. H. Rogalla, Universiteit Twente, NL

Typeset using LaTeX 2_ε

Cover design by Novliza Ariando

Printed by Wöhrmann Print Service, The Netherlands

ISBN 90-365-2195-5

JOSEPHSON JUNCTION ARRAYS WITH d-WAVE-INDUCED π-PHASE-SHIFTS

PROEFSCHRIFT

ter verkrijging van
de graad van doctor aan de Universiteit Twente,
op gezag van de rector magnificus,
prof.dr. W.H.M. Zijm,
volgens besluit van het College voor Promoties
in het openbaar te verdedigen
op donderdag 12 Mei 2005 om 15.00 uur

door

Ariando
geboren op 8 April 1976
te Sijunjung, West Sumatera, Indonesia

Dit proefschrift is goedgekeurd door de promotoren

prof.dr. H. Rogalla
prof.dr. H. Hilgenkamp

Contents

1 Introduction **1**

2 Josephson junctions with $d_{x^2-y^2}$-wave-induced π-phase-shifts **7**
2.1 Superconductivity 7
2.1.1 Phenomenological description 7
2.1.2 Flux quantization 8
2.2 The high-T_c cuprate superconductors 10
2.3 Josephson junctions and SQUIDs 13
2.3.1 Josephson relations 13
2.3.2 Josephson coupling energy 14
2.3.3 Static phase distribution: effect of a magnetic field 14
2.3.4 SQUIDs 17
2.4 Josephson junctions with π-phase-shifts 19
2.4.1 The symmetry of the order parameter in superconductors . . . 19
2.4.2 $d_{x^2-y^2}$-wave-induced π-phase-shifts 24
2.4.3 The magnetic field dependencies of the critical currents 25
2.4.4 State of the art 26
2.4.5 Terminology: 0- and π-facets 29

3 Fabrication aspects and measurement techniques **31**
3.1 Fabrication aspects 31
3.1.1 The high-T_c cuprate thin-films 34
3.1.2 Interfacing the high-T_c and the low-T_c superconductors 36
3.1.3 The Niobium thin-films 39
3.2 Measurement techniques 39
3.2.1 Transport measurements 39
3.2.2 Low temperature scanning electron microscopy 40
3.2.3 Scanning SQUID microscopy 41

4 Arrays of $YBa_2Cu_3O_{7-\delta}$/Nb Josephson junctions in a zigzag configuration **45**
4.1 Introduction 45
4.2 $YBa_2Cu_3O_{7-\delta}$/Au/Nb zigzag junctions 46
4.3 Magnetic field dependence of the critical current 47
4.3.1 Introduction 47

4.3.2 Measurement results . . . 49
4.4 Imaging of the local currents by LTSEM . . . 53
4.4.1 Introduction . . . 53
4.4.2 Measurement results . . . 53
4.5 Concluding remarks . . . 57

5 Pairing symmetry tests on $Nd_{2-x}Ce_xCuO_{4-y}$ utilizing zigzag junctions 59
5.1 Introduction . . . 59
5.2 $Nd_{2-x}Ce_xCuO_{4-y}$/Au/Nb zigzag junctions . . . 61
5.3 Measurement results . . . 62
5.4 Concluding remarks . . . 67

6 Half-integer flux quantum effects in 1-d π-ring arrays 69
6.1 Introduction . . . 69
6.1.1 Spontaneous flux in π-rings . . . 70
6.1.2 First direct observation . . . 73
6.1.3 Spontaneous-flux in zigzag junctions . . . 74
6.2 Measurement results . . . 78
6.2.1 The $I_c(H_a)$-dependencies . . . 78
6.2.2 Magnetic imaging by scanning SQUID microscopy . . . 81
6.2.3 Half magnetic-flux quanta in background fields . . . 85
6.2.4 Coupling of half magnetic-flux quanta in connected versus unconnected structures . . . 87
6.3 Concluding remarks . . . 91

7 Ordering and manipulation of half flux-quanta in 2-d π-ring arrays 93
7.1 Introduction . . . 93
7.1.1 The superconducting π-ring as an Ising spin . . . 93
7.1.2 Two dimensional antiferromagnetic Ising spins . . . 97
7.2 Measurement results . . . 100
7.2.1 Magnetic imaging of triangular π-ring arrays . . . 100
7.2.2 Imaging of the half-vortices arrangement in frustrated versus unfrustrated arrays . . . 108
7.3 Concluding remarks . . . 115

Bibliography 117

Summary 129

Samenvatting 133

Acknowledgements 137

List of publications 139

Chapter 1

Introduction

Nowadays the fascinating shape of 'the Möbius Loop', a twisted loop named after the astronomer and mathematician August Ferdinand Möbius, has become a universal symbol in life. The artist John Galleher [1] described 'The Möbius Loop is symbolic of eternal change within stillness itself. It represents the process of transforming waste materials into useful resources, a willingness to move with the constantly changing cycles in our life process, transforming our challenges into useful solutions. The Möbius Loop is an expression of non-duality. It reveals the unity of all polarities, creating a state of oneness, joining the whole and the part, the masculine and the feminine, expansion and contraction, spirit and matter. Everything is one and nothing can be separated from anything else. All is completely intertwined, infinitely. This geometric form stimulates our inter-related connection with nature, awakening to the beauty and power of life.'

Physically, the Möbius Loop is a one-sided nonorientable surface obtained by cutting a closed band into a single strip, giving one of the two ends thus producing a π (180°) twist, and then reattaching the two ends. Figure 1.1 presents an artistic sketch of the Möbius Loop, on which ants are able to walk on its whole surface indefinitely since there is no edge in the direction of their movement.

In the field of superconductivity, the Möbius Loop also finds its place, and it presents many fascinating effects. A 'superconducting Möbius Loop' can be formed when the phase of the superconducting wave function is twisted by π, which can be realized when a high temperature superconductor is combined with a low temperature superconductor to form a ring comprising multiple Josephson junctions, *e.g.*, as depicted in Fig. 1.2. This is possible because it turns out that the pair wave function in the high temperature superconductors has a $d_{x^2-y^2}$-wave symmetry with a phase change of π along orthogonal directions in momentum space, instead of an s-wave symmetry with a constant phase in all directions as in conventional metallic superconductors. With one of the ring electrodes having a $d_{x^2-y^2}$-wave symmetry, the junction oriented in one direction experience an additional π-phase difference compared to that oriented in the other direction, as seen in Fig. 1.2. Since there is thus a phase shift of π inherently built in the ring, it is frequently called a π-ring. Such structures were first proposed by Geshkenbein, Larkin, and Barone [2, 3], and later

Figure 1.1: An artistic sketch of the Möbius Loop. M.C. Escher's "Moebius Strip II" © 2004 The M.C. Escher Company - Baarn. All rights reserved. Used by permission. www.mcescher.com.

relating to the $d_{x^2-y^2}$-wave symmetry in the high-T_c superconductors by Sigrist and Rice [4].

One of the most fascinating effects presented by the π-ring is the spontaneous formation of a half magnetic flux quantum in its ground state [5]. Until recently, the formation of individual half-flux quanta could be shown only in very challenging experiments, relying on difficult-to-prepare, and expensive, tri- or tetracrystalline substrates. Nevertheless, there has been a great deal of speculation about further possible applications of the half-flux quantum effect, *e.g.*, in the development of superconducting (quantum)-electronics and in investigations on magnetic effects in specific geometries. The experimental activities towards this have been limited, to a great extent because of the difficulties in fabricating multiple fractional flux quanta in proximity to one another.

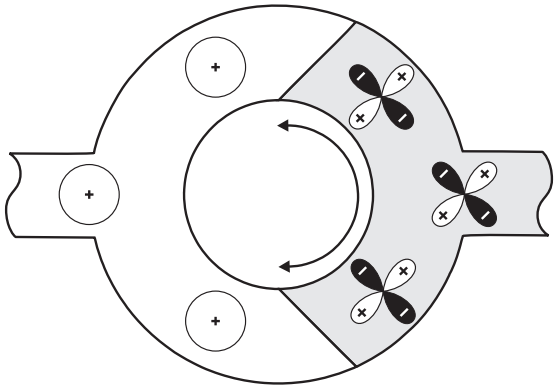

Figure 1.2: Schematic representation of the Möbius superconducting loop.

Multiple π-rings placed controllably at arbitrary positions would enable more detailed and systematic studies on the order parameter symmetry and the formation of spontaneous flux quanta, and their effects on Josephson devices, as well as the realization of theoretically proposed elements for superconducting (quantum) electronics [6–8]. For this, sufficient flexibility and control are required in the positioning of the junctions, and to couple one junction to another. A suitable way to achieve this is with a planar array of Josephson junctions realized with an all-thin-film process using ramp-type junctions [9] between high-T_c and low-T_c superconductors [10, 11].

The first coupled Josephson Junctions has been realized when Jaklevic and coworkers [12] placed a Formvar spacer between their two tin-oxide-tin junctions and observed quantum interference effects between the currents flowing through those separate junctions. It is unlikely however that they fully imagined the importance and the widespread interest that such coupled Josephson junctions would assume in the years to come. Arrays of Josephson junctions, coupled to each other via superconducting phases or vortex interactions, constitute today a major research area within superconductivity [13]. With available standard photolithographic techniques, it is a relatively an easy matter to deposit superconducting islands, micrometer sized and of well-defined shape, onto an appropriate substrate to allow the study of collective Josephson effects, the interaction of the vortex lattices, and superconductivity in two dimensions. For basic two dimensional physics, the arrays have become tools for experimental investigations of phase transitions, the Ising model, frustration and disorder, to mention but a few of the more important ones. While one should realize the complexity to fabricate three-dimensional (3D) arrays, and the relevance of such 3D-arrays as model systems for bulk granular superconductors, it is fair to say that today's most popular arrays are planar. On the other hand, although the phase coherence of the superconducting wave function between a high-T_c and a low-T_c superconductor has been demonstrated [14], the properties and potential of planar hybrid Josephson junctions combining these two superconductors have hardly been explored.

Modifying the ramp-junction technology [11, 15] arises the ability to controllably prepare high-quality Josephson junction structures connecting a high-T_c and a low-T_c superconductor, and enables the realization of planar arrays of π-rings. In this thesis, Josephson junction arrays have been first investigated in a zigzag configuration, employing a high-T_c and a low-T_c superconductor. Originally, the gene of this structure was born when Hilgenkamp, Mannhart, and co-workers squeezed their brains to understand highly anomalous magnetic field dependencies of the critical currents observed in their high-T_c grain boundary Josephson junctions, which could not be explained from standard Josephson models [16]. The fundamental physics relating to the pairing symmetry in the high-T_c cuprate superconductors and to the faceting in the grain boundaries were found to explain these anomalous patterns. A challenging task was arisen to model the faceting in the grain boundaries in a controllable manner. Motivated by this and allowed by the recent technology available in our group to fabricate high-quality contacts between a low-T_c superconductor and a high-T_c cuprate superconductor [10, 11], the faceting in high-T_c grain boundaries has been modeled and studied in controllable zigzag Josephson arrays. Even more interestingly, these arrays were shown to be viable structures to resolve controversial issues regarding the pairing symmetry in the high-T_c cuprate superconductors.

The zigzag Josephson array is basically a linear array of π-rings, and it can be extended to various one- and two-dimensional π-ring arrays in different configurations, enabling a study of many novel intriguing physical phenomena. This includes *e.g.*, fundamental investigations on order parameter symmetry in the high-T_c cuprates [17, 18], half magnetic-flux quantum effects [5, 19], and correlation in two dimensional Ising models [19, 20]. Coupled Josephson junctions with $d_{x^2-y^2}$-wave-induced π-phase-shifts also seem to have large potential applications, *e.g.*, to realize the theoretically proposed elements for superconducting (quantum) electronics such as complementary Josephson circuits [6] and qubits [7, 21]. Some promising steps for further works in realizing these devices have been shown in [21–23].

In this thesis, the realization of Josephson junction arrays with $d_{x^2-y^2}$-wave-induced π-phase-shifts utilizing high-T_c and low-T_c contact technology will be described. Combining these two types of superconductors allows one to realize the so-called π-ring, as briefly introduced earlier. This π-ring is the basic element of Josephson array-structures discussed in this thesis. Combining π-loops in various novel (quantum)-structures allows one to study many intriguing effects.

In Chapter 2, a brief introduction on superconductivity and superconducting materials and devices will be first given. In the same chapter, the $d_{x^2-y^2}$-wave-induced π-phase-shifts in Josephson junctions will be discussed. This includes an introduction on the pairing symmetry in high-T_c superconductors and how π-phase shifts can arise in Josephson structures involving $d_{x^2-y^2}$-wave superconductors. Some structures with $d_{x^2-y^2}$-wave-induced π-phase-shifts will be introduced. Chapter 3 will present the fabrication procedures in order to realize high-quality thin-film ramp-type Josephson contacts between high-T_c and low-T_c superconductors. Measurement techniques used in the experiments will also be discussed in this chapter.

The first Josephson junction array configuration discussed in this thesis is the zigzag structure. In this structure, the facets in the junctions experience a 0- or π-additional phase in an alternating fashion. This basically presents a systematic

model for faceting in the high-T_c grain boundaries. The results show that this type of junction behaves in similar ways as the asymmetric 45° [001]-tilted grain boundary junctions, and even more important simultaneously confirms that the predominant pairing symmetry in $YBa_2Cu_3O_{7-\delta}$ is $d_{x^2-y^2}$-wave. This will be discussed in Chapter 4. Furthermore, the results of Josephson current imaging using low temperature scanning electron microscopy on zigzag Josephson junctions will be demonstrated. In Chapter 5, this structure was employed as a tool to phase-sensitively test the order parameter symmetry in the electron-doped compound $Nd_{2-x}Ce_xCuO_{4-y}$.

Under certain conditions, the π-loops are characterized by the spontaneous generation of half magnetic-flux quanta. These half flux quantum effects and their coupling in one dimensional (1D) and in two dimensional (2D) systems will be discussed in Chapter 6 and 7, respectively.

Chapter 2

Josephson junctions with $d_{x^2-y^2}$-wave-induced π-phase-shifts

The Josephson junction is a central element in many studies on superconductivity, and in the applications of this macroscopic quantum state. In the high temperature cuprate superconductors, experiments on Josephson junctions have established the superconducting order parameter in this cuprate material having predominantly $d_{x^2-y^2}$-wave symmetry, providing the opportunity to realize novel Josephson quantum-structures, characterized by built-in π-phase-shifts. Such Josephson structures are of interest for basic studies and have also been proposed as new components in superconducting (quantum)-electronics.

In this chapter, a brief introduction to the superconductivity and superconducting materials and devices will be given first. This first section will partly follow Refs [24] and [25]. Later, the symmetry of the order parameter in superconductors will be discussed, followed by an introduction to how a π-phase shift is obtained in connected Josephson arrays. Finally, the state of the art of the Josephson structures with $d_{x^2-y^2}$-wave-induced π-phase-shifts will be listed.

2.1 Superconductivity

2.1.1 Phenomenological description

Superconductivity is one of the examples of macroscopic quantum systems [26], and is the result of a weak positive correlation between two electron states of opposite spin and momentum (Cooper pairs in BCS theory) through interaction with lattice vibrations (phonons). Because of the anti-parallel combination of the spin and the angular momentum of the electrons in each pair, the total angular momentum vanishes and the Cooper pairs act as bosonic particles. At zero temperature, all Cooper pairs are Bose-condensed into the superconducting electronic ground state.

In a phenomenological description of the superconducting state, introduced by Ginzburg and Landau, these Cooper pairs form a superfluid condensate that can be described by a single wave function

$$\Psi(\mathbf{r}) = |\Psi(\mathbf{r})|\, e^{i\varphi(\mathbf{r})} \tag{2.1}$$

characterized by an amplitude $|\Psi(\mathbf{r})|$ and a phase $\varphi(\mathbf{r})$. The quantity $|\Psi(\mathbf{r})|^2$ is a measure of the local density of the Cooper pairs, n_s. The phase $\varphi(\mathbf{r})$ is coherent over a macroscopic distance, resulting in observable macroscopic quantum mechanical phenomena relating to superconductivity, such as the vanishing of the electrical resistance when the superconducting material is cooled below its critical temperature T_c. A characteristic distance, over which $\Psi(\mathbf{r})$ can vary without undue energy increase, is called the coherence length, $\xi(T)$, which is temperature and material dependent.

In addition to the disappearance of resistance in the current transport, another intrinsic characteristic property of the superconducting state is the Meissner effect. This implies that the magnetic induction $\mathbf{B} = \mathbf{0}$ well inside the superconductor when it is cooled below T_c (the magnetic flux is expelled from the interior of the superconductor). This is due to the current on the surface which gives rise to the magnetization of $\mathbf{M}$ so that $\mathbf{B} \sim \mathbf{M} + \mathbf{H} = \mathbf{0}$, where $\mathbf{H}$ is the applied magnetic field. The thickness of the region, measured from the surface, through which the supercurrents flow is called the London penetration depth $\lambda(T)$. A magnetic field penetrating into a superconductor decays exponentially over this characteristic length-scale from the surface.

2.1.2 Flux quantization

The long-range quantum phase coherence of the pair wave function results in a flux quantization in a superconducting loop. With this, magnetic flux Φ threading through a superconducting ring is quantized in multiples of the flux quantum

$$\Phi_0 = \frac{h}{2e} = 2.07 \times 10^{-15} \text{ Wb} \tag{2.2}$$

The flux quantization as a result of a single-valuedness of the pair wave function is easily seen and derived from the Ginzburg-Landau's differential equations.

In the basic postulate of Ginzburg & Landau, the free energy density f can be expanded in a series in terms of Ψ and the vector potential $\mathbf{A}$ of the form [24]

$$f = \alpha|\Psi|^2 + \frac{\beta}{2}|\Psi|^4 + \frac{1}{2m^*}\left|\left(\frac{\hbar}{i}\nabla - \frac{e^*}{c}\mathbf{A}\right)\Psi\right|^2 + \frac{h^2}{8\pi} \tag{2.3}$$

The parameter α is temperature dependent as $\alpha(t) = \alpha_0(t-1)$, $t = T/T_c$, and β is a constant. The constant m^* and e^* are the effective mass and charge of the Cooper pairs, respectively. Here, $e^* = 2e$, where e is the charge of an electron. The total free energy is given by the volume integral of Eq. 2.3, $F = \int f dV$. When fields, currents, or gradients are imposed, $\Psi(\mathbf{r})$ adjusts itself to minimize the overall free energy. Minimizing this energy F with respect to Ψ and $\mathbf{A}$ leads to the Ginzburg-Landau

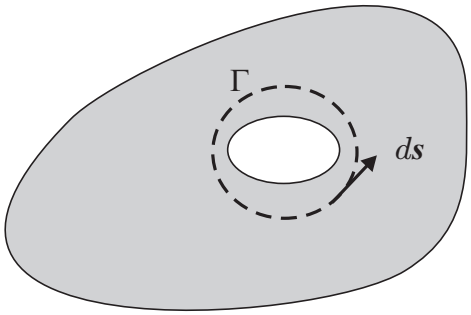

Figure 2.1: Contour of integration within a superconducting loop.

equations [24]

$$\alpha|\Psi| + \beta|\Psi|^2\Psi + \frac{1}{2m^*}\left(\frac{\hbar}{i}\nabla - \frac{e^*}{c}\mathbf{A}\right)^2\Psi = 0 \tag{2.4}$$

and

$$\mathbf{J} = \frac{e^*\hbar}{2m^*i}(\Psi^*\nabla\Psi - \Psi\nabla\Psi^*) - \frac{e^{*2}}{m^*c}\Psi^*\Psi\mathbf{A} \tag{2.5}$$

Substituting the pairing wave function into Eq. 2.5 gives

$$\mathbf{J} = \frac{e^*}{m^*}|\Psi|^2\left(\hbar\nabla\varphi - \frac{e^*}{c}\mathbf{A}\right) \tag{2.6}$$

Integration of this current along a contour Γ enclosing a superconducting material as sketched in Fig. 2.1 leads to

$$\frac{m^*c}{e^{*2}|\Psi|^2}\oint_\Gamma \mathbf{J}\cdot d\mathbf{s} + \oint_\Gamma \mathbf{A}\cdot d\mathbf{s} = \frac{\hbar c}{e^*}\oint_\Gamma \nabla\varphi\cdot d\mathbf{s} \tag{2.7}$$

Applying the conditions that Ψ is a single-valued function, *i.e.*, $\oint_\Gamma \nabla\varphi\cdot d\mathbf{s} = 2n\pi$, and that $\oint_\Gamma \mathbf{A}\cdot d\mathbf{s} = \Phi$ results in

$$\frac{m^*c}{e^{*2}|\Psi|^2}\oint_\Gamma \mathbf{J}\cdot d\mathbf{s} + \Phi = n\Phi_0 \tag{2.8}$$

where $\Phi_0 = hc/2e$ is the flux quantum[1] and n is an integer. For thin superconductors with dimensions comparable to ξ and λ, and with currents at the integration path Γ, both terms on the left hand side of Eq. 2.7 need to be considered. But if the dimensions of the superconductors are much larger than λ, and Γ is deep in the superconductor where the magnetic field is expelled, then $\mathbf{J} = 0$ and the flux threading the loop is simply

$$\Phi = n\Phi_0 \tag{2.9}$$

[1]For simplicity, Gaussian units are used in the derivation, and this leads to $\Phi_0 = hc/2e$. In SI units, $\Phi_0 = h/2e$ (See [24] for Gaussian to SI units conversion).

The quantity on the left hand side of Eq. 2.8 is, in equivalence to the concept introduced first by London, called fluxoid and always quantized in integral multiples of Φ_0. In the Ginzburg-Landau theory it is based simply on the existence of a single-valued complex superconducting wave function $\Psi(\mathbf{r})$.

2.2 The high-T_c cuprate superconductors

Until now a huge number of superconducting materials have been discovered. Based on their transition temperatures from the normal to the superconducting state T_c, two types of superconducting materials are classified. The materials with T_c's above 23.2 K are referred to as high-T_c superconductors. The metallic superconductors are usually called low-T_c superconductors because of their lower T_c's. Only a few metallic superconductors have T_c above the boiling point of liquid helium. Niobium is the mostly used metallic material in electronics applications because of its 9.2 K transition temperature, and its chemical and mechanical stability.

The high-T_c superconductors are characterized by a relatively high transition temperature T_c from the normal conducting to the superconducting state. For some members of this class of materials, the T_c's are even well above the boiling point of liquid nitrogen which is 77 K. Most of the high-T_c superconductors are cuprate compounds.

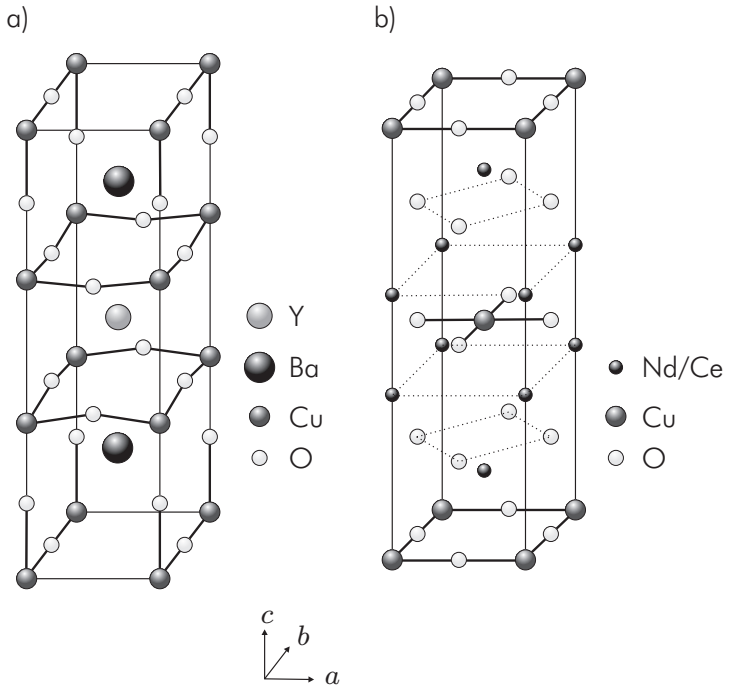

Figure 2.2: Schematic layout of (a) $YBa_2Cu_3O_{7-\delta}$ and (b) $Nd_{2-x}Ce_xCuO_4$ unit cell.

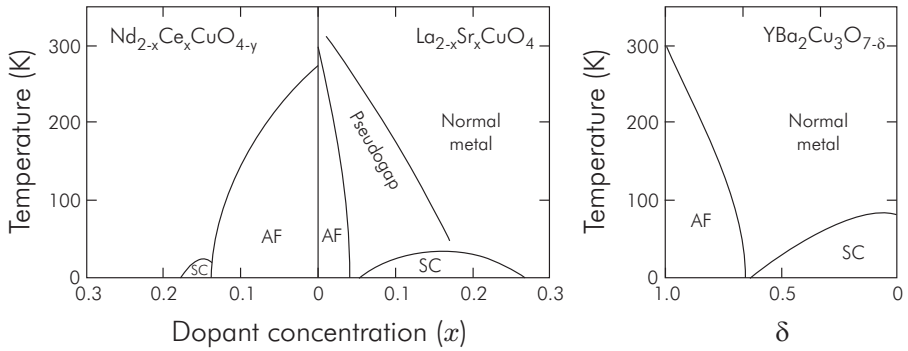

Figure 2.3: (Left) Phase diagram of the electron-doped $Nd_{2-x}Ce_xCuO_4$ and the hole-doped $La_{2-x}Sr_xCuO_4$; (Right) Phase diagram of the hole-doped $YBa_2Cu_3O_{7-\delta}$.

The cuprate superconductors are a class of ceramics which are built from a stacked perovskite-like structure containing CuO_2 planes, separated by layers of other atoms. The CuO_2 plane is a common structural ingredient for the cuprates, and it is strongly believed that superconductivity relates to a process that occurs in these CuO_2 planes, with the other layers (simply) providing the carriers. In Figure 2.2, the unit cell structures of the two cuprate compounds mainly used in this thesis are schematically shown.

Another common property of cuprate superconductors is the presence of antiferromagnetic order at low temperatures in the undoped regime, *i.e.*, when no free charge carriers exist in the planes (see Fig. 2.3). This can be changed drastically upon both ion and oxygen doping resulting in a superconducting phase.

A huge number of combinations can be synthesized by modifying the structure or composition of these materials resulting in large families of cuprate compounds. Relating to the type of charge carriers, the cuprates can be classified into two classes. First is the hole-doped cuprate, in which the charge carriers are the holes (electron vacancies), and second the electron-doped cuprate, in which the charge carriers are electrons. In high-temperature superconductors, the supercurrent flows in CuO_2 conduction layers, while the rest of the unit cell serves as a charge reservoir.

The primary role of vacancies or substituted atoms is to alter the supply of charge carriers in the CuO_2-planes. In the case of the hole-doped compunds, *e.g.* $YBa_2Cu_3O_{7-\delta}$, the excess of oxygen atoms affects the charge balance in the crystal. This is obtained by adding oxygen to $YBa_2Cu_3O_6$, which enters the compound as O^{2-} and forms CuO chains [See Fig. 2.2 (a)].

To maintain the charge balance, electrons are removed from the copper oxide planes, leaving behind holes that carry the supercurrent. These oxygen atoms basically act as dopants, because they increase the number of sites where electrons can reside, and this amounts to creating hole-carriers in the crystal. In the case of the electron-doped compounds, atoms of higher valance are substituted into the lattice in-

	Nb		$YBa_2Cu_3O_{7-\delta}$	$Nd_{2-x}Ce_xCuO_{4-y}$
λ (nm)	39	$\lambda_\parallel$	150	132
		$\lambda_\perp$	1600	-
ξ (nm)	38	$\xi_\parallel$	1.2	8
		$\xi_\perp$	0.3	0.3

Table 2.1: The London penetration depth and coherence length of $YBa_2Cu_3O_{7-\delta}$, $Nd_{2-x}Ce_xCuO_{4-y}$, and Nb [27].

stead of lower-valance atoms. This increases the number of free electrons in the copper oxide planes. For $Nd_{2-x}Ce_xCuO_4$, it is obtained by replacing Nd^{3+} with Ce^{4+}. The phase diagrams of the hole- and electron-doped compounds as a function of dopant concentrations are compared in Fig. 2.3. On the left side is the phase diagram for electron-doped $Nd_{2-x}Ce_xCuO_4$ and hole-doped $La_{2-x}Sr_xCuO_4$. For both, the number of charge carriers is influenced by the substituted atoms. The phase diagram for hole-doped $YBa_2Cu_3O_{7-\delta}$ is shown on the right side of Fig. 2.3.

The unit cell structure of $YBa_2Cu_3O_{7-\delta}$ is orthorhombic and is shown schematically in Fig. 2.2 (a). A key feature of this unit cell is the presence of two layers of CuO_2 separated by a single yttrium atom. Next to this sandwich are two BaO planes where one barium atom is surrounded by four oxygens along the edges of the unit cell. At the ends of the unit cell is a copper oxide region known as the copper oxide chain. $YBa_2Cu_3O_{7-\delta}$ has in-plane lattice constants $a = 3.83$ Å and $b = 3.89$ Å, and the c-lattice constant $c = 11.65$ Å. The missing oxygens are very important in $YBa_2Cu_3O_{7-\delta}$, which results in electron vacancies (hole-doped). These missing oxygens are originally located in the CuO chains at the ends of the unit cell. The subscript δ in the formula indicates that a fraction of the expected oxygens are missing. The maximized-T_c is 92 K at optimal doping ($\delta = 0.16$); with $\delta = 0.60$, superconductivity goes away.

The unit cell structure of the electron-doped $Nd_{2-x}Ce_xCuO_{4-y}$ cuprate is shown schematically in Fig. 2.2 (b). The structure of this compound is body-centered tetragonal at all temperatures. It has nominally vacant apical oxygen atoms. Instead, the out-of-plane oxygen atoms are located directly above and below the in-plane oxygens. In the undoped $Nd_{2-x}Ce_xCuO_{4-y}$, the room temperature in-plane lattice constant is $a = 3.94$ Å, and the c-lattice constant $c = 12.16$ Å. The lattice constants change very slightly with cerium doping. The superconducting phase is obtained by cerium (Ce) doping, which results in an excess of electrons in the CuO_2 planes acting as the charge carriers. This superconducting phase is observed in a relatively narrow cerium

doping range of $0.12 \lesssim x \lesssim 0.17$, with an optimal doping around $x = 0.15$ and a T_c of 22 K.

In Table 2.1, the magnetic penetration depth and the coherence length of $YBa_2Cu_3O_{7-\delta}$ and $Nd_{2-x}Ce_xCuO_{4-y}$ are listed and compared with the low-T_c superconductor Niobium (Nb), which is used as the counter electrode in our Josephson junction structures.

2.3 Josephson junctions and SQUIDs

The macroscopic long-range phase coherence of the pairing wave function is one of the most intriguing features of the superconducting state, resulting for example in the flux quantization such as just described. Another frequently used phenomenon in superconducting electronics is the Josephson effect, which is obtained when the wave function of two superconductors are allowed to weakly interact (weak link) through a barrier (normal metal N, or insulator I, or constriction), in a structure called the Josephson junction (Fig. 2.4). In this case, the Cooper pairs can still tunnel from the first superconductor S1 to the second superconductor S2 through a thin barrier without any bias voltage.

2.3.1 Josephson relations

Josephson [28] predicted that the supercurrent density J for such a junction is related to the phase difference $\Delta\varphi$ of the two superconductors' wave functions at the interface as

$$J = J_c \sin(\Delta\varphi) \tag{2.10}$$

where the critical current density J_c is the maximum supercurrent density that the junction can support, above which the voltage has a finite value. In general, the

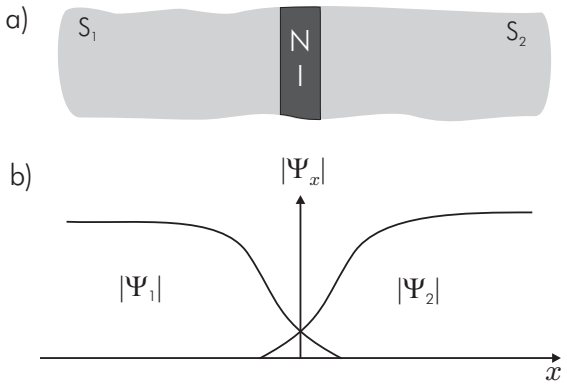

Figure 2.4: (a) A Josephson junction, and (b) the wave function of the first superconductor S1 (Ψ_1) overlaps with the wave function of the second superconductor S2 (Ψ_2) at the interface.

$\sin(\Delta\varphi)$ component can be replaced by any function $f(\Delta\varphi)$, but because the phase must be single-valued, $f(\Delta\varphi)$ has to be 2π periodic. In this thesis, and for most cases, $f(\Delta\varphi) = \sin(\Delta\varphi)$ is used.

Equation 2.10 is called the dc Josephson relation. Applying a constant dc voltage to the tunnel junction, the phase difference $\Delta\varphi$ evolves in time according to the ac Josephson relation

$$\frac{d(\Delta\varphi)}{dt} = \frac{2\pi}{\Phi_0}V \tag{2.11}$$

Consequently, at a constant voltage V the supercurrent through the junction oscillates with the characteristic frequency

$$\frac{d(\Delta\varphi)}{dt}\frac{1}{2\pi V} = \frac{1}{\Phi_0} = 483.6 \text{ MHz}/\mu\text{V} \tag{2.12}$$

The two Josephson equations govern the electrodynamics of the Josephson junction. In particular, the dc Josephson relation gives rise to the nonlinear current flow across the junction barrier and the ac Josephson equation relates the electric field in the junction to the evolution of the phase in time.

2.3.2 Josephson coupling energy

From the dc and ac Josephson relations of Eq. 2.10 and 2.11, respectively, one can derive the coupling free energy stored in the junction by integrating the electrical work $\int JVdt = \int J(\Phi_0/2\pi)d(\Delta\varphi)$ done by a current source in changing the phase. This leads to

$$F = -J_c\frac{\Phi_0}{2\pi}\cos(\Delta\varphi) + C \tag{2.13}$$

Here C is the constant of integration, and $J_c\Phi_0/2\pi = E_J$ is the Josephson coupling energy. From Eq. 2.13, it is clear that the energy is minimal when the phases of the two superconducting wave functions are equal, *i.e.*, $\Delta\varphi = 0$. The critical current gives a measure of how strong the phases of the two superconducting electrodes are coupled through the weak link. This depends on how thin and of what material the barrier is, or, in the case of constriction weak links, on the cross-sectional area and length of the neck.

2.3.3 Static phase distribution: effect of a magnetic field

The extremely high sensitivity of the Josephson current to magnetic fields is the key to the most important applications of the Josephson effect. To ensure the critical current density in the current phase relation is independent of the choice of the vector potential, the gauge invariant phase difference is introduced and is defined as [24]

$$\phi \equiv \varphi_2 - \varphi_1 + \frac{2\pi}{\Phi_0}\int_1^2 \mathbf{A}\cdot d\mathbf{s} \tag{2.14}$$

where $\mathbf{A}$ is the vector potential and the integration is from the first to the second electrode in a Josephson junction. With this, the general current-phase relation becomes

$$J = J_c\sin\phi \tag{2.15}$$

The gauge invariant phase difference is the key to understand the influence of a magnetic field, which can not be treated without introducing the vector potential. On the other hand, when no magnetic field is present, $\mathbf{A} = 0$, ϕ and $\Delta\varphi$ can be used interchangeably.

To derive a relation between the gauge invariant phase difference and the magnetic field passing through a junction, consider two pairs of points Q_1, Q_2 and P_1, P_2 as in Fig. 2.5 (a). Using Eq. 2.14 leads to

$$\phi(P) - \phi(Q) = \frac{2\pi}{\Phi_0}\left[\int_{P_1}^{P_2} \mathbf{A}(P)\cdot d\mathbf{s} - \int_{Q_1}^{Q_2} \mathbf{A}(Q)\cdot d\mathbf{s}\right] \tag{2.16}$$

The magnetic flux through the rectangular contour Γ in Fig. 2.5 is

$$\Phi = \int_S \mu_0\mathbf{H}\cdot d\mathbf{S} = \oint_\Gamma \mathbf{A}\cdot d\mathbf{s} \tag{2.17}$$

$$= \int_{Q_2}^{Q_1} \mathbf{A}\cdot d\mathbf{s} + \int_{Q_1}^{P_1} \mathbf{A}\cdot d\mathbf{s} + \int_{P_1}^{P_2} \mathbf{A}\cdot d\mathbf{s} + \int_{P_2}^{Q_2} \mathbf{A}\cdot d\mathbf{s} \tag{2.18}$$

If the $Q_1 - P_1$ and $Q_2 - P_2$ portions of the contour are deep enough inside the superconductor, where the current density is essentially zero, the second and fourth term in Eq. 2.18 can be neglected. Then combining Eq. 2.16 and Eq. 2.18 leads to

$$\phi(P) - \phi(Q) = \frac{2\pi}{\Phi_0}\Phi \tag{2.19}$$

Simply put, the difference of the phase difference between two points along a junction is proportional to the magnetic flux passing through the junction between the points, including that in the penetration depths of the superconductors. In general, the gradient of the phase difference along the junction as a function of applied fields can be derived by considering a small section dx of the junction. This leads to

$$\frac{\phi(P) - \phi(Q)}{dx} = \frac{2\pi}{\Phi_0}\mu_0 H_z t \tag{2.20}$$

or

$$\nabla\phi = \frac{2\pi}{\Phi_0} t\mu_0\mathbf{H}\times\mathbf{n} \tag{2.21}$$

where $\mathbf{n}$ is a normal vector perpendicular to the junction interface and $t = d + \lambda_1 + \lambda_2$ is the (effective) magnetic thickness, with d the barrier thickness and λ the (effective) London penetration depth of the respective superconducting electrodes. It is noted here that for thin film electrodes, the penetration depth λ needs to be corrected due to the finite electrode thickness [29, 30]. With this, the effective magnetic thickness t becomes

$$t = d + \lambda_1 \coth\left(\frac{d_1}{\lambda_1}\right) + \lambda_2 \coth\left(\frac{d_2}{\lambda_2}\right) \tag{2.22}$$

where d_1 and d_2 are the thickness of the first and second superconducting electrodes, respectively.

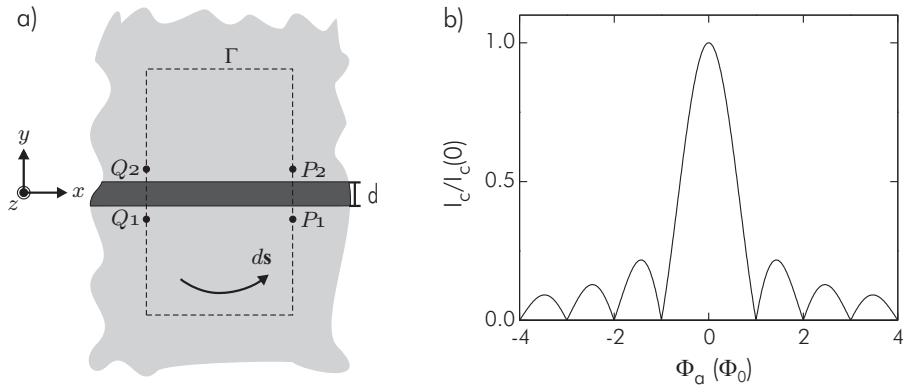

Figure 2.5: a) The integration contour of the vector potential **A** in a Josephson junction used to derive a relation between the enclosed flux and the phase difference. b) Fraunhofer pattern: the magnetic field dependence of the critical current for a uniform junction.

Because the phase difference along the junction can vary by virtue of the presence of a magnetic field passing through the junction, so can the critical currents. The total current which flows through the junction is obtained by integrating the local critical current density over the junction area A. With this,

$$I(H_a) = \int_A J_c(x) \sin\left(\frac{2\pi\mu_0 H_a t x}{\Phi_0} + \phi_0\right) dA \tag{2.23}$$

In general, this can be written in the form [31]

$$I(H_a) = \mathrm{Im}\left[e^{i\phi_0} \int_{-\infty}^{\infty} h J_c(x) e^{i\eta x} dx\right] \tag{2.24}$$

where $\eta = 2\pi\mu_0 t H_a/\Phi_0$, and h is the junction intersection in z direction which is parallel to the applied magnetic field. Thus, $I_c(H_a)$ is the magnitude of the complex Fourier transform of the critical current density

$$I_c(H_a) = \left|\int_{-\infty}^{\infty} h J_c(x) e^{i\eta x} dx\right| \tag{2.25}$$

It is noted here that the symbol H has been replaced by H_a to indicate an externally applied magnetic field, and thus the symbol Φ_a will be used for the applied flux.

In practice, the $I_c(H_a)$-dependence will be more complicated by the contribution of self magnetic field produced by the tunneling current. However, the fields from the tunneling currents can be neglected in the case of a rectangular Josephson junction with dimensions much smaller than a few times the characteristic length scale for the self field effects, the Josephson penetration depth λ_J. Under this condition, Eq. 2.23

can be explicitly integrated, and this results in

$$I_c\left(\frac{\Phi_a}{\Phi_0}\right) = J_c A \left| \frac{\sin\left(\pi \frac{\Phi_a}{\Phi_0}\right)}{\pi \frac{\Phi}{\Phi_0}} \right| \tag{2.26}$$

This expression resembles a magnetic field dependence of the critical current pattern as shown in Fig. 2.5 (b), which is the hallmark of a rectangular junction with homogeneous critical current densities, and is well-known as the Fraunhofer pattern.

The Josephson penetration depth λ_J which is introduced above gives a measure of the distance over which significant variations of the phase difference along the junction can occur, and is defined as

$$\lambda_J = \sqrt{\frac{\hbar}{2e\mu_0 t J_c}} \tag{2.27}$$

Junctions with dimensions a much smaller than λ_J, $a \ll \lambda_J$, are referred to as 'small junctions', and junctions with $a \gg \lambda_J$ as 'large junctions'.

2.3.4 SQUIDs

Since the fluxoid is quantized and the phase difference in the Josephson junction is dependent on the magnetic field, one can build a device which is very sensitive to magnetic fields by integrating Josephson junctions in a superconducting loop. Such devices with one built-in Josephson junction are referred to as rf SQUIDs, and with two Josephson junction as dc SQUIDs. The latter is schematically shown in Fig. 2.6 (a).

In a SQUID, the flux in the loop can be related to the gauge invariant phase-difference ϕ of the integrated Josephson junctions. Assuming that the supercurrent density $\mathbf{J} = 0$ well inside the superconductor, Eq. 2.7 becomes

$$\oint \nabla\varphi \cdot d\mathbf{s} = \frac{2\pi}{\Phi_0} \oint \mathbf{A} \cdot d\mathbf{s} \tag{2.28}$$

For the dc SQUID in Fig. 2.6 (a), by considering the phase drop across the two junctions and that the phase around the loop must be single-valued, integration along the contour Γ yields

$$\begin{aligned} \oint_\Gamma \nabla\varphi \cdot d\mathbf{s} - (\varphi_{1+} - \varphi_{1-}) - (\varphi_{2-} - \varphi_{2+}) = \\ \frac{2\pi}{\Phi_0}\left(\oint_\Gamma \mathbf{A} \cdot d\mathbf{s} - \int_{1-}^{1+} \mathbf{A} \cdot d\mathbf{s} - \int_{2+}^{2-} \mathbf{A} \cdot d\mathbf{s}\right) \end{aligned} \tag{2.29}$$

Using the gauge invariant phase difference defined in Eq. 2.14 and realizing that the contour integral of the vector potential is the flux Φ in the loop leads to

$$\phi_2 - \phi_1 = 2n\pi - 2\pi \frac{\Phi}{\Phi_0} \tag{2.30}$$

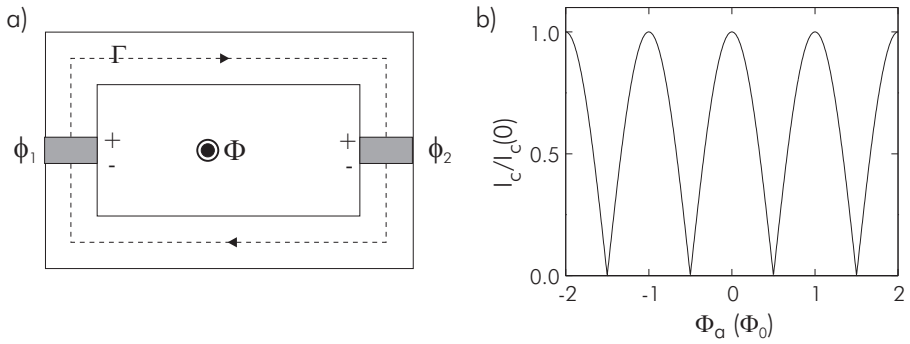

Figure 2.6: (a) Sketch of a dc SQUIDs, (b) the magnetic field dependence of the critical current pattern for a symmetric SQUID ($I_{c,1} = I_{c,2}$), assuming a loop inductance $L = 0$.

The $2n\pi$ component can be excluded since it only represents the 2π periodicity. The total circulating current through the junctions is

$$I_{tot} = I_{c,1}\sin(\phi_1) + I_{c,2}\sin(\phi_2) \tag{2.31}$$

or

$$I_{tot} = I_{c,1}\sin(\phi_1) + I_{c,2}\sin(\phi_1 - \frac{2\pi\Phi}{\Phi_0}) \tag{2.32}$$

Assuming that the loop inductance $L \approx 0$, and that both junctions in the dc SQUID have the same critical current, then by maximizing Eq. 2.32, the critical current for the SQUID can be obtained

$$I_{c,tot}(\Phi) = 2I_c\left|\cos\frac{\pi\Phi}{\Phi_0}\right| \tag{2.33}$$

This dependence of the total critical current on the magnetic field is shown in Fig. 2.6 (b). The total critical current of the SQUID is Φ_0-periodic and zero when the flux in the loop $\Phi = n\Phi_0/2$.

When the inductance of the loop is non-negligible, and there is an unbalance between currents flowing in both arms of the loop, *i.e.*, $I_1 \neq I_2$, resulting in a circulating current $I_{\circlearrowleft} = \frac{1}{2}(I_2 - I_1)$, the total flux is

$$\Phi = \Phi_a + LI_{\circlearrowleft} \tag{2.34}$$

where Φ_a is the applied magnetic flux. In terms of the currents in the junction, this can be expressed as

$$\Phi = \Phi_a + \frac{1}{2}LI_c(\sin\phi_2 - \sin\phi_1) \tag{2.35}$$

assuming identical I_c's for both junctions in the loop. Using Eq. 2.30 gives

$$\phi_2 = \phi_1 - \frac{2\pi}{\Phi_0}\left[\Phi_a + \frac{1}{2}LI_c(\sin\phi_2 - \sin\phi_1)\right] \tag{2.36}$$

To obtain the relation between $I_{c,tot}$ versus applied magnetic flux, these equations must be solved numerically.

The depth of modulation of $I_{c,tot}$ by the magnetic field is an important factor in practical applications. For small thermal noise, an expression for this modulation depth has been given in [32]

$$\Delta I_{c,tot} = \frac{1}{1+\beta_L} I_{c,tot}(\max) \tag{2.37}$$

where $\beta_L = 2\pi L I_c/\Phi_0$ is the screening parameter. The smaller β_L the larger the modulation depth. This parameter is a measure of the importance of self-inductance in the loop, and an indication of the ability of the circulating current to shield the applied magnetic field in the loop.

2.4 Josephson junctions with π-phase-shifts

2.4.1 The symmetry of the order parameter in superconductors

Various physical systems in nature experience phase transitions. The change of order in these phase transitions is conveniently quantified by a parameter called order parameter. The transition from the normal to the superconducting state is characterized by an order parameter $\Psi(\mathbf{r})$, the single superfluid-condensate wave-function, described by Eq. 2.1. This single wave function leads to long range macroscopic phase coherence that is one of the unique signatures of the superconducting state.

The excitations from the superconducting ground state involve mixtures of electron and hole states referred to as quasiparticles. One of the most striking properties of the quasiparticles is that they exhibit an energy gap Δ with respect to the ground-state energy. The energy gap inhibits the creation of excitations in the superconducting state and dominates the low temperature electrical transport and optical properties of superconductors. The gap is most clearly demonstrated and measured by tunneling measurements into superconductors that exhibit a sharp conductance increase at voltage $V = \Delta/e$ [33, 34]. In the microscopic BCS theory, it is predicted that a minimum excitation energy $E_g = 2\Delta(T)$ should be required to break a pair.

Later, Gor'kov [35] linked the Ginzburg-Landau theory and the BCS theory, and showed that the order parameter $\Psi(\mathbf{r})$ is proportional to the energy gap $\Delta(\mathbf{r})$. In momentum space, the order parameter $\Psi(\mathbf{k})$ is related to the gap function $\Delta_\mathbf{k}$ through $\Psi(\mathbf{k}) = \Delta_\mathbf{k}/2E_\mathbf{k}$, where $E_\mathbf{k}$ is the quasiparticle excitation energy, and the gap parameter in state $\mathbf{k}$ is defined to be proportional to the pairing amplitude $\langle c_{\mathbf{k}\uparrow} c_{-\mathbf{k}\downarrow}\rangle$ [24]. Therefore, the use of the pair amplitude $\langle c_{\mathbf{k}\uparrow} c_{-\mathbf{k}\downarrow}\rangle \propto \Delta_\mathbf{k} \propto \Psi(\mathbf{k})$ as the order parameter captures the essence of the macroscopic phase-coherent superconducting state [26].

In BCS theory, it is assumed that the system is isotropic, so that $\Delta_\mathbf{k}$ is independent of $\mathbf{k}$. Because of its spherical form, this symmetry is referred to as s-wave, an analogy to the atomic orbital with a spherical symmetry. In Fig. 2.7 (a), the magnitude and phase of the s-wave order parameter symmetry as a function of angle in momentum space (k-space) are depicted. This symmetry represents almost all low-T_c supercon-

ductors, with the exception of a class of materials referred to as the heavy-fermion superconductors.

On the other hand, all high-T_c cuprate superconductors are characterized by a relatively high ratio of c- to a-axis lattice constants, c/a. In the k-space presentation, this ratio translates into a flattened Brillouin zone possessing the basic symmetry properties of the unit cell of a square (rectangular) lattice [26]. This was supported by the results of band-structure calculations for various cuprates, which all show energy bands predominantly derived from the CuO_2 planes, with no significant dispersion in the c-axis direction.[2] Furthermore, investigations of c-axis charge dynamics and transport have provided strong evidence for charge confinement in the CuO_2 layers [26, 36].

The two dimensional characteristics of the energy bands, which increase with larger c/a ratio, are also obviously seen in the anisotropy of various electrical properties, such as the magnetic penetration depths and the superconducting coherence length [37, 38]. In general, it is now widely believed that for anisotropic materials such as the high-T_c cuprate superconductors, superconductivity basically originates from the CuO_2 layers, and the pairing symmetry is expected to reflect the symmetry of the underlying CuO lattices. In this thesis, therefore, the high-T_c cuprate superconductors are assumed as two-dimensional electronic systems, not as anisotropic three-dimensional systems. They consist of stacks of two-dimensional superconducting CuO_2 layers.

Several pairing mechanism in the high-T_c cuprate superconductors have been proposed, each related to a specific symmetry in the order parameter. The most prominent mechanism was proposed first by Bicker, Scalapino, and White [39], based on the exchange of anti-ferromagnetic spin fluctuations leading to $d_{x^2-y^2}$-wave pairing symmetry. However, the exact pairing mechanism in high-T_c superconductors is thus far not yet established. Although most pairing symmetry tests yielded convincing evidence for a predominantly $d_{x^2-y^2}$-wave order parameter, none of these experiments thus far could rule out a mixed pair state. For example the small difference between the a- and b-direction in the $YBa_2Cu_3O_{7-\delta}$ unit cell may induce an additional real s-wave component to the dominant $d_{x^2-y^2}$-wave order parameter reflecting the asymmetry in the lattice. In addition, for the electron-doped materials, there is still ongoing discussion about possible pairing symmetries in this compound, specifically about the possible pairing symmetry changes with temperature and doping (see Chapter 5 for a more detailed discussion).

In the following, some possible pairing symmetries and their gap function in momentum space are described [34, 40]. In Fig. 2.7, these symmetry functions along with their magnitude and phase are plotted as a function of angle in k-space for the two-dimensional representation.

isotropic s-wave ; $\Delta_{\mathbf{k}} = \Delta_0$. This is a spherical symmetry. The magnitude and phase is constant along all directions in momentum space, *i.e.*, the gap potential $\Delta_{\mathbf{k}}$ is independent of $\mathbf{k}$. [Fig. 2.7 (a)]

[2] See [26] for a complete list of references.

anisotropic s-wave ; $\Delta_{\mathbf{k}} = \Delta_0[\cos k_x - \cos k_y]^4 + \Delta_1$. In this case the phase is constant as in the isotropic s-wave case, but the magnitude is suppressed along the 45° directions. The minimum gap is Δ_1.
[Fig. 2.7 (b)]

extended s-wave ; $\Delta_{\mathbf{k}} = \Delta_0\{(1+\gamma^2)[\cos k_x - \cos k_y]^2 - \gamma^2\}$. This symmetry has a sign change of the phase for a range of angles around the 45° directions.
[Fig. 2.7 (c)]

$d_{x^2-y^2}$-wave ; $\Delta_{\mathbf{k}} = \Delta_0[\cos k_x - \cos k_y]$. This symmetry has a π-phase shift along orthogonal directions. The magnitude of the gap is strongly anisotropic with nodes along the 45° directions.
[Fig. 2.7 (d)]

d_{xy}-wave ; $\Delta_{\mathbf{k}} = \Delta_0[2\sin k_x \sin k_y]$. This symmetry is similar to the $d_{x^2-y^2}$ case but is rotated by 45°. The gap is strongly anisotropic with nodes along orthogonal direction.
[Fig. 2.7 (e)]

$d_{x^2-y^2}+s$; $\Delta_{\mathbf{k}} = \Delta_0\{(1-\varepsilon)[\cos k_x - \cos k_y] + \varepsilon s\}$. This symmetry is a real admixture of the $d_{x^2-y^2}$-wave and and s-wave symmetry. The s-wave will add to the plus lobes and subtract from the minus lobes of the $d_{x^2-y^2}$-wave. This result in a similar phase-dependence but with asymmetric amplitudes as compared to the $d_{x^2-y^2}$-wave symmetry. In addition, the nodes are shifted from the 45° directions.
[Fig. 2.7 (f)]

$d_{x^2-y^2}+is$; $\Delta_{\mathbf{k}} = \Delta_0\{(1-\varepsilon)[\cos k_x - \cos k_y] + i\varepsilon s\}$. This symmetry is a complex admixture of the $d_{x^2-y^2}$-wave and s-wave symmetry. As a result, the $d_{x^2-y^2}$-wave node disappears and Δ_k becomes fully gapped but anisotropic. The anisotropy is dependent on the fraction of the imaginary admixture. The relative phase becomes a continuous function in k-space with $0 < \Delta\varphi < \pi$. The relative phase between the 90° and 0° direction is less than π, depending on the amount of the imaginary s-admixture.
[Fig. 2.7 (g)]

$d_{x^2-y^2}+id_{xy}$; $\Delta_{\mathbf{k}} = \Delta_0\{(1-\varepsilon)[\cos k_x - \cos k_y] + i\varepsilon[2\sin k_x \sin k_y]\}$. This symmetry is a complex admixture of the $d_{x^2-y^2}$-wave and d_{xy}-wave symmetry. As a result also in this case the $d_{x^2-y^2}$-wave node disappears and Δ_k becomes fully gapped but anisotropic, which is dependent on the fraction of the imaginary component. The relative phase is also a continuous function in k-space, but the relative phase between the 90° and 0° directions is always π.
[Fig. 2.7 (h)]

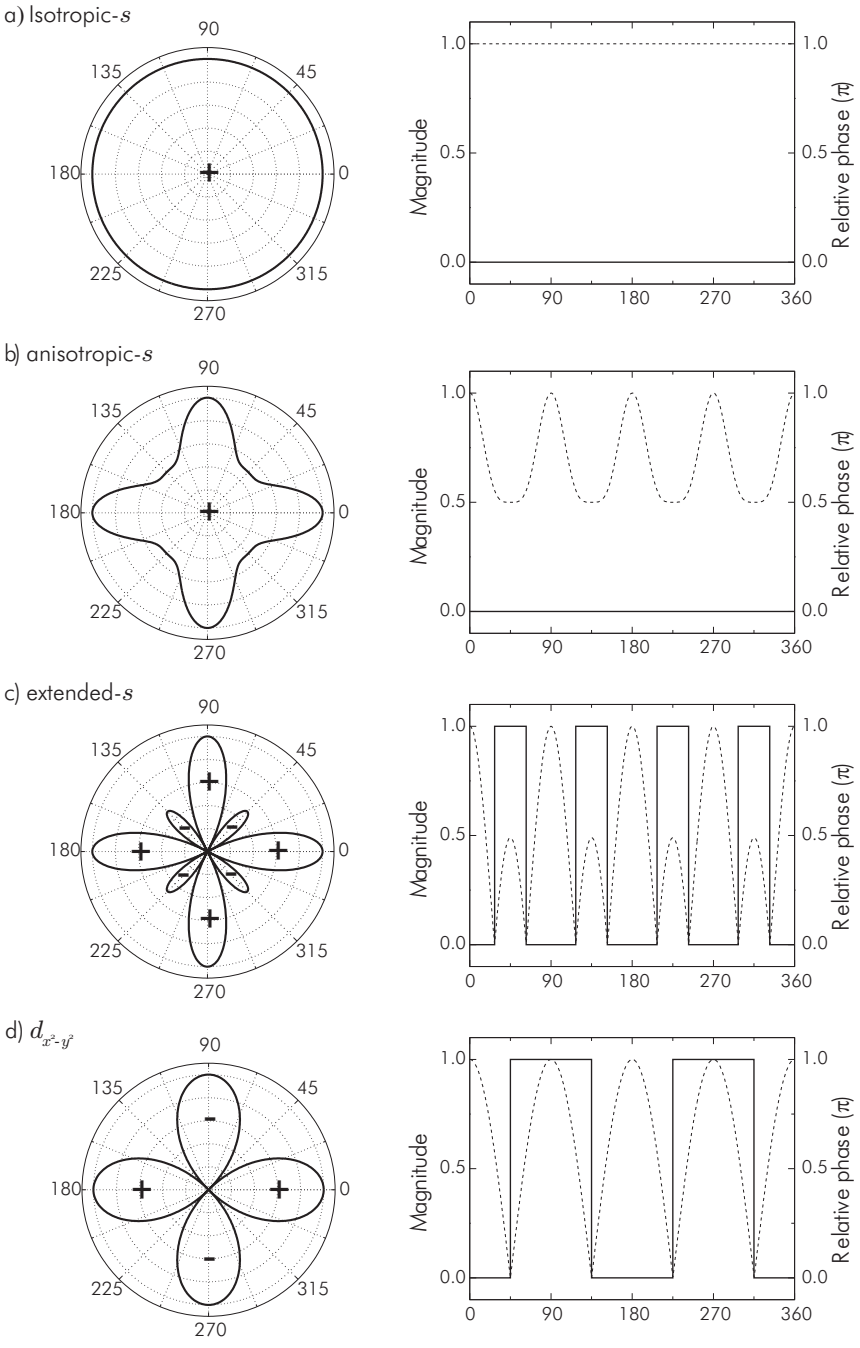
a) Isotropic-s
b) anisotropic-s
c) extended-s
d) $d_{x^2-y^2}$
90
135
45
180
0
225
315
270
+
-
Magnitude
Relative phase (π)
1.0
0.5
0.0
0
90
180
270
360

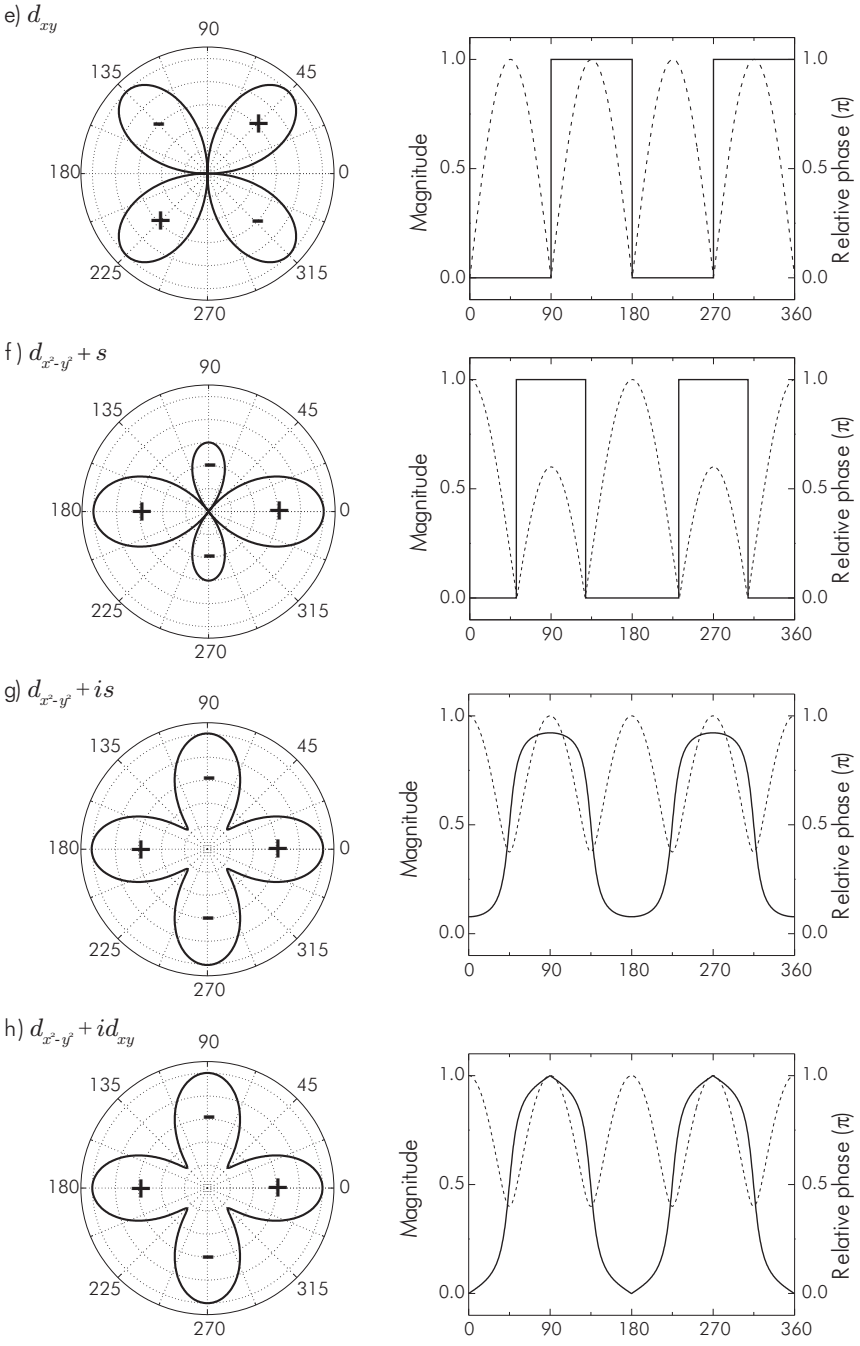

Figure 2.7: Various possible pairing symmetries plotted in k-space; a) isotropic-s, b) anisotropic-s, c) extended-s, d) $d_{x^2-y^2}$, e) d_{xy}, f) $d_{x^2-y^2}+s$, g) $d_{x^2-y^2}+is$, and h) $d_{x^2-y^2}+id_{xy}$. On the right hand side, the magnitude (dashed line) and phase (solid line) are plotted as a function of directions in k-space.

2.4.2 $d_{x^2-y^2}$-wave-induced π-phase-shifts

In Josephson junction arrays involving $d_{x^2-y^2}$-wave superconductors, additional π-phase shifts in the superconducting wave function can be inherently built between the adjacent junctions. This can be realized, *e.g.*, in Josephson junctions between a high-T_c and a low-T_c superconductor.

Combining these two types of superconductors, which have a $d_{x^2-y^2}$-wave and s-wave order parameter symmetry, respectively, gives a freedom to create Josephson structures in which part of the junctions, or even parts within the junctions, are biased with an additional π-phase shift. Figure 2.8 schematically shows Josephson junction structures which are characterized by an additional π-phase difference between the adjacent facets within the junction [Figure 2.8 (a)], and between the two Josephson junctions in the superconducting ring [Figure 2.8 (b)]. The former and latter structures are referred to as a corner (0-π) junction and a dc π-SQUID, respectively. Since the superconducting wave function experiences an additional phase of π when going around a closed contour in those structures, both structures are also called π-rings.

The structures depicted in Fig. 2.8 are combinations of a high-T_c and a low-T_c superconductor. In these structures, both interfaces are aligned along one of the $\langle 100 \rangle$ directions of the high-T_c cuprate. With the high-T_c cuprate being an s-wave superconductor, the structure in Fig. 2.8 (a) presents no significant difference to the case of a straight junction aligned along one of the junction's directions, and the structure in Fig. 2.8 (b) is simply a dc-SQUID described earlier in this chapter. With the high-T_c superconductor having a $d_{x^2-y^2}$-wave symmetry, the facet oriented in one direction experiences an additional π-phase difference compared to that oriented in the other direction. Remark that the negative and positive signs in the figures are used only to describe the π-phase change between the two lobes, and they can be used interchangeably.

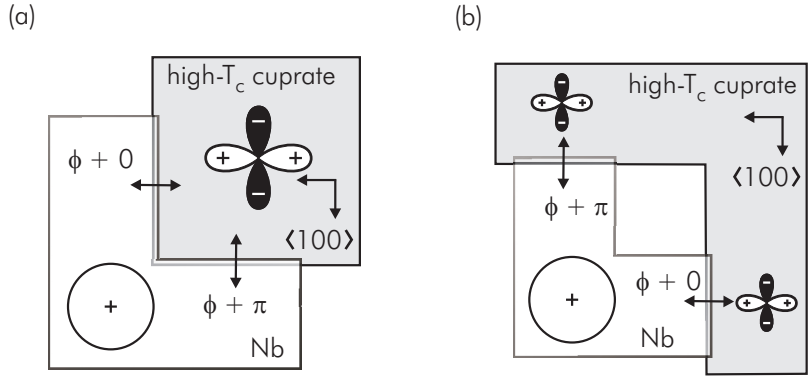

Figure 2.8: Sketch of Josephson junction structures involving superconductors with $d_{x^2-y^2}$-wave and s-wave symmetry, resulting in a relative additional π-phase shift in (a part of) the junction facing the negative lobe of the $d_{x^2-y^2}$-wave symmetry; (a) a corner junction and (b) a π-SQUID.

The gauge-invariant current-phase relation for such 0-π structures can be generally simplified and described as

$$J = \begin{cases} J_c \sin(\phi) & ; \quad \text{without a } \pi\text{-phase shift} \\ J_c \sin(\phi + \pi) & ; \quad \text{with a } \pi\text{-phase shift} \end{cases} \tag{2.38}$$

To simplify the analysis, the π-phase shift may also be treated as a 'negative' critical current density.

The temperature dependence of J_c, calculated from microscopic BCS theory, is given by Ambegaokar and Baratoff [41–43]. When both superconducting electrodes are the same material ($\Delta_1 = \Delta_2$), $J_c(T)$ is given by

$$J_c(T) = \frac{\pi \Delta(T)}{2eR_N} \tanh\left(\frac{\Delta(T)}{2k_B T}\right) \tag{2.39}$$

where R_N is the normal state junction resistance. For a junction with two different electrodes ($\Delta_1 \neq \Delta_2$), J_c at $T = 0$ is given by [43]

$$J_c(0) = \frac{2}{eR_N} \frac{\Delta_1 \Delta_2}{\Delta_1 + \Delta_2} K\left(\frac{|\Delta_1 - \Delta_2|}{\Delta_1 + \Delta_2}\right) \tag{2.40}$$

where K is the complete elliptical integral of the first kind. These expressions are very useful in practice. It allows a ready estimation of the expected maximum supercurrent at $T = 0$.

2.4.3 The magnetic field dependencies of the critical currents

It has been discussed in Section 2.3 that the magnetic field dependence of the critical current $I_c(H_a)$ for a straight junction with a uniform critical current density resembles the Fraunhofer pattern described by Eq. 2.26. In general the $I_c(H_a)$ pattern reaches the highest value of the critical current I_c at zero applied field. The $I_c(H_a)$-dependence becomes somewhat more complicated for $0 - \pi$ junctions. The $I_c(H_a)$-dependence for this case can be obtained using Eq. 2.25 applying the additional phase of π in the critical current distribution as in Eq. 2.38. This leads to

$$I_c(H_a) = \left| \int_{-a}^{0} h J_c(x) e^{i\eta x} + \int_{0}^{a} h J_c(x) e^{i(\eta x + \pi)} \right| \tag{2.41}$$

where a is the facet length, and the linear coordinate x is taken along the facets centered at the corner point. For a uniform critical current density, this results in

$$I_c(H_a) = J_c h \left| \frac{\sin^2\left(\dfrac{\pi\Phi}{\Phi_0}\right)}{\dfrac{\pi\Phi}{2\Phi_0}} \right| \tag{2.42}$$

The critical current as a function of applied flux from Eq. 2.42 is plotted in Fig. 2.9 (a) with a solid line. For comparison, the Fraunhofer diffraction pattern from Eq. 2.26 is plotted with a dashed line in the same figure. The $I_c(H_a)$-dependence for

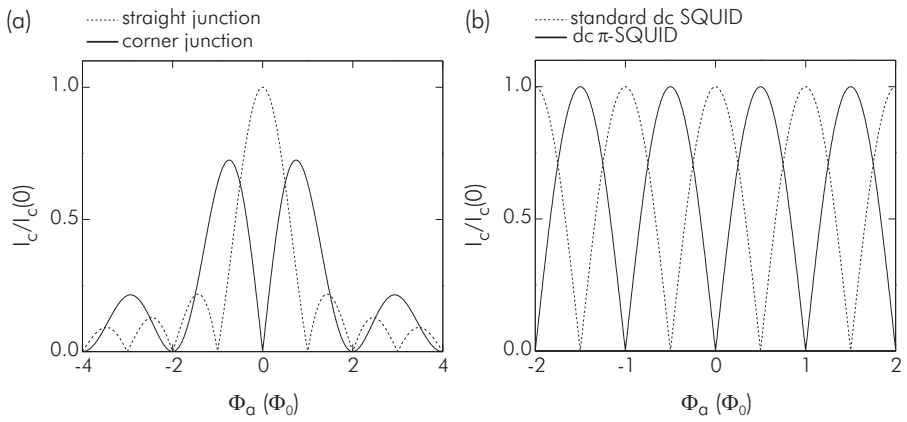

Figure 2.9: (a) The magnetic field dependencies of the critical currents of a corner junction with (solid line) and without (dashed line) a π-phase shift between the two facets, (b) the magnetic field dependence of the critical current pattern for a symmetric π-SQUID (solid line) and a standard dc-SQUID (dashed line), assuming a loop inductance $L = 0$.

$0 - \pi$ junctions has zero critical current at zero applied field, in stark contrast to the Fraunhofer diffraction pattern. The critical current reaches its highest value when the applied magnetic flux per facet approaches $\frac{1}{2}\Phi_0$. In addition, the pattern has a modulation length of $2\Phi_0$.

In equivalence to Eq. 2.30 for the standard dc SQUID, the fluxoid quantization for the dc SQUID with an additional π-phase shift is described by

$$\phi_2 - \phi_1 = 2n\pi - 2\pi\frac{\Phi}{\Phi_0} + \pi \tag{2.43}$$

Using the same method as for the standard dc SQUID, the dependence of the total critical current on the magnetic flux for a symmetric dc π-SQUID neglecting the inductance of the loop is described by

$$I_{c,tot}(\Phi) = 2I_c \left|\cos\left(\frac{\pi\Phi}{\Phi_0} + \frac{\pi}{2}\right)\right| \tag{2.44}$$

This $I_c(H_a)$-dependence is plotted in Fig. 2.9 (b) with a solid line. The pattern is shifted by $\frac{1}{2}\Phi_0$ because of the presence of an additional phase of π in the SQUID loop. While for the standard dc SQUID the critical current has a maximum at zero applied field, for the dc π-SQUID it has a minimum at zero applied field.

2.4.4 State of the art

The $d_{x^2-y^2}$-wave-induced π-phase-shifts in connected Josephson junction arrays have been confirmed in various phase sensitive order parameter symmetry test experiments

on several high-T_c cuprate superconductors as reviewed in [26, 34]. As discussed above, the magnetic field dependencies of the critical currents for such Josephson arrays strongly deviate from the straight Josephson junction. Another intriguing characteristic of Josephson structures with π-phase shifts is that, under certain conditions, they will spontaneously generate fractional magnetic flux quanta of $\frac{1}{2}\Phi_0$, even when no applied fields and currents are present. In chapter 6 and 7, this effect will be discussed in more details. In the following, some experiments in which the π-phase shift has been observed, and thus the $d_{x^2-y^2}$-wave symmetry, will be described.

Corner junction and π-SQUID

Wollman *et al.* [44] performed a phase-sensitive experiment based on a $YBa_2Cu_3O_{7-\delta}$/Au/Pb corner junction schematically shown in Fig. 2.8 (a). The magnetic field dependencies of the critical currents of this junction were observed and compared with a single straight Josephson junction. From their measurement results, it was concluded that the pairing symmetry in $YBa_2Cu_3O_{7-\delta}$ is predominantly $d_{x^2-y^2}$-wave, introducing a π-phase shift in a part of the corner junction which results in a $I_c(H_a)$-dependence deviating from a standard Fraunhofer pattern for a straight Josephson junction. Later independently, Miller *et al.* [45] used frustrated thin-film tricrystal samples to probe the pairing symmetry in $YBa_2Cu_3O_{7-\delta}$ in an experiment analogous to the corner junction. Their results are also consistent with a predominantly $d_{x^2-y^2}$-wave symmetry in the $YBa_2Cu_3O_{7-\delta}$ cuprate.

Experiments using a similar structure as the corner junction, 'the π-SQUID', schematically shown in Fig. 2.8 (b), were performed by Wollman *et al.* [46] utilizing twinned and detwinned $YBa_2Cu_3O_{7-\delta}$/Au/Pb junctions, by Mathai *et al.* [47] utilizing twinned $YBa_2Cu_3O_{7-\delta}$/Ag/Pb junctions, by Brawner and Ott [48] on single crystals of $YBa_2Cu_3O_{7-\delta}$, with two bulk point-contact junctions of Niobium, and by Schulz *et al.* [49, 50] utilizing a low-inductance SQUID design in $YBa_2Cu_3O_{7-\delta}$ thin films epitaxially grown on tetracrystal $SrTiO_3$ substrates. All of the results gave a completely unambiguous evidence for a time-reversal-invariant order parameter with a phase shift of π between the a- and b-axis direction of $YBa_2Cu_3O_{7-\delta}$, and were strongly suggestive of $d_{x^2-y^2}$-wave symmetry pairing in $YBa_2Cu_3O_{7-\delta}$.

However, until recently, more complex geometries have not yet been realized owing to the difficulties faced in preparing controllably high-quality junctions between high-T_c and low-T_c superconductors, and to the geometrical limitations that are set by the use of specially designed tricrystalline or tetracrystalline substrates.

Tricrystal ring

Tsuei *et al.* [5, 26] performed a phase-sensitive test on high-T_c cuprates utilizing grain boundary Josephson junctions in a structure called the tricrystal ring. The tricrystal ring was constructed to have particular orientations of the grain boundaries between adjacent crystals as shown in Fig. 2.10 (a). The orientation of the cuprate thin film grown on the substrate is denoted by the axes and the grid lines. The top left segment has a 30° orientation relative to the lower crystal and 60° to the top right. The grain boundary dividing the top crystals is oriented at an angle of 60° relative to the horizontal grain boundary. The tricrystal ring is located at the tricrystal meeting

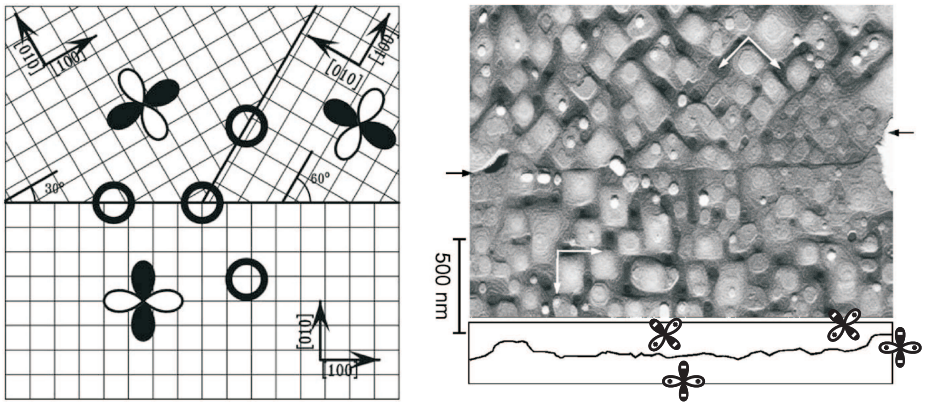

Figure 2.10: (a) Sketch of the tricrystal ring experiment (taken from [51]). (b) Faceting in the high-T_c grain boundary Josephson junction (taken from [16]). The $d_{x^2-y^2}$-wave cloverleafs are added for clarity.

point, and as controls two two-junction rings and one ring with no junctions are either at the bicrystal grain boundaries or not at grain boundary as shown in the Fig. 2.10 (a).

It is clear that for a $d_{x^2-y^2}$-wave order parameter symmetry the wave function in the tricrystal ring experiences a total additional phase of π when circulating around the loop. This introduces a spontaneous magnetization of $\frac{1}{2}\Phi_0$, as was measured by scanning SQUID microscopy. This spontaneous magnetization effect will be discussed in more detail in Chapter 6 and 7. The control rings do not have such additional π-phase shift and exhibit the standard integer flux quantization.

Resulting from the geometrical limitations that are set by the use of specially designed tricrystalline or tetracrystalline substrates, more complex geometries have not been realized yet and only individual half-flux quantum could be studied.

Faceting in the high-T_c grain boundaries junction

High-T_c SQUIDs made from asymmetry 45° [001]-tilt biepitaxial grain boundaries show anomalous dependence of their critical currents on magnetic field [16, 52, 53].

Hilgenkamp *et al.* [54] pointed out that the magnetic field dependencies of the critical currents of grain boundaries strongly dependent on the misorientation angle. For an asymmetric 45° [001]-tilt grain boundary, the patterns are highly deviating from the Fraunhofer-like dependence with maximum peaks at a finite magnetic field [16, 55], similar to the corner junction case. This characteristic behavior is caused by the faceting (grain boundary microstructure) and the $d_{x^2-y^2}$-wave symmetry of the high-T_c cuprates [Fig. 2.10 (b)]. In an asymmetric 45° [001]-tilt grain boundary, the node of the presumed $d_{x^2-y^2}$-wave order parameter symmetry is normal to the average interface on one side of the boundary (see Fig. 2.10) (b). Faceting ro-

tates the normal angle slightly. Because of a random orientation of faceting, each facet experiences either a 0- or π-phase difference depending on its misorientation angle. As a whole, this introduces a random array of junctions with or without additional π-phase shift, producing alternating positive and negative critical currents along the grain boundary. This is equivalent to having a series of π-loops, which spontaneously generate alternating supercurrents, which in turn produce anomalous SQUID interference patterns. This interpretation was supported by scanning SQUID microscope measurements, which imaged the spontaneous magnetization in the grain boundaries [56, 57].

In addition to an anomalous magnetic field dependence of the critical current and the spontaneous generation of un-quantized magnetic flux, the unusual electronic properties of the grain boundary junctions include also anomalous dependencies between the critical current and the gauge-invariant phase difference over the junctions [58–60]. As this faceting is uncontrollable, such grain boundary junctions provide only limited possibilities for more detailed and systematic studies, *e.g.*, on the effects of spatial correlations in the sign changes of the critical current densities on the electronic properties of the Josephson contacts [55]. To model the faceting in grain boundary junctions in a controllable manner, a structure called the zigzag Josephson junction, discussed later in Chapter 4 and schematically shown in Fig. 4.1, can be realized by combining superconductors with $d_{x^2-y^2}$-wave and s-wave symmetry.

2.4.5 Terminology: 0- and π-facets

It has been discussed that a π-phase shift can be realized within a junction due to the $d_{x^2-y^2}$-wave pairing symmetry in high-T_c cuprate superconductors. Furthermore, it has been suggested and shown in several experiments that a π-phase shift can also be realized within a junction by mechanisms unrelated to the pairing symmetry, such as spin-flip scattering by magnetic impurities [61], indirect electron tunneling [62], junctions with ferromagnetic barrier [63, 64], non-equilibrium quasiparticle population [65–67], or conventional junctions with a pair of tiny injectors [68].

Because the term π-junction is reserved for junctions that experience a π-phase drop across the junction, such as those with ferromagnetic barrier, in this thesis the 0- and π-junction terms are avoided when it concerns order parameter induced phase-shifts. Instead the terms of π- and 0-facet will be used to describe junctions with and without π-phase shift, respectively, in multiple connected arrays. However, a superconducting ring with an odd number of π-phase shifts, independent of whether the π-phase shifts results from symmetry or tunneling mechanism effects, will be referred to as π-rings, and a ring with an even number of π-phase shifts as 0-rings.

Chapter 3

Fabrication aspects and measurement techniques

To exploit the $d_{x^2-y^2}$-wave pairing symmetry in the high-T_c cuprate superconductors, all Josephson junction arrays described in this thesis were fabricated based on thin-film ramp-type Josephson contacts between the high-T_c cuprate and a low-T_c superconductor. In most cases, the high-T_c cuprate $YBa_2Cu_3O_{7-\delta}$ was employed as the base electrode. For studies on the order parameter symmetry in the electron-doped compound $Nd_{2-x}Ce_xCuO_{4-y}$ described in Chapter 5, the $YBa_2Cu_3O_{7-\delta}$ base electrode is replaced by $Nd_{2-x}Ce_xCuO_{4-y}$ with various Ce-doping levels. The keystone to obtain a sufficient transparency in ramp-type Josephson junctions is the interlayer concept. With this, a thin interlayer is incorporated to restore the surface damaged by ion milling. A further advantage is that it allows an all *in situ* barrier deposition between the two superconductors, leading to clean and well-defined interfaces.

In this chapter, the preparation of thin-film ramp-type Josephson contacts between the high-T_c cuprate and the low-T_c Niobium superconductor will be discussed. This includes thin-film deposition processes, structuring of the arrays, and improved ramp-type concepts. Later on in this chapter, measurement techniques used for characterizing the samples will be introduced, including transport measurements, low temperature scanning electron microscopy, and scanning SQUID microscopy.

3.1 Fabrication aspects

In the high-T_c cuprate superconductors, it is known that the coherence length is longer and the charge density of states is larger in the planar $a-b$ directions of the cuprate layers. For these reasons, the ramp-type [9, 15, 69] interface configuration (Fig. 3.1) is frequently used for Josephson contacts involving thin-film high-T_c superconductors. Relating to the high-T_c superconductors, a further advantage of using the ramp-type configuration is that one has a freedom to choose any junction orientations, or even simultaneously fabricate a large number of junctions at variable directions in the $a-b$ plane of the cuprates on a single chip. The use of the ramp-type geometry also allows

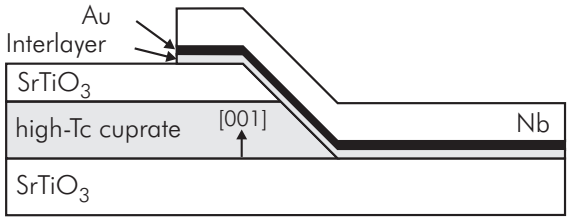

Figure 3.1: Thin-film ramp-type Josephson junction between the high-T_c cuprate and the low-T_c Niobium superconductor.

one to tailor junction properties by varying the barrier material and its thickness.

A crucial step in the preparation of ramp-type interfaces is the structuring of the beveled edge in the superconducting base electrode. This step unfortunately can severely degrade the quality of the base electrode near the interface. To address this problem, a thin interlayer is introduced [10] on top of the ion-beam structured high-T_c base electrode. This leads to a much cleaner interface. Figure 3.1 schematically shows the final layout of the ramp-type Josephson junctions between the high-T_c cuprate and the low-T_c Nb superconductor that are used for the experiments described in this thesis. The complete fabrication steps for fabricating thin-film ramp-type Josephson contacts between the high-T_c cuprate and the low-T_c Nb superconductor are schematically depicted in Fig. 3.2. In the following, the fabrication procedures to realize this ramp-type Josephson junction will be discussed step by step.

Substrate preparations

For the development of a reliable deposition technology for high-quality high-T_c superconductor thin films, the choice of the substrate material is of primary importance. The basic requirements are a crystallographic lattice match between the high-T_c cuprate and the substrate, and similar thermal expansivity of the high-T_c films and substrate. Furthermore, substrates should be suitably polished, stable, and reasonably robust.

Depending on the application of the films, specific requirements are imposed on the substrate. For experiments described in this thesis, the edge-alignment of the substrate crystal axes is specifically required in order to facilitate a good alignment of the junction interfaces with respect to the high-T_c crystal axes. Therefore, all the samples were fabricated on the edge-aligned $SrTiO_3$ [001]-oriented single crystal substrates, with an alignment accuracy was better than 1°.

The $SrTiO_3$ substrate termination determines the growth and material properties of the $YBa_2Cu_3O_{7-\delta}$ thin films on the (sub)unit cell scale. To ensure a reproducibility of the thin film growth, a single terminated surface is a prerequisite. For this, the substrates are etched using a buffered HF solution and subsequently annealed in flowing oxygen for 1.5 hour at 950 °C, resulting in the substrates with a single TiO_2 terminated surface [70].

The twin behavior of $YBa_2Cu_3O_{7-\delta}$ thin films grown by pulsed-laser deposition

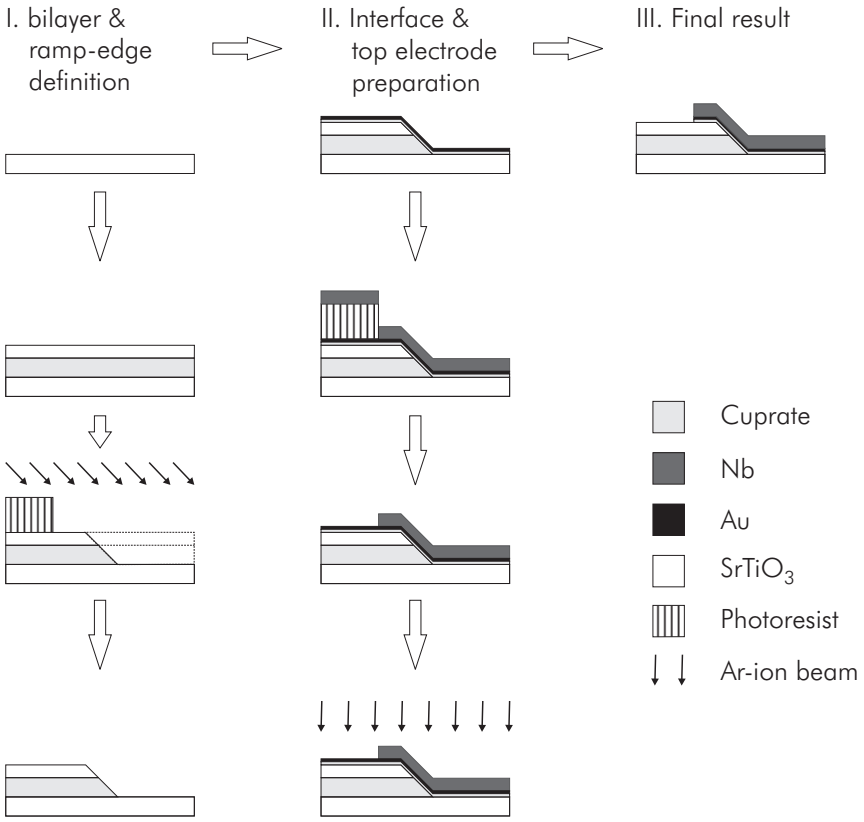

Figure 3.2: The complete fabrication steps for realizing thin-film ramp-type Josephson contacts between the high-T_c cuprate and low-T_c Nb superconductors.

is strongly affected by the vicinal properties, *i.e.*, angle and in-plane orientation, of $SrTiO_3$ [001] substrates [71]. The vicinal angle α is defined between the optical and the crystallographic substrate surface, and its in-plane orientation β with respect to the $SrTiO_3$ $\langle 100 \rangle$ crystal axis (see Fig. 3.3). On substrates having an $\langle 110 \rangle$ in-plane orientation of the step edges, a completely preferred twin pair can be obtained if α is increased to 0.6°. On the other hand, on substrates having an $\langle 100 \rangle$ in-plane orientation of the step edges, the degree of twinning can be controlled from the presence of four *ab*-orientations to single-domain [001] $YBa_2Cu_3O_{7-\delta}$ by varying the vicinal angle from a low angle $\alpha \sim 0.1°$ to $\alpha = 1.10°$. Around $\alpha = 1.10°$, the diffusion length of $YBa_2Cu_3O_{7-\delta}$ during the growth is expected to match the terrace length of $SrTiO_3$, resulting in almost completely detwinned $YBa_2Cu_3O_{7-\delta}$ films.

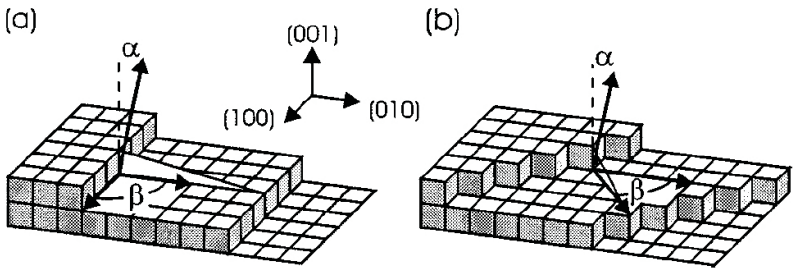

Figure 3.3: Schematic representation of the vicinal substrate surface. The step edges are oriented along (a) the ⟨100⟩, and (b) the ⟨110⟩ crystallographic axis (taken from [71]).

3.1.1 The high-T_c cuprate thin-films

After substrate preparation, the first step in the sample fabrication processes is the growth of a bilayer of the $YBa_2Cu_3O_{7-\delta}$ or $Nd_{2-x}Ce_xCuO_{4-y}$ cuprate base electrode and the $SrTiO_3$ insulation layer. The growth of the bilayer was performed in a home-built vacuum chamber with a load-lock system. Additionally, this vacuum system is also equipped with an inline chamber for an *in situ* etching process. A background pressure of 1×10^{-7} mbar can be generally achieved in this system. A deposition in two types of gas environments, Oxygen (O_2) or Argon (Ar), is possible in this vacuum chamber.

The bilayer-deposition is accomplished using pulsed-laser deposition, utilizing a pulsed Lambda Physik XrF excimer laser with 248 nm wave length. In general, the pulsed laser deposition technique allows an accurate control of the film stoichiometry. The [001]-oriented $SrTiO_3$ single crystal substrates are mounted with silver paint onto a heater. A plume of the vaporized target material is created by focusing the laser beam at the target via a lens with a focal length of $f \approx 45$ cm, and is directed at the substrate, whose temperature and position can be controlled. Prior to the deposition, the target is always cleaned by ablating some material from the target surface while keeping the trajectory of the plume to the target closed. This preablation step is performed with a 10 Hz laser pulse for 2 minutes. To achieve a homogeneous energy distribution over the laser spot at the target, the laser beam is passed through a mask with a window area of 98 mm^2. The mask is positioned between the laser source and focusing lens. The pressure during deposition can be controlled ranging from 1×10^{-4} to 5×10^2 mbar using a variable valve and mass flow controllers. The process parameters, such as deposition pressure and temperature, are determined by the type of the material being grown.

$YBa_2Cu_3O_{7-\delta}$-film growth procedures

The $SrTiO_3$ substrate is mounted on the heater using silver paint, and subsequently heated up for outgassing before being loaded into the load-lock chamber and transferred to the deposition chamber. The background pressure is maintained at about

4×10^{-7} mbar at 200 °C substrate temperature, prior to heating up the substrate slowly to the deposition temperature T_{dep} of 780 °C. The heating up of the substrate is performed at this background pressure of up to 600 °. To *in situ* anneal and clean the substrate, 0.25 mbar O_2 gas is introduced when the temperature reaches 600 °.

The deposition of the $YBa_2Cu_3O_{7-\delta}$ film is performed in an O_2 environment at a deposition pressure P_{dep} of 0.25 mbar using a $YBa_2Cu_3O_7$ target. The spot size of the laser beam at the target is 5.7 mm^2 with an energy density E_s of 1.2 J/cm^2. This gives a deposition rate v_{dep} of 1.00 Å/pulse for the $YBa_2Cu_3O_{7-\delta}$ film. Films with a typical thickness of 150 nm or 300 nm are prepared with a 4 Hz laser pulse. During the ablation, the substrate is scanned relative to the plume to ensure a uniform film over the entire substrate. Subsequently, the $SrTiO_3$ insulation layer is deposited at 740 °C in 0.10 mbar O_2. The parameters for the $SrTiO_3$ deposition are listed in Table 3.1. After depositing the $SrTiO_3$ insulation layer, the annealing process is performed in two steps at 600 °C for 15 minutes and at 450 °C for 30 minutes in an O_2 environment, by venting the system. Finally the sample is slowly cooled down to room temperature and taken out from the chamber. The complete annealing procedure for the $YBa_2Cu_3O_{7-\delta}$ films is given in the left panel of Fig. 3.4. This procedure yields a typical critical temperature T_c of 89 K for the $YBa_2Cu_3O_{7-\delta}$ films.

$Nd_{2-x}Ce_xCuO_4$-film growth procedures

The procedures for the $Nd_{2-x}Ce_xCuO_{4-y}$ depositions are similar to the $YBa_2Cu_3O_{7-\delta}$ films, but they differ strongly in the deposition temperatures and annealing procedures. For the optimally doped films, a $Nd_{1.85}Ce_{0.15}CuO_4$ target, and for the overdoped cases a $Nd_{1.835}Ce_{0.165}CuO_4$ target is used. The $Nd_{2-x}Ce_xCuO_{4-y}$-film depositions are performed at 820 °C in 0.25 mbar O_2. The spot size of the laser beam at the target is also 5.7 mm^2 and the energy density $E_s = 2.5$ J/cm^2. This gives a deposition rate v_{dep} of 0.83 Å/pulse. Films with a typical thickness of 150 nm or 300 nm are prepared with a 4 Hz laser pulse. Sub-

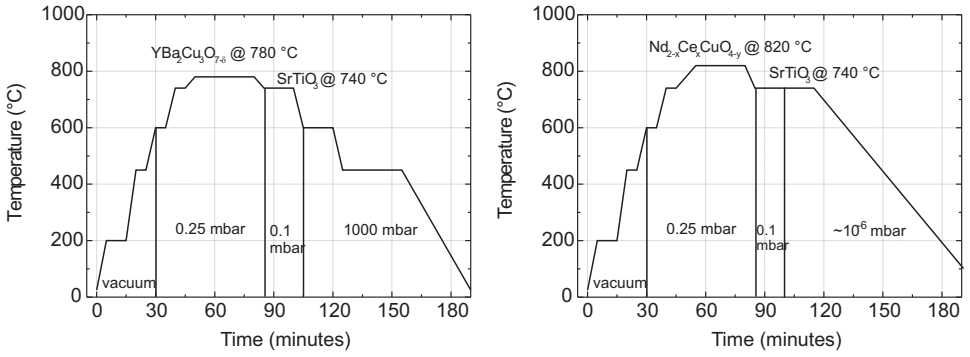

Figure 3.4: Annealing procedures for the (left) $YBa_2Cu_3O_{7-\delta}$ and (right) $Nd_{2-x}Ce_xCuO_{4-y}$ thin-film depositions.

Material	T_{dep} (°C)	P_{dep} (mbar)	E_{spot} (J/cm^2)	A_{spot} mm^2	v_{dep} (Å/pulse)
$YBa_2Cu_3O_{7-\delta}$	780	0.25 O_2	1.2	5.7	1.00
$Nd_{2-x}Ce_xCuO_{4-y}$	820	0.25 O_2	1.2	5.7	0.83
$SrTiO_3$	740	0.10 O_2	1.2	5.7	0.64
Au	100	0.22 Ar	4.0	3.5	0.20

Table 3.1: Parameters used for thin film depositions using pulsed laser ablation.

sequently, the $SrTiO_3$ insulation layer is deposited at 740 °C in 0.10 mbar O_2 in a similar way to the bilayer $YBa_2Cu_3O_{7-\delta}$-$SrTiO_3$ case. After depositing the insulation layer, the deposition chamber is evacuated to about 1×10^{-6} mbar and the sample is kept at 740 °C for 10–15 minutes, before it is slowly cooled down to room temperature under vacuum conditions. The complete annealing procedure for the $Nd_{2-x}Ce_xCuO_{4-y}$ films is given in the right panel of Fig. 3.4. For the optimally doped $Nd_{1.85}Ce_{0.15}CuO_4$ films, this procedure yields a typical critical temperature T_c of 20 K, the overdoped $Nd_{1.835}Ce_{0.165}CuO_4$ films have T_c's of 13 K. The T_c's for $Nd_{1.85}Ce_{0.15}CuO_4$ and $Nd_{1.835}Ce_{0.165}CuO_4$ are optimized with respect to the oxygen content in the films.

3.1.2 Interfacing the high-T_c and the low-T_c superconductors

After the preparation of the cuprate bottom electrode and the insulating layer, the definition of the bottom electrode and the preparation of the ramp are performed. These are done by applying a photoresist mask and subsequently removing the uncovered parts by Argon-ion milling.

Photolithography

First a positive photoresist-stencil of Shipley 1813 is dropped uniformly all over the sample, which is placed on a spinner. The sample is directly spun at 4000 or 5000 rotations per minute for 30 sec to uniformly spread and harden the photoresist, and it is subsequently baked at 100 °C for 10 min. Generally, the photoresist at the edges of the sample will be thicker than that in the middle due to the spinning. The resist is therefore exposed to UV-light with an energy density of 10 mW/cm^2 for 45 sec, through a square positive mask which is designed only to remove the photoresist at

the edges of the sample. This is done in order to allow a better contact between the mask and the sample during the sample-layout transferring, giving a more highly precise pattern than the one without this step. The photoresist is developed in a water-diluted 5%-NaOH developer (5 water : 1 developer) for 25 sec, and followed by two immersions in demiwater for 15 and 20 sec, respectively. Then the designed sample-layout is transferred by exposing the sample to UV light for $6 - 12$ sec, and subsequently developed in a similar way as the edge-part removal process.

Argon-ion milling

The removal of uncovered film material is simultaneously performed with the ramp interface preparation, using accelerated Argon ions (Argon-ion milling). The process is accomplished in a vacuum system with a background pressure of 4×10^{-6} mbar.

The milling process is performed at a beam voltage of 500 V and a beam current of 100 mA in 5×10^{-3} mbar. The ramps are etched under an angle of $\beta = 45°$ between the incoming Ar-ions and the sample surface, while rotating the sample at 18 rotations per beam-pulse. The rotation of the sample during the milling yields an identical ramp interface for all directions. To protect the sample from heating up due to the ion bombardment, the Ar-ion beam is pulsed with 8 sec in on-mode and 12 sec in off- mode. This results in an etching rate of 6.25 nm/pulse for $YBa_2Cu_3O_{7-\delta}$, 3.60 nm/pulse for $Nd_{2-x}Ce_xCuO_{4-y}$, and 4.20 nm/pulse for $SrTiO_3$. Finally the photoresist residue is removed by using acetone and ethanol.

The effective ramp angle α for a stationary sample during etching is roughly estimated by [10, 72]

$$\alpha = \arctan\left(\frac{1}{1+x}\tan\beta\right) \tag{3.1}$$

where x is the ratio of the etching rate of the photoresist over the etching rate of the thin film. Taking $x = 2$ for $YBa_2Cu_3O_{7-\delta}$ [10] and $x = 1$ for $Nd_{2-x}Ce_xCuO_4$ yield $\alpha = 18°$ and $26°$, respectively. The difference of α relative to β can be understood from the etching process shown schematically in Fig. 3.5. As the photoresist retracts

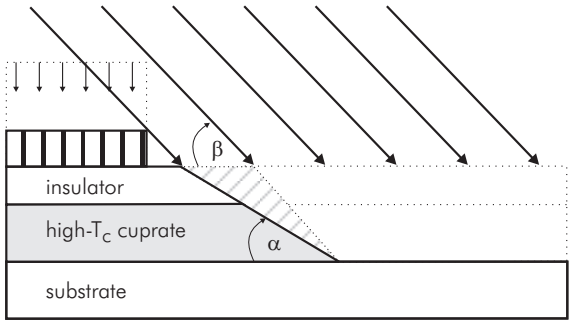

Figure 3.5: Argon ion-milling process for structure definition and ramp-edge preparation. β is the angle of incidence of the ion beam and α is the angle of the ramp-edge.

because its thickness is decreased during milling, a portion of the thin film represented by the shaded region will be gradually removed (see Fig. 3.5), leading to a smaller ramp-angle α than the angle of incidence of the ion beam β.

Interlayer and the Au barrier

The ramp interface is one of the most important ingredients in order to have a reliable Josephson contact. The milling process of the ramp however introduces a damaged region close to the ramp surface [10, 11]. Eventhough a special care is taken to obtain clean interfaces and the samples are annealed prior to the Au barrier deposition, critical current densities have never exceeded 1 A/cm^2 at 4.2 K, with normal resistance (R_nA) values of the order of 10^{-4} Ωcm^2 [11]. This poor interface transparency is attributed to the fact that just an annealing procedure will not recover the correct stoichiometry at the ramp-edge surface. To overcome this problem, two steps are introduced prior to the deposition of the Au barrier layer. Those are the soft-etch cleaning by ion-milling and the deposition of the interlayer.

After the removal of the photoresist in the previous step, the sample is surface-cleaned by Ar-ion milling in an inline etching chamber separated to the deposition chamber by a controllable valve, to allow an *in situ* interlayer and barrier layer deposition. The milling is performed in two steps; first, with a beam voltage of 500 V and a beam current of 10 mA for 4 pulses (hard-etch), and second, with a beam voltage of 50 V and a beam current of 5 mA for 10 pulses (soft-etch). Subsequently, the sample is transferred *in situ* − without breaking the vacuum − into the deposition chamber. Then, a very thin layer of the same material as the base electrode is grown in a similar

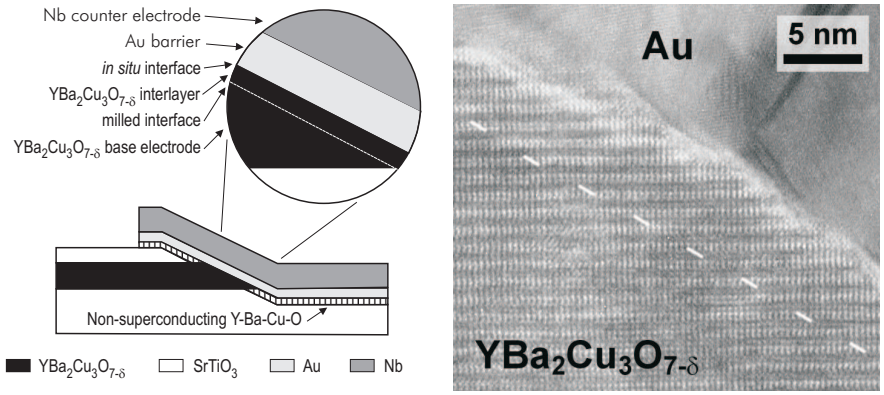

Figure 3.6: Bright-field transmission electron microscopy image of the $YBa_2Cu_3O_{7-\delta}$/Au interface at the ramp-edge area, including an $YBa_2Cu_3O_{7-\delta}$ interlayer of 6 nm. Crystalline $YBa_2Cu_3O_{7-\delta}$ material is observed up to the Au interface, while no clear interface (dashed line) is observed between the base electrode and the interlayer (taken from [11]).

way to the cuprate base electrode. In the case of $YBa_2Cu_3O_{7-\delta}$, this interlayer is 7 nm and for $Nd_{2-x}Ce_xCuO_{4-y}$ it is 12 nm. These were found to be the optimized values with respect to the obtained critical current density of the respective samples. This interlayer is expected to stabilize the off-stoichiometric etched surface of the base electrode and enables *in situ* formation of the interfaces between the electrodes and barrier, leading to a much cleaner interface. Figure 3.6 shows a transmission electron microscopy image of the $YBa_2Cu_3O_{7-\delta}$/Au interface at the ramp-edge area, including an $YBa_2Cu_3O_{7-\delta}$ interlayer of 6 nm. Crystalline $YBa_2Cu_3O_{7-\delta}$ material is observed up to the Au interface, while no clear interface (dashed line) is observed between the base electrode and the interlayer [11].

The Au barrier is grown directly *in situ* after interlayer deposition. The deposition is performed by pulsed laser deposition at a substrate temperature of ~ 100 °C in 0.22 mbar Ar environment. The choice of Ar instead of O_2 results in a smoother surface and has a wetting effect on the cuprates during the Au deposition, thus decreases the density of pinholes especially in the case of a very thin Au barrier layer [10]. Furthermore, the deposition pressure has been optimized in order to decrease the effect of high-energy particles in the plasma that are ablated from the Au target at the cuprate layer [10]. A common deposition problem of metals is the occurrence of droplets on the surface. Using the above mentioned parameters, a low density of droplets was observed with practically no significant effect on the experiments.

3.1.3 The Niobium thin-films

The definition of the Nb top electrode is performed *ex situ* by first applying photoresist prior to the Nb deposition. Niobium is deposited in a sputter system with a background pressure of 1×10^{-7} mbar. An *in situ* cleaning process of the Au surface is introduced before the Nb deposition. This is done by rf sputter removal of < 1 nm Au, with an rf power of 50 W resulting in a voltage bias V_{bias} of 310 V. Subsequently, a Nb film with a typical thickness of 160 nm is deposited by a standard dc sputtering with a dc voltage and power of 365 V and 250 W, respectively, in a deposition pressure of 7.3×10^{-3} mbar of Argon gas. Using these deposition parameters, a robust deposition rate of 80 nm/min is obtained.

As a final step, after lifting-off the unnecessary Nb part and removing the photoresist by using acetone and ethanol, the redundant, uncovered Au and interlayer underneath are removed by ion milling for a few pulses.

3.2 Measurement techniques

In this section, three different measurement techniques used for the experiments on the arrays are described. Transport measurements including $(I-V)$-characterizations and $I_c(H_a)$-dependencies were performed at the Universiteit Twente. Low temperature scanning electron microscopy experiments were executed at the Physikalisches Institut, Universität Tübingen by Prof. D. Kölle and co-workers. The magnetic imaging of the spontaneously-generated magnetic flux expected to thread through the Josephson junction arrays was performed at the IBM T.J. Watson Research Center by Dr. John Kirtley.

3.2.1 Transport measurements

The current-voltage characteristics and the magnetic field dependencies of the critical currents were measured in a helium cryostat at 4.2 K. The measured sample was attached to PC-board using Ge-varnish and the superconducting leads were connected to the electrical contacts on a PC-board by Al wire-bonds. The $I_c(H_a)$-dependence was measured by applying a magnetic field perpendicular to the sample surface. A Nb shield and RLC filters were used to reduce external noise. With this, a typical dc background magnetic field of ~ 0.2 μT was observed.

The measurements of the $I_c(H_a)$-dependencies are performed using a feedback loop. The voltage over the sample is measured and coupled back to the current source, keeping the voltage $V_c \leqslant 5$ μV at a constant value. In case of hysteresis in the current-voltage curve, this leads to an oscillating behavior of the current between the critical current I_c and the return current I_r. The black areas in the $I_c(H_a)$-graphs indicate this hysteresis. The $I_c(H_a)$-dependencies are obtained by scanning just in one direction with the field (*e.g.* from negative to positive H_a), reversing the bias current and scanning the field in the opposite direction (from positive to negative H_a). Depending on the resolution and the applied magnetic-field range, the scanning process will be completed approximately in $1/4 - 2$ hours. The scan direction does not influence the obtained dependence. No averaging was applied, nor scanning many times. The magnetic field dependencies are very reproducible down to the smallest features, so that averaging would not change the patterns significantly.

3.2.2 Low temperature scanning electron microscopy

Low temperature scanning electron microscopy experiments were executed by the group of Prof. D. Kölle at the Physikalisches Institut, Universität Tübingen. All measurements were performed in a liquid helium (LHe) cryostage of a Scanning Electron Microscope (SEM), as described in detail in [73, 74]. In short, the cryostage consists of a small LHe tank placed inside the SEM and has a connection to a LHe reservoir. The sample was mounted on top of a cold finger while its surface was scanned by the electron beam. The back of the sample is mounted in good thermal contact with a thermal reservoir. The LHe tank is surrounded by μ-metal shields to provide a low-noise environment.

Figure 3.7 schematically shows the electrical network outside the SEM setup for the LTSEM imaging experiment on $YBa_2Cu_3O_{7-\delta}$/Nb ramp-type zigzag junctions. The network consists of a current source with two outputs for the current bias and for the field coil. Since the voltage differences caused by the electron beam are in the order of $10 - 100$ nV, the voltage outputs of the sample are 1000-fold amplified. The electron beam perturbation is periodically modulated resulting in a periodically modulated response signal, which is detected phase sensitively by a lock-in amplifier. A two dimensional voltage $\delta V(x, y)$ image of the sample is obtained by scanning the sample and measuring the electron beam induced change of the sample voltage simultaneously.

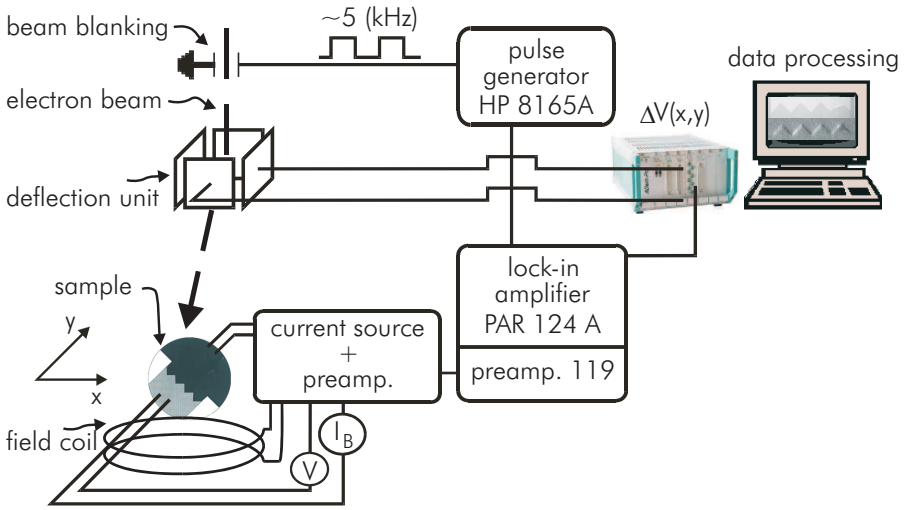

Figure 3.7: The setup for Low Temperature Scanning Electron Microscopy (LTSEM) imaging experiments.

3.2.3 Scanning SQUID microscopy

The scanning SQUID microscope is an extremely sensitive instrument for imaging local magnetic fields. To measure the magnetic fields, it employs a SQUID, the most sensitive magnetic field sensing element known. This very high sensitivity is the inherent advantage of the scanning SQUID microscopy compared to many other techniques for imaging magnetic fields at surfaces [75–78]. In addition, it gives an easily calibrated absolute value for the local magnetic fields.

Basically a SQUID microscope scans a sample with a scan area of a few hundred microns on a side to image the sample magnetic fields. To obtain optimal resolution, the SQUID pickup loop has to be very small, well shielded, and positioned as close as possible to the sample surface. The obtainable spatial resolution of a scanning SQUID microscope depends among other factors on the effective SQUID area. An effective area of only a few μm^2 is desirable as it allows a spatial resolution of a few μm. In principle, a SQUID with nanobridges as weak links provides very small junction areas of below 0.1 μm^2 [79]. But some problems still have to be solved before this structure can be realized in the scanning SQUID microscope. Nevertheless, there are many possible applications for the scanning SQUID microscope which do not require sub-micron spatial resolution [76].

The magnetic imaging of spontaneously generated magnetic flux expected to thread through the Josephson junction arrays discussed in this thesis was performed at the IBM T.J. Watson Research Center by Dr. John Kirtley. A high-resolution scanning SQUID microscope as described in detail in [75, 76] was employed. In short, the scanning SQUID microscope employed has pickup loops integrated into the SQUID

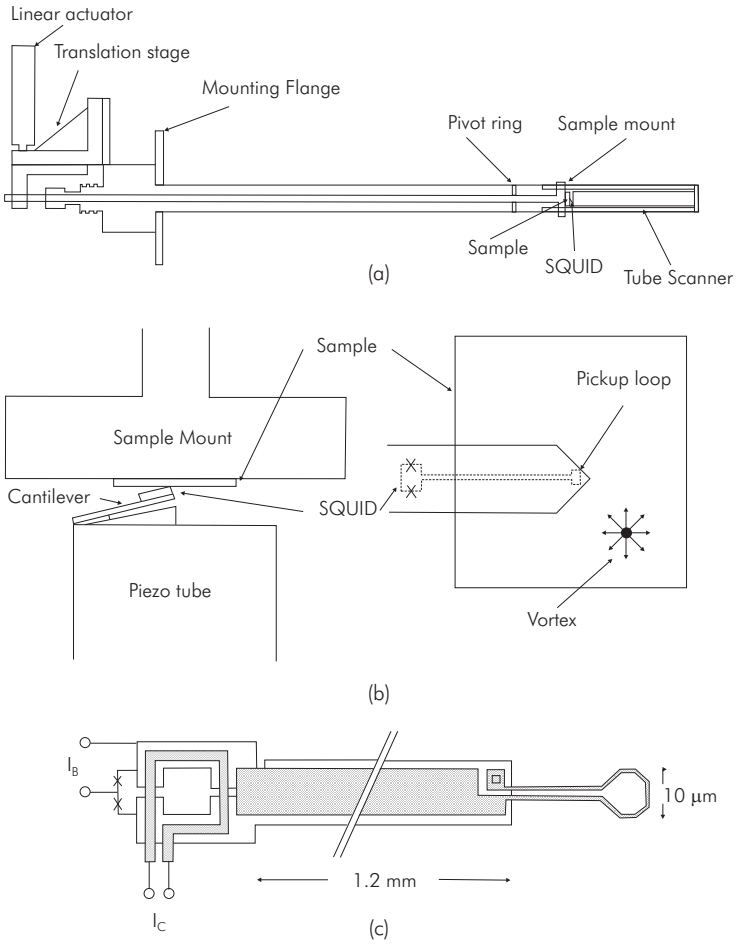

Figure 3.8: (a) Schematic diagram of the IBM scanning SQUID microscope. (b) Expanded views of the sample area. (c) Schematic layout of the integrated magnetometer (taken from [75]).

sensor itself. It is immersed in liquid helium in a μ-metal-shielded dewar which is suspended from the ceiling of a screened room with elastic cords. A sketch of the scanning SQUID microscope is shown in Fig. 3.8 (a). The sample is mounted at the end of a long, thin-walled stainless tube. The longitudinal and transverse position of the translation stage can be adjusted with a differential micrometer and scanned with dc motors, respectively.

Figure 3.8 (b) shows an expanded view of the microscope at the sample area. For scanning a mechanical lever is used. The SQUID sensor is mounted on a cantilever, and is run in direct contact with the sample. This mechanical scanning mechanism has

the advantages of having relatively large scan area with good linearity and repeatability, and retaining a good sensitivity and spatial resolution. The spacing between pickup loop and the sample was optimized with respect to the spatial resolution and sensitivity. The scanning SQUID microscope has a well shielded pickup loop integrated into the design of low-T_c dc SQUIDs, with the pickup loop diameter of 10 μm or 4 μm. The sketch of the pickup loop is shown in Fig. 3.8 (c). This design provides a relatively small coupling between the SQUID and the system to be measured, good shielding of the parts of the SQUID away from the pickup loop, and a good spatial resolution. The noise of the SQUIDs used is typically $< 2 \times 10^{-6}$ $\Phi_0/\mathrm{Hz}^{1/2}$, corresponding to a field noise at the pickup loop of $\sim 4 \times 10^{-11}$ $\mathrm{T}/\mathrm{Hz}^{1/2}$.

Chapter 4

Arrays of $YBa_2Cu_3O_{7-\delta}$/Nb Josephson junctions in a zigzag configuration

In this chapter, the realization and characterization of one-dimensional zigzag-shaped $YBa_2Cu_3O_{7-\delta}$/Au/Nb Josephson junctions are described. Measurements and analyses on the magnetic field dependencies of the critical currents of these junctions are presented. The results show convincingly that the order parameter symmetry in the $YBa_2Cu_3O_{7-\delta}$ is predominantly $d_{x^2-y^2}$-wave, and simultaneously that the magnetic field dependencies of the critical currents of zigzag junctions resemble, in their basic features, the ones observed for asymmetric 45° grain boundary junctions. Furthermore, using low temperature scanning electron microscopy, the Josephson current counterflow in these junctions can be directly observed. All zigzag junctions described in this chapter are considered to be in the small facet limit, *i.e.*, the width of the junction facets is considerably smaller than the Josephson penetration depth ($a \ll \lambda_J$). In Chapter 6, the opposite case in which $a \gg \lambda_J$ will be discussed.

4.1 Introduction

Controllable Josephson junctions comprising the high-T_c cuprate superconductor enable detailed and systematic studies on the order parameter symmetry in this class of materials and its effects on Josephson devices. In order to realize designed complex geometries incorporating the high-T_c cuprate superconductors, sufficient flexibility and control are required in the positioning of the junctions. A suitable way to achieve this is, in an all-thin-film process, using ramp-type junctions as described in Chapter 3.

Based on various studies, there is now a substantial experimental evidence that the order parameter symmetry in the hole-doped high-T_c cuprate superconductors, such as $YBa_2Cu_3O_{7-\delta}$, is predominantly $d_{x^2-y^2}$-wave [5, 26, 34, 44]. In Chapter 2, it has been discussed that with this symmetry the superconducting wave function exhibits a π-phase difference for orthogonal direction in k-space, and that a possibility

arises to configure multiply connected Josephson junctions with a built-in π-phase difference. Examples of Josephson junction arrays with an additional phase of π have also been shown in Chapter 2. Those structures are mostly formed by connections between high-T_c and low-T_c superconductors, or by using grain boundary configurations prepared by employing specially designed tricrystalline or tetracrystalline substrates. Resulting from the geometrical limitations of such special substrates, more complex geometries have not been realized yet in the form of grain boundary Josephson junctions. On the other hand, the difficulties to fabricate high-quality Josephson contacts between high-T_c and low-T_c superconductors have until recently limited the studies on this hybrid Josephson junction. A method to overcome this problem has been established [10, 11, 80, 81], as described in Chapter 3. This opens a possibility to controllably create Josephson contacts along specified directions of the high-T_c cuprates, or even to combine a large number of Josephson contacts with a complex structure on a single chip. The first structure that has been studied is the zigzag Josephson junction [17].

4.2 $YBa_2Cu_3O_{7-\delta}$/Au/Nb zigzag junctions

The zigzag Josephson junction has been briefly introduced in Chapter 2. In general, the zigzag Josephson junction is an array of Josephson contacts in a zigzag geometry as shown in Fig. 4.1. In this configuration, all the Josephson contacts are aligned along a $\langle 100 \rangle$ direction of the high-T_c cuprate. Analogous to grain boundary junctions, the individual contacts in the zigzag junctions are referred to as facets. The facets oriented

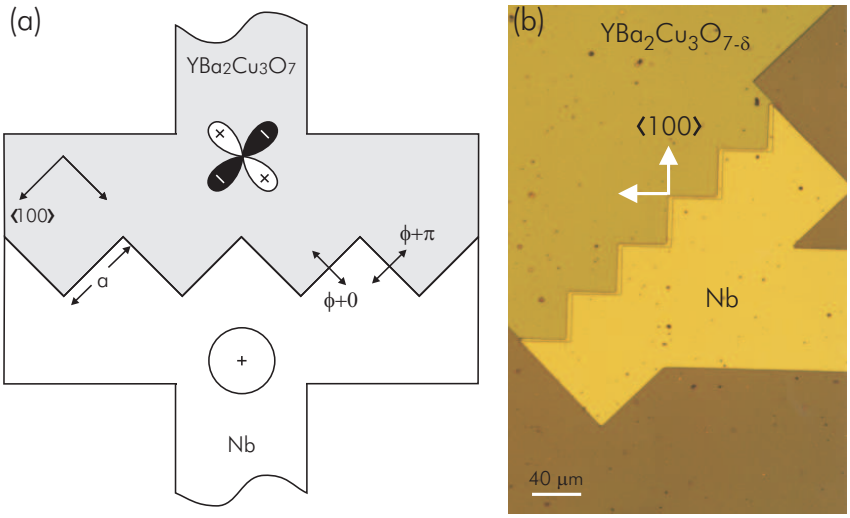

Figure 4.1: (a) Sketch of a zigzag junction. (b) An optical image of a zigzag junction between $YBa_2Cu_3O_{7-\delta}$ and Nb with 40 μm facet-width. The facets are oriented along the $\langle 100 \rangle$ directions of the $YBa_2Cu_3O_{7-\delta}$.

along one direction are expected to experience an additional π-phase difference relative to those oriented in the other direction due to the predominant $d_{x^2-y^2}$-wave order parameter symmetry of the high-T_c cuprate. Basically, in a zigzag Josephson junction, multiple 0- and π-facets are placed controllably at alternating position.

In the zigzag structure, all the facets are aligned along either $\langle 100 \rangle$ directions of the $YBa_2Cu_3O_{7-\delta}$, and are designed to have identical (absolute) values of the critical current densities J_c. In order to create identical circumstances for all facets in the zigzag structure, the samples were ion milled under an angle with the substrate plane, with the in-plane velocity components of the incident Ar ions oriented along the $YBa_2Cu_3O_{7-\delta}$ $\langle 110 \rangle$-direction. Alternatively, the samples can be ion milled under an angle of 45° with respect to the substrate plane and rotated during the ramp definition.

Figure 4.1 (b) presents an optical image of a zigzag structure with 10 facets of 10 μm width. On the same chip, there are in total 4 zigzag junction with 80, 40, 10, and 8 facets of 5, 5, 40, and 25 μm width, respectively. In addition there are two pairs of straight junctions facing the $YBa_2Cu_3O_{7-\delta}$ $\langle 100 \rangle$ direction with 5 and 50 μm width. Each pair has junctions facing either $\langle 100 \rangle$ direction. Since the a- or b-direction of the $YBa_2Cu_3O_{7-\delta}$ crystal axes is not fixed along a certain direction in the sample due to the possibility of twinning, the $\langle 100 \rangle$ symbol is used to describe that it can be the a- or b-axis of the $YBa_2Cu_3O_{7-\delta}$ film.

For the specific sample in Fig. 4.1 (b), the thickness of the bilayer $YBa_2Cu_3O_{7-\delta}$ and $SrTiO_3$ are 150 nm and 100 nm, respectively, and the thickness of the Nb top electrode is 140 nm. The ramp interface is prepared with 6 nm $YBa_2Cu_3O_{7-\delta}$ and a 14 nm Au-barrier layer. Measurements on this sample will be presented later on in this chapter.

4.3 Magnetic field dependence of the critical current

4.3.1 Introduction

In Chapter 2, the magnetic field dependence of the critical current $I_c(H_a)$ for a straight junction and for a single 0-π junction with a uniform critical current density has been discussed. It resembles the Fraunhofer pattern, which reaches the highest value of the critical current I_c at zero applied field. On the other hand the $I_c(H_a)$-dependence for a single $0-\pi$-junction has zero critical current at zero applied field, in stark contrast to the Fraunhofer diffraction pattern. The critical current reaches its highest value when the applied magnetic flux per facet approaches $\frac{1}{2}\Phi_0$.

The $I_c(H_a)$-dependence becomes somewhat more complicated for a zigzag array of $0-\pi$-junctions. However, for a uniform critical current density, the $I_c(H_a)$-dependence for zigzag junctions with an arbitrary number of facets can be comprehended in a relatively simple theoretically model. In this case, an additional phase of π is added to the current-phase relation for every facet facing one direction, and no additional phase for facets facing the other direction (see Fig. 4.1, the '+' and '-' symbols in the pairing symmetry functions are added for clarity). Then the zigzag junction can be

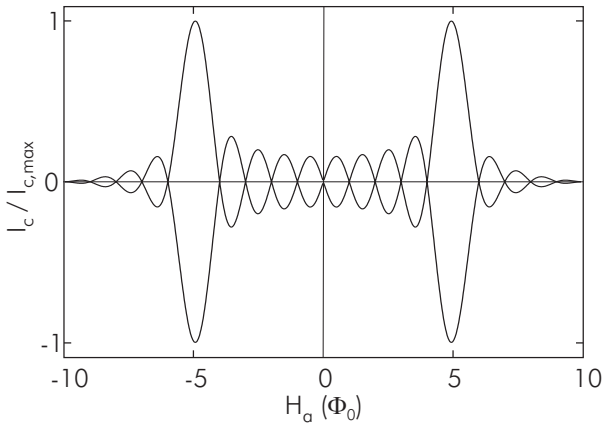

Figure 4.2: The calculation result for the magnetic field dependence of the critical currents of a zigzag junction with 10 facets, assuming a constant (absolute) value of the local critical current density along the junction.

considered as a one dimensional series of independent facets with a critical current density for facet j described by

$$J_j = J_c \sin(\phi + n_j \pi) \tag{4.1}$$

where $j = 1, 2, ..., N$ with N is the number of facets, and $n_j = \frac{(-1)^j+1}{2}$ takes a value of either 0 or 1, representing alternating facets with or without additional π-phase shifts. The critical current is then the amplitude of the current density integration for all facets, as described by equation 2.25. This gives

$$I_c(H) = \left| \sum_{j=1}^{N} \int_{(j-1)a}^{ja} J_c(x) h e^{i(\phi x + n_j \pi)} dx \right| \tag{4.2}$$

where a is the facet length. Assuming a constant local critical current density, integration and straight forward algebra yields

$$\begin{aligned} I_c = & \frac{J_c h a}{k} \left\{ \left(\sum_{j=1}^{N} [(1 - \cos k) \sin(n_j \pi + jk) + \sin k \cos(n_j \pi - jk)] \right)^2 \right. \\ & \left. + \left(\sum_{j=1}^{N} [(1 - \cos k) \cos(n_j \pi - jk) - \sin k \sin(n_j \pi + jk)] \right)^2 \right\}^{1/2} \end{aligned} \tag{4.3}$$

where $k = 2\pi\Phi/\Phi_0 N$, and Φ is the applied flux.

Figure 4.2 shows the $I_c(H_a)$-dependence of a zigzag junction with 10 facets calculated from Eq. 4.3, assuming a constant (absolute) value of the local critical current densities along the junction. Characteristic features of the $I_c(H_a)$ patterns for the zigzag arrays are the occurrence of sharp maxima in I_c for an applied magnetic flux $\Phi_{max} = N\Phi_0/2$, and the vanishing I_c at $\Phi = 0$ for an even number of facets. Further, the number of minima in I_c in the flux range $-\Phi_{max} < \Phi < \Phi_{max}$ is predicted to equal $N-1$. It is noted here that in this analysis possible self-generated magnetic flux is not taken into account, which becomes important if the facet length is significant in comparison with the local Josephson penetration depth [19, 57, 82, 83].

4.3.2 Measurement results

The critical current has been measured as a function of applied magnetic field for various zigzag junctions. Each sample contains several straight junctions as references. In all cases, the magnetic field H_a was applied along the [001]-direction of the $YBa_2Cu_3O_{7-\delta}$ unit cell. Critical currents were measured with a voltage bias below 5 μV. Variations of the bias voltage in this range did not affect the basic features in the $I_c(H_a)$ characteristics.

Figure 4.3 (a) shows a typical current-voltage $I(V)$-characteristic and $I_c(H_a)$-dependence of a single $YBa_2Cu_3O_{7-\delta}$/Au/Nb Josephson junction oriented along the $YBa_2Cu_3O_{7-\delta}$ $\langle 100 \rangle$ axes. The $I(V)$-characteristic is hysteretic (which is indicated in the $I_c(H_a)$-dependence with the black area), with a maximal value of the critical current of $I_c \approx 6.0$ μA, corresponding with $J_c = 80$ A/cm^2, taking as the junction area the product of the $YBa_2Cu_3O_{7-\delta}$ layer thickness (150 nm) and the junction width (50 μm). From this, the Josephson penetration depth λ_J for these junctions is estimated to be approximately 36 μm. The Josephson penetration depth is calculated using Eq. 2.27, where the effective magnetic thickness t was calculated using the $YBa_2Cu_3O_{7-\delta}$ and Nb London penetration depth presented in Table 2.2 and corrected using Eq. 2.22. The critical current decreases when increasing the applied magnetic flux. Further increasing the applied flux, the critical current modulates and decreases further. The $I_c(H_a)$-dependence resembles the Fraunhofer-like pattern described by Eq. 2.26, with a large maximum in the critical current at zero applied magnetic field.

Figure 4.3 (b) displays the $I_c(H_a)$-dependence for an array of 8 facets of each 25 μm width, placed in the zigzag geometry of Fig. 4.1. Clearly the maxima in the critical current are now observed at a non-zero applied magnetic field, $H_a = 1.1$ μT. At this field-value I_c equals 50 μA. In Fig. 4.3 (c) the $I_c(H_a)$-dependence is shown for an array of 10 alternating 0- and π-facets of 40 μm width. Here the maximal $I_c = 48$ μA is obtained at $H_a = 0.46$ μT. Finally, in Fig. 4.3 (d) the $I_c(H_a)$-dependence is shown for an array of 80 facets of 5 μm width. This very complex array even shows highly symmetric patterns with maxima occurring at non-zero applied magnetic field, namely $I_c = 41$ μA at $H_a = 5.1$ μT. The ratios between the I_c-values at zero magnetic field and the maximal critical currents are 17%, 6% and 27% for the arrays shown in Fig. 4.3 (b)−(d), respectively.

The magnetic field dependencies of the critical currents for the arrays obviously display the characteristic features indicated by Fig. 4.2, namely the absence of a global maximum at zero magnetic field and the sharp increases in the critical current at a

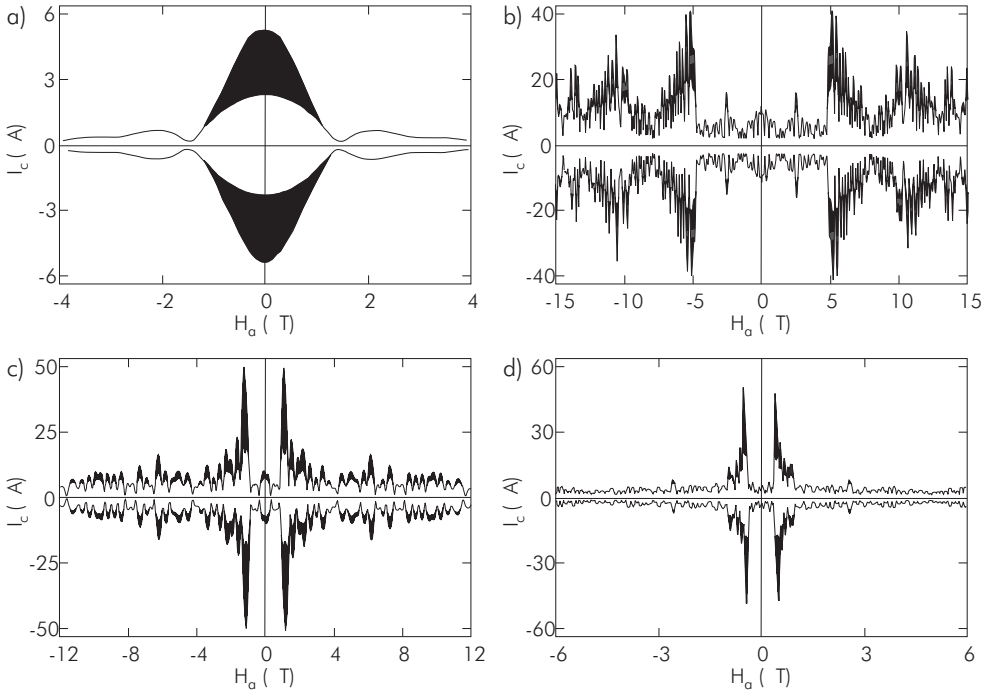

Figure 4.3: Magnetic field dependencies of the critical currents for (a) a 50 μm straight junction, and zigzag arrays of (b) 80 facets of 5 μm width, (c) 8 facets of 25 μm width, and (d) 10 facets of 40 μm width.

given applied magnetic field. This behavior can only be explained by the arrays being comprised of facets alternatingly biased with or without an additional π-phase change. As all facets are aligned along the $\langle 100 \rangle$ axes of the $YBa_2Cu_3O_{7-\delta}$ and were prepared in an identical way, intrinsic processes at the interfaces cannot be the cause of these π-phase shifts and the results thus provide compelling evidence for a predominant $d_{x^2-y^2}$-wave symmetry of the order parameter in the $YBa_2Cu_3O_{7-\delta}$. It is noted that the characteristics of the arrays resemble, in their basic features, the ones observed for asymmetric 45° [001]-tilt grain boundary junctions [16, 53]. This strongly supports the hypothesis that the anomalous characteristics of these grain boundary junctions are due to the occurrence of regions with additional π-phase shifts along the interface.

With the employed ramp-type junction configuration, in which the ramp has a slope of 20° with respect to the substrate plan, the interface normal-vector to the barrier has a large component in the $YBa_2Cu_3O_{7-\delta}$ c-axis direction. From this, a significant c-axis component to the critical current of the array could in principle be expected. If this contribution were to arise from an imaginary s-wave symmetry-component of the order parameter in the c-axis direction, then its sign would not be expected to change for the orthogonal adjacent facets. Therefore it would contribute to the supercurrent that is observed at zero magnetic field. As $I_c(H_a = 0)$ is found

to be very small for all arrays, such an s-wave c-axis contribution is considered to be small, if not negligible. The $YBa_2Cu_3O_{7-\delta}$ films are twinned on a considerably smaller length scale than the facets. If a c-axis component to the supercurrent would change its sign over a twin boundary, *e.g.* in a real s-wave admixture, its contribution to the supercurrent at zero magnetic field is expected to be averaged out. This scenario is consistent with the data presented.

Admixture of complex order parameters

Order parameter symmetry tests thus far have shown that in $YBa_2Cu_3O_{7-\delta}$ it is predominantly $d_{x^2-y^2}$-wave [26], but none has unambiguously ruled out (complex) order parameter admixtures. Because of the orthorhombicity of $YBa_2Cu_3O_{7-\delta}$, subdominant order parameter components may be expected to arise, such as real admixture $d_{x^2-y^2}+s$ and imaginary admixture $d_{x^2-y^2}+is$. Various experiments to study such possible admixtures often rely on tunneling along the $\langle 110\rangle$ direction of the $YBa_2Cu_3O_{7-\delta}$, which is the nodal direction of the $d_{x^2-y^2}$-wave symmetry component [84, 85]. In such a configuration, it is difficult to distinguish whether possible subdominant components are intrinsic to the superconductivity in the $YBa_2Cu_3O_{7-\delta}$, or whether they are induced only locally by the particularities connected with the $\langle 110\rangle$ interfaces, *e.g.*, the presence of Andreev bound states [84, 85]. Therefore, order parameter symmetry test experiments that avoid such $\langle 110\rangle$ surfaces, as is the case for the zigzag arrays, are of particular interest.

In chapter 2, some possible admixture pairing symmetries are shown and plotted in momentum space, such as $d_{x^2-y^2}+is$ and $d_{x^2-y^2}+id_{xy}$. In the case of $d_{x^2-y^2}+is$, the relative phase difference for orthogonal directions in k-space is $0 < \phi < \pi$, and is dependent on the strength of the complex s-wave admixture. For a gap function of the form $\Delta_{\mathbf{k}} = (1-\varepsilon)\Delta_d + i\varepsilon\Delta_s$, where Δ_d and Δ_s represent the $d_{x^2-y^2}$-wave and s-wave order parameter, respectively, and ε is the fraction of the s component, the phase difference γ along orthogonal directions can be generalized as

$$\gamma = \pi - 2\arctan\left|\frac{\varepsilon}{1-\varepsilon}\right| \tag{4.4}$$

The phase shift γ reduces to $\gamma = \pi$ for pure $d_{x^2-y^2}$-wave symmetry ($\varepsilon = 0$), and to $\gamma = 0$ for pure s-wave symmetry ($\varepsilon = 1$). The supercurrent density in zigzag junctions for each facet can the be described as

$$J_j = J_c \sin(\phi + n_j\gamma), \tag{4.5}$$

Using a similar method to Eq. 4.3 leads to

$$\begin{aligned} I_c = \frac{J_c h a}{k}\Bigg\{ &\left(\sum_{j=1}^{N}\left[(1-\cos k)\sin(n_j\gamma + jk) + \sin k\cos(n_j\gamma - jk)\right]\right)^2 \\ &+ \left(\sum_{j=1}^{N}\left[(1-\cos k)\cos(n_j\gamma - jk) - \sin k\sin(n_j\gamma + jk)\right]\right)^2\Bigg\}^{1/2} \end{aligned} \tag{4.6}$$

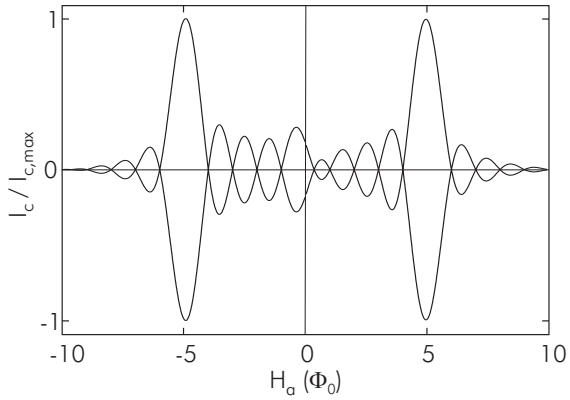

Figure 4.4: The magnetic field dependence of the critical currents of a zigzag junction with 10 facets and 10% of imaginary s-wave admixture.

Figure 4.2 shows the $I_c(H_a)$-dependence of a zigzag junction with 10 facets calculated from Eq. 4.6, assuming an admixture of 10% imaginary s-wave admixture to the $d_{x^2-y^2}$-wave symmetry. If the order parameter were to comprise an imaginary s-wave admixture, the $I_c(H_a)$ dependencies for the arrays would be expected to display distinct asymmetries, especially for low fields. From the high degree of symmetry of the measured characteristics, it can be concluded that there is only a small, if any, imaginary s-wave contribution. It is noted here that due to the twinning in the films, no conclusions can be drawn about possible real s-wave admixtures. Furthermore, the presented configuration is insensitive to possible admixture of subdominant d_{xy} components, as all facets face a nodal direction of this symmetry component.

Flux focusing effects

For the two arrays with the smaller amount of facets, the number of minima before reaching the global maxima in critical currents corresponds exactly with the theoretical predictions following from Eq. 4.3, namely 4 for the array with 8 facets of 25 μm width and 5 for the array with 10 facets of 40 μm width. For the array with 80 facets of 5 μm width, the number of minima is somewhat smaller, namely 21 instead of the expected 40. This difference can be attributed to the influences of flux focusing, creating a non-homogeneous flux coupling to the junction, as described for line-shaped junctions *e.g.* in [86, 87]. Because of the flux focusing, the local flux density in the center of the array is expected to be larger than at the edges, the effects of which become increasingly noticeable for an increasing amount of facets in the arrays. Figure 4.5 shows the $I_c(H_a)$-dependence that was calculated for an array of 80 facets, in the small limit, assuming the flux profile as indicated in the inset. By these simulations it was found that the number of minima is reduced due to the flux focusing. A striking feature following the simulations, which is also seen in the experiments, is that although there is a sharp enhancement in the critical current when reaching the

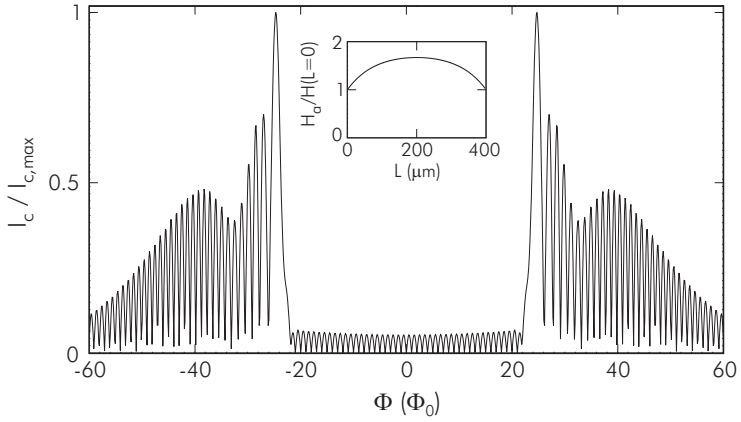

Figure 4.5: The magnetic field dependence of the critical currents for an 80 facets junction under influence of flux focusing with a field distribution as in the inset.

major peak, due to the flux focusing, a more shallow decrease in I_c for larger applied magnetic fields occurs. This does not follow from Fig. 4.2, in which flux focusing was not considered.

4.4 Imaging of the local currents by LTSEM

4.4.1 Introduction

Low temperature scanning electron microscopy (LTSEM) represents a highly promising method for investigating physical phenomena in superconducting thin films and Josephson tunnel junctions [74, 88, 89]. This technique allows one to image the critical current density distribution with a spatial resolution of about 1 μm. It is based on the scanning of a focused electron beam over the surface samples, while simultaneously modifications of the critical currents are recorded. The effect of the electron can be considered as a local heating resulting in an increase of the sample temperature at the beam position. During the scanning process the sample is current biased at a value $I_b \gtrsim I_c$ and the electron beam induced change $\delta V(x, y)$ of the sample voltage is recorded as a function of the beam coordinates.

4.4.2 Measurement results

The measurements were performed on the same zigzag sample described in Section 4.3.2, when the sample was already about two years of age. The main attention was to the zigzag junction with 8 facets of 25 μm width each. Before LTSEM imaging experiments were performed, the sample was electrically characterized in a Helium-

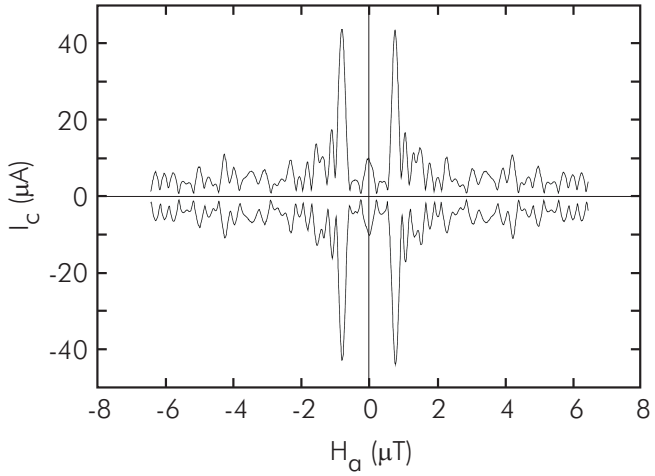

Figure 4.6: The magnetic field dependence of the critical currents of a zigzag sample with 8 facets of 25 μm width, measured prior to the LTSEM experiments.

bath cryostat to address the question of whether the sample degraded in time and of whether the same electrical characteristics as those obtained at the Universiteit Twente could be reproduced. Figure 4.6 shows the $I_c(H_a)$-dependence of the above mentioned junction at 4.2 K from the measurement performed at the Universität Tübingen. The pattern is similar to the one obtained from the previous measurement as in Fig. 4.3 (c). All small features in Fig. 4.3 (c) appear also in Fig. 4.6, with a maximum critical current of about 45 μA. From this, it can be concluded that there is no significant degradation in the sample.

Prior to the LTSEM imaging experiments, the $I_c(H_a)$ characterization was redone in the LTSEM. This was essential to identify appropriate points in the $I_c(H_a)$-pattern, and to see the influence of the environment in LTSEM on the $I_c(H_a)$ pattern. Figure 4.7 (a) shows the $I_c(H_a)$-dependence of the same junction mentioned above. In this figure, the results of measurements in LTSEM setup is presented by the square dots, and is compared to the $I_c(H_a)$ pattern obtained from the measurement in the liquid Helium cryostat presented by the solid line. The critical currents were measured with a 6 μV voltage criterion. It is clear that the critical currents of the measurements in LTSEM setup are reduced significantly compared to the measurements in the liquid Helium cryostat. The maximum critical current of ~ 15 μA in the LTSEM falls to about 33% of its maximum value obtained from measurements in liquid helium cryostat. This difference was due to a higher minimum-achievable temperature of about 6.2 K in LTSEM, and to a noisier environment in the LTSEM than in the liquid helium cryostat. Despite this difference, identical basic features are still present in the LTSEM result.

Figure 4.7 (b) and (c) show typical LTSEM voltage images of the 25 μm facet junction recorded at $T = 6.2$ K. The images were obtained by scanning the current

biased junction and recording the electron beam induced change of the junction voltage as a function of beam position. For optimal results, the images were taken using a beam voltage of $V_{\mathrm{beam}} = 10$ kV and beam current of $I_{\mathrm{beam}} = 50$ pA. The scanning direction was perpendicular to a line connecting two next-nearest neighboring corners. The junction was biased with a control current just above the critical current. The white and black signals in the LTSEM images correspond to positive and negative voltage changes, respectively.

Each micrograph in Fig. 4.7 corresponds to an applied field in the $I_c(H_a)$ pattern depicted. In Fig. 4.7 (b), an external applied magnetic field of $H_a = -0.88$ μT was applied during the recording of the image, corresponding to the maximum critical current in $I_c(H_a)$-pattern. The LTSEM voltage image at zero applied field was pre-

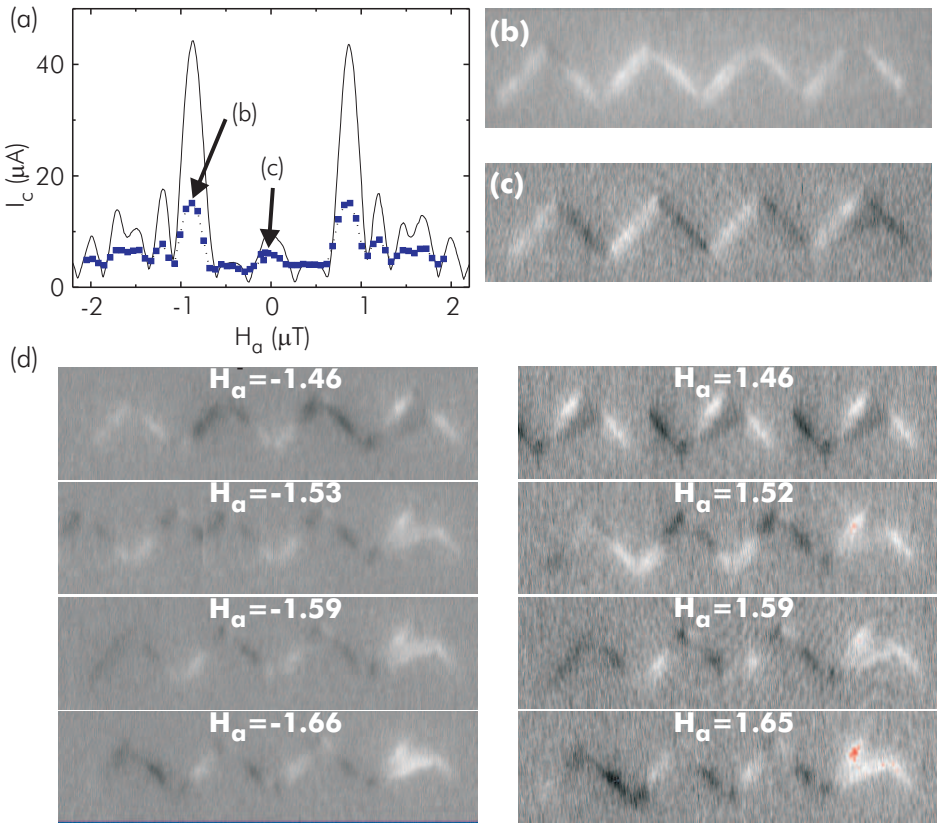

Figure 4.7: (a) The magnetic field dependencies of the critical currents measured in a liquid helium cryostat (solid line) and in the LTSEM setup (square dots). The LTSEM images for (b) an applied field corresponding to the maximum I_c in the $I_c(H_a)$ pattern, and for (c) zero applied field. (d) The LTSEM images for both polarities of applied magnetic fields.

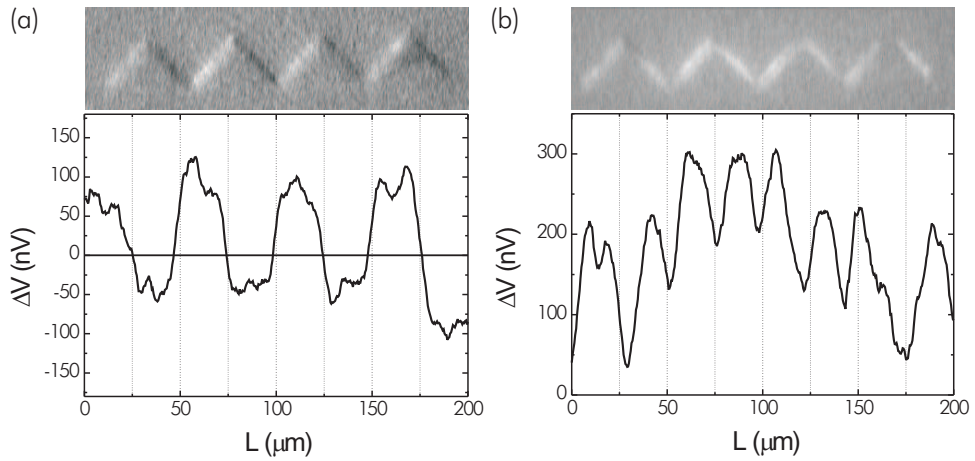

Figure 4.8: The voltage signals from the LTSEM measurements (a) for zero applied field, and (b) for an applied field corresponding to the maximum I_c in the $I_c(H_a)$-pattern.

sented in Fig. 4.7 (c). In this image the white and black signals alternatingly appear on the facets from left to right. This situation is as theoretically expected because at zero applied field the phase difference of the facets in the zigzag junctions is biased alternatingly by an additional phase different of 0 and π, due to the $d_{x^2-y^2}$ order parameter symmetry in high-T_c cuprates. The situation is totally different for images taken at an applied field corresponding to the maximum peak of the critical current in the $I_c(H_a)$-dependence. In this case the LTSEM micrograph shows a single white signal for all the facets in the junction. The images look qualitatively quite similar when the polarity of the magnetic field is changed, as shown in Fig. 4.7 (d). In this case the sensitivity is different by a factor of 2.5 between the measurements in the negative and positive applied magnetic fields. Changing the polarity of the bias current, however, reverses the polarity of the signals as expected.

In general, a beam-induced change in the phase difference function cannot always be ignored and can have a significant effect on the measured quantity δV, as pointed out by Chang and coworkers [90, 91]. However for the case of small limit junctions and for a small applied perturbation, this change in the phase difference can be neglected [92, 93]. Figure 4.8 (a) and (b) show the voltage signals for zero applied field and for an applied field corresponding to the maximum I_c in the $I_c(H_a)$-pattern, respectively. Above these voltage signals, the corresponding voltage images are depicted. The voltage signals are plotted for a single line along the facet of the junction. Since the measured zigzag junction is in the small facet limit, the measured voltage signal is about proportional to the local current density. That is, the voltage image shows the spatial distribution of the field-modulated critical current density along the facet in the zigzag junction. This measurement is the first direct observation of the Josephson current counterflow in a Josephson junction with built-in π-phase shifts.

4.5 Concluding remarks

The realization and characteristics of zigzag-shaped $YBa_2Cu_3O_{7-\delta}$/Au/Nb junctions are described. This demonstrates that high-quality thin-film ramp-type Josephson junctions between the high and low temperature superconductors can be realized. Even complex combinations of such structures can be fabricated on a single chip in a controllable way.

The $I_c(H_a)$ dependencies of the zigzag-shaped $YBa_2Cu_3O_{7-\delta}$/Au/Nb junctions resemble, in their basic features, the ones observed for asymmetric 45° [001]-tilt grain boundary junctions. The results provide evidence for a Josephson current counterflow, in agreement with a π-phase shift between the two adjacent facets in the zigzag junctions. This simultaneously provides evidence for a predominant $d_{x^2-y^2}$-wave order parameter symmetry in the $YBa_2Cu_3O_{7-\delta}$. The highly symmetric $I_c(H_a)$ characteristics indicate that a possible subdominant imaginary s-wave admixture to the $d_{x^2-y^2}$-wave order parameter symmetry, if any, is below 1%. Furthermore, the Josephson current counter flow in zigzag junctions has been directly observed by using the low temperature scanning electron microscopy. This provides a direct proof of the sign change in phase of the order parameter in $YBa_2Cu_3O_{7-\delta}$.

On the contrary to the grain boundary junction, zigzag Josephson junctions between $d_{x^2-y^2}$-wave and s-wave superconductors demonstrate the feasibility to realize complex thin-film Josephson structures consisting of a multitude of π-loops. Besides, such structures also provide a means to identify the pairing symmetry of the still controversial high-T_c cuprates and to derive an upper bound for a possible admixture of subdominant symmetry components to the order parameter symmetry of the cuprates. Furthermore, it also enables one to realize theoretically proposed elements for superconducting (quantum) electronics [6–8, 23]. The latter has been demonstrated for example as described in [21, 23].

Chapter 5

Pairing symmetry tests on $Nd_{2-x}Ce_xCuO_{4-y}$ utilizing zigzag junctions

The thin-film ramp-type Josephson junction between a high-T_c cuprate and a low-T_c s-wave superconductor in a zigzag configuration has been demonstrated as an excellent instrument for testing the order-parameter symmetry in the high-T_c cuprate $YBa_2Cu_3O_{7-\delta}$. In this chapter, phase-sensitive order parameter symmetry test experiments are presented on electron-doped high-T_c cuprates utilizing $Nd_{2-x}Ce_xCuO_{4-y}$/Au/Nb zigzag junctions. The critical current densities of these Josephson contacts are considerably larger than the grain boundary contacts employed so far for phase-sensitive experiments on the electron-doped high-T_c cuprates. To address controversial questions of whether the pairing symmetry changes away from optimal doping, the pairing symmetry tests are also performed on overdoped $Nd_{2-x}Ce_xCuO_{4-y}$ samples. It is found that for the optimally doped and overdoped $Nd_{2-x}Ce_xCuO_{4-y}$ a clear predominant $d_{x^2-y^2}$-wave behavior is observed at $T = 4.2$ K. Another issue is the possible pairing symmetry transition from $d_{x^2-y^2}$-wave symmetry at $T \geq 3$ K to s-wave symmetry at $T \leq 2$ K. Investigations at $T = 1.6$ K present no indications for such a change to a predominant s-wave symmetry with decreasing temperature.

5.1 Introduction

The determination of the order parameter symmetry in the high temperature superconductors is an important step towards the identification of the mechanism of superconductivity in these materials. This includes its dependencies on the sign and density of the mobile charge carriers, on temperature and possible other parameters. For the hole-doped high temperature superconductors, such as $YBa_2Cu_3O_{7-\delta}$, a long-lasting debate on the order parameter symmetry was settled by the clear $d_{x^2-y^2}$-wave behavior displayed in various phase-sensitive symmetry test experiments, as reviewed

in [26, 34]. This result was confirmed by phase sensitive test experiments utilizing zigzag $YBa_2Cu_3O_{7-\delta}$/Nb Josephson junction [17], as described in Chapter 4.

For the electron-doped materials, $Ln_{2-x}Ce_xCuO_{4-y}$, with Ln = La, Nd, Pr, Eu or Sm, $y \approx 0.04$, only a few phase-sensitive test experiments have until now been reported, all are based on grain boundary Josephson junctions. Tsuei and Kirtley [26, 94] described the spontaneous generation of half-integer flux quanta in $Nd_{1.85}Ce_{0.15}CuO_{4-y}$ and $Pr_{1.85}Ce_{0.15}CuO_{4-y}$ tricrystalline films at temperature $T = 4.2$ K, presenting evidence for a $d_{x^2-y^2}$-wave order parameter symmetry. A similar conclusion was drawn by Chesca *et al.* [95] from the magnetic field dependence of the critical current for grain boundary-based π-SQUIDs in near optimally doped $La_{2-x}Ce_xCuO_{4-y}$, also at $T = 4.2$ K.

In contrast to these phase-sensitive experiments, a substantial volume of more indirect symmetry test experiments exist for the electron-doped materials. The conclusions from these studies are varying. Behavior in line with an *s*-wave, or more general a nodeless, symmetry was reported *e.g.*, from the absence of a zero-bias conductance peak in $Nd_{1.85}Ce_{0.15}CuO_{4-y}$ tunneling spectra at $T \geq 4.0$ K [96–98] and from the temperature dependencies of the London penetration depth in $Pr_{1.855}Ce_{0.145}CuO_{4-y}$ for 1.6 K $< T <$ 24 K [99], in $Pr_{2-x}Ce_xCuO_{4-y}$ with varying Ce-content ($0.115 \leq x \leq 0.152$) for 0.5 K $< T$ [100], and in $Nd_{1.85}Ce_{0.15}CuO_{4-y}$ for 1.5 K $< T <$ 4 K [101], in addition to several earlier studies [102–104]. On the other hand, *d*-wave like characteristics were reported *e.g.*, from the observed gap-anisotropy in angle resolved photoemission spectroscopy on $Nd_{1.85}Ce_{0.15}CuO_{4-y}$ at $T = 10$ K [105, 106], the temperature dependence of the London penetration depth in optimally doped $Pr_{2-x}Ce_xCuO_{4-y}$ and $Nd_{2-x}Ce_xCuO_{4-y}$ (0.4 K $< T$) [107, 108] and from the observation of zero-bias conductance peaks in optimally doped $Nd_{1.85}Ce_{0.15}CuO_{4-y}$ ($T = 4.2$ K) [109] and $La_{1.855}Ce_{0.105}CuO_{4-y}$ for 4.2 K $< T <$ 29 K [110].

Recently, a transition from *d*-wave behavior for underdoped materials to *s*-wave like behavior for the optimally doped and overdoped compounds was reported from the temperature dependence of the London penetration depth in $Pr_{2-x}Ce_xCuO_{4-y}$ and $La_{2-x}Ce_xCuO_{4-y}$ [99] and from the point contact spectroscopy [111, 112]. Further, Balci *et al.* [113] suggested a temperature-dependent change in the order parameter symmetry for optimally and overdoped $Pr_{2-x}Ce_xCuO_{4-y}$, with *s*-wave behavior at $T = 2$ K and *d*-wave behavior at $T \geq 3$ K, based on specific heat measurements.

In view of this still ongoing discussion, there is a need for further phase-sensitive experiments, specifically to study possible changes with temperature and doping. Tsuei and Kirtley [94] and Chesca *et al.* [95] succeeded in performing the first phase-sensitive measurements on the electron-doped compounds based on grain boundary junctions. A complicating factor in the phase-sensitive experiments conducted so far is the geometrical restriction set by the use of the tricrystalline or tetracrystalline substrates, and the intrinsically low critical current density of grain boundaries in the electron-doped materials. This results for example in rather large values of the Josephson penetration depth, which determines the spatial distribution of the half integer flux quantum in the tricrystal experiment, leading to small signal amplitudes [94]. This makes such experiments very challenging, especially for investigation on non-optimally doped compounds. For the SQUID-based experiment discussed in Ref. [95]

the low grain boundary critical current densities required the use of rather thick films (0.5 μm) and wide junctions (500 μm) to reach measurable levels of the critical current. For further detailed studies, it is therefore advantageous to explore other Josephson junction configurations, with potentially higher critical current densities. In addition, it would be very fruitful to choose a configuration for the symmetry test-experiment in which a large Josephson penetration depth presents an advantage rather than a difficulty. Both aspects are fulfilled in the experiment based on zigzag-shaped Josephson contacts between $Nd_{2-x}Ce_xCuO_{4-y}$ and Nb, separated by a Au barrier layer, described in the following.

5.2 $Nd_{2-x}Ce_xCuO_{4-y}$/Au/Nb zigzag junctions

The zigzag-configuration [Fig. 5.1 (a)] has been described in detail in Chapter 4, where it was used to investigate symmetry admixtures to the predominant $d_{x^2-y^2}$-wave symmetry in $YBa_2Cu_3O_{7-\delta}$ and to model the faceting in the high-T_c grain boundaries. In these structures, all interfaces are aligned along one of the $\langle 100 \rangle$-directions of the cuprate, and are designed to have identical values of the critical current densities J_c. With the high-T_c cuprate being an s-wave superconductor, the zigzag-structure presents no significant difference to the case of a straight junction aligned along one of the facet's directions. With the high-T_c superconductor having a $d_{x^2-y^2}$-wave symmetry, the facets oriented in one direction experience an additional π-phase difference compared to those oriented in the other direction. For a given number of facets, the characteristic of these zigzag structures then depend on the

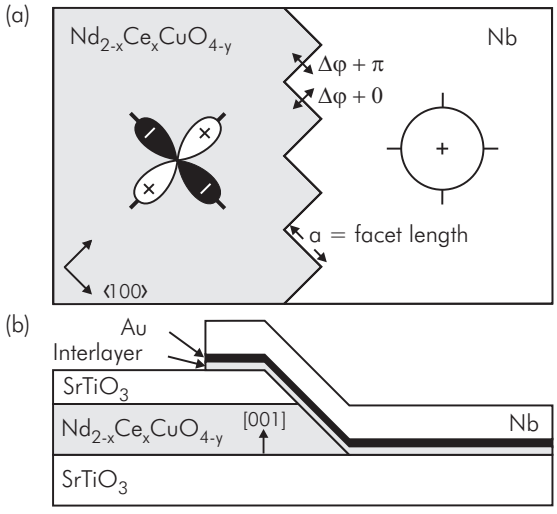

Figure 5.1: (a) Schematic topview of a $Nd_{2-x}Ce_xCuO_{4-y}$/Nb zigzag structure with facet-length a. (b) Schematic sideview illustrating the ramp-type $Nd_{2-x}Ce_xCuO_{4-y}$/Nb Josephon junction.

ratio of the facet length a and the Josephson penetration depth λ_J (see Chapter 4 and 6 and Ref. [83] for more discussion). In the small facet limit, $a \ll \lambda_J$, the zigzag structure can be envisaged as a one-dimensional array of Josephson contacts with an alternating sign of J_c, leading to anomalous magnetic field dependencies of the critical current, as displayed for $YBa_2Cu_3O_{7-\delta}$ in Chapter 4. In the large facet limit, the energetic ground state includes the spontaneous formation of half-integer magnetic flux quanta at the corners of the zigzag structures, as will be discussed in Chapter 6 and 7. All experiments on $Nd_{2-x}Ce_xCuO_{4-y}$ described below are in the small facet limit.

Figure 5.1 (b) schematically shows the $Nd_{2-x}Ce_xCuO_{4-y}$/Nb ramp-type junctions that were used for the experiments. The fabrication procedures have been described in Chapter 3. Both the optimally-doped and overdoped samples were prepared with a bilayer of 150 nm [001]-oriented $Nd_{2-x}Ce_xCuO_{4-y}$ and 35 nm $SrTiO_3$ and with a 160 nm Nb top electrode. For the optimally doped films a $Nd_{1.85}Ce_{0.15}CuO_4$ target, and for the overdoped cases a $Nd_{1.835}Ce_{0.165}CuO_4$ target is used. A 12-nm $Nd_{2-x}Ce_xCuO_{4-y}$ interlayer and a 12-nm Au barrier were employed for both the optimally doped and overdoped samples. In addition to zigzag structures with different size and number of facets, every chip contained several straight reference junctions oriented parallel to one of the facet directions.

The $Nd_{1.85}Ce_{0.15}CuO_4$ films had a typical critical temperature T_c of 20 K, and the $Nd_{1.835}Ce_{0.165}CuO_4$ had a T_c of 13 K. The critical temperatures and corresponding cerium doping levels for the optimally doped and overdoped films used in the measurements were consistent with the known phase diagram of the doping dependence of T_c for electron-doped superconductors [114].

5.3 Measurement results

The junctions were characterized by measuring the current-voltage (IV) characteristics and the dependencies of the critical currents I_c on applied magnetic field H_a, using a four-probe method with the magnetic field parallel to the [001]-direction of the $Nd_{2-x}Ce_xCuO_{4-y}$ in a well-shielded cryostat at $T = 4.2$ K and $T = 1.6$ K, as described in Section 3.2.1. For the determination of the critical currents of the structures, a typical voltage criterion of $V_c \lesssim 2\ \mu$V was used. This set a lower limit of V_c/R_n to the determination of I_c, with R_n being the junctions' normal state resistance.

Optimally-doped $Nd_{2-x}Ce_xCuO_{4-y}$ ($x = 0.15$)

Figure 5.2 (a) shows the $I_c(H_a)$-dependence recorded for a 50 μm wide straight $Nd_{1.85}Ce_{0.15}CuO_{4-y}$/Nb reference junction at $T = 4.2$ K, and in Fig. 5.2 (b) its zero-field IV-characteristic. The $I_c(H_a)$-dependence closely resembles a Fraunhofer pattern, which is the hallmark of small rectangular junctions with homogeneous current distributions. A maximum $I_c = 2.2\ \mu$A at zero applied field was found. Similarly to the graphs shown for the $YBa_2Cu_3O_{7-\delta}$-based junction in Chapter 4, the black areas in the peaks of the $I_c(H_a)$ curves are indicative for the hysteresis in the IV-characteristics. At $T = 4.2$ K, this junction has a typical critical current density of

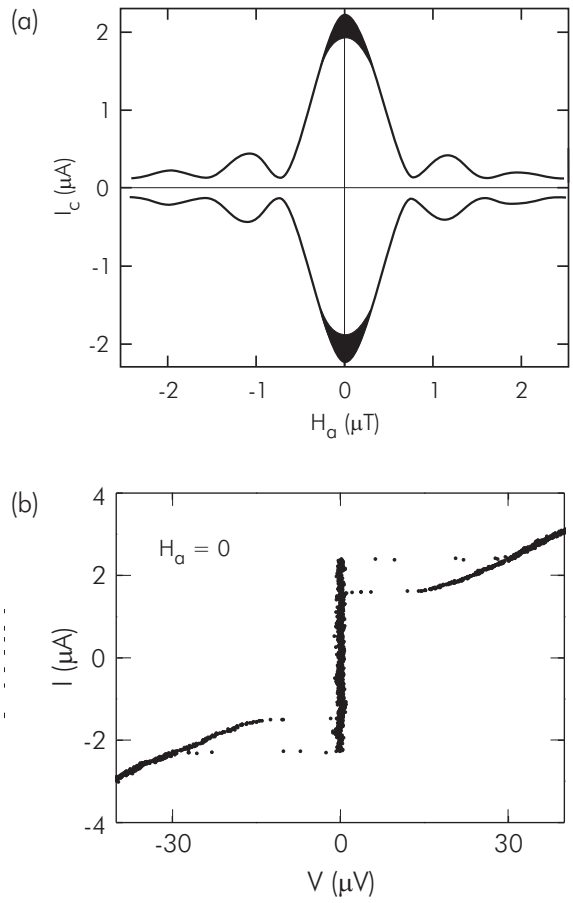

Figure 5.2: (a) Critical current I_c as a function of applied magnetic field H_a for a 50 μm wide straight $Nd_{1.85}Ce_{0.15}CuO_4$/Nb ramp-type junction ($T = 4.2$ K). The dark areas correspond to the hysteresis in the current-voltage characteristic shown for $H_a = 0$ in (b).

$J_c = 29$ A/cm^2, where junction area A is defined by the $Nd_{2-x}Ce_xCuO_4$-film thickness times the junction width. This J_c is several times larger than that is attainable with grain boundary junctions. From this J_c value, the Josephson penetration depth for this sample is estimated to be $\lambda_J = 65$ μm. With this, all the zigzag junctions are well in the small facet limit. The Josephson penetration depth is estimated using Eq. 2.27, where the effective magnetic thickness t is calculated using the $Nd_{2-x}Ce_xCuO_{4-y}$ and Nb London penetration depth presented in Table 2.2 and corrected using Eq. 2.22. The normal-state resistance R_n for this junction is 13 Ω, which gives an I_cR_n product of about 30 μV and $R_nA = 1.0 \times 10^{-6}$ Ωcm^2.

The $I_c(H_a)$-dependence for a $Nd_{1.85}Ce_{0.15}CuO_4$/Nb zigzag junction having 8

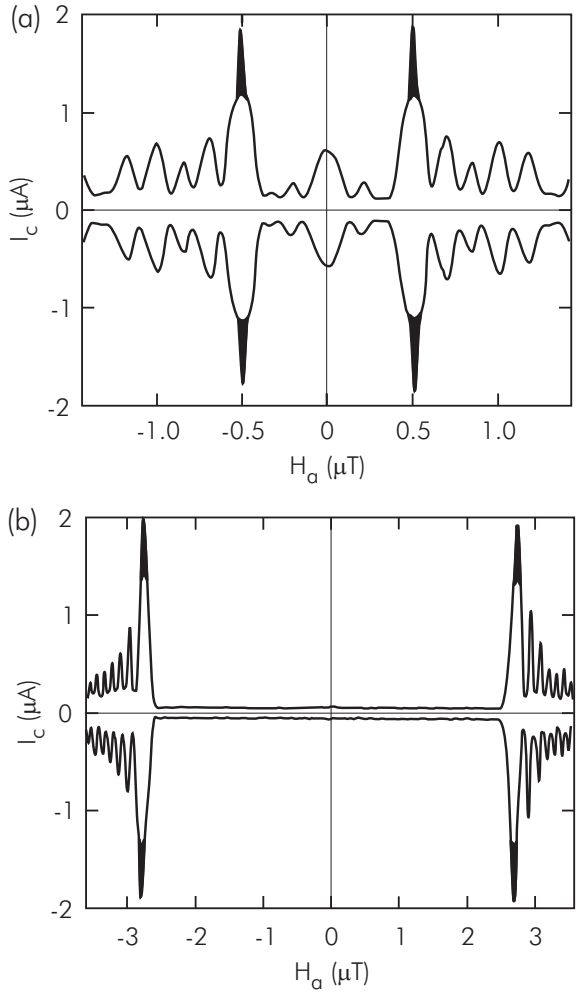

Figure 5.3: Critical current I_c as a function of applied magnetic field H_a for (a) a $Nd_{1.85}Ce_{0.15}CuO_4$/Nb zigzag array comprised of 8 facets of 25 μm width and (b) a similar array with 80 facets of 5 μm width ($T = 4.2$ K).

facets of 25 μm width is presented in Fig. 5.3 (a). Instead of an I_c-maximum at $H_a = 0$, a maximum I_c of 1.8 μA at $H_a = 0.5$ μT can be observed. This zigzag junction shows a highly symmetric $I_c(H_a)$ pattern for both polarities of the current bias and applied magnetic field. The critical current at $H_a = 0$ falls to less than 32% of its peak value. Presuming that J_c for this junction is equal to the reference junction described above, the zero field I_c is only 7% of the expected value for an equally long straight junction, disregarding the wide-junction effects. It should be noted that also the maximum I_c at $H_a = 0.5$ μT is $2 - 3$ times lower than that is expected based

on the J_c of the straight junction. As was shown by Zenchuk and Goldobin [83], a zigzag structure with an odd number of corners is expected to produce spontaneous magnetic flux for all facet-lengths. As the $I_c(H_a)$-dependence of Fig. 5.3 (a) is still strongly non-Fraunhoferlike, this spontaneous flux is expected to be smaller than a half-flux quantum per facet length (see Chapter 6 for more discussion). Nevertheless, the considerable I_c-value at $H_a = 0$ and the reduced peak height at $H_a = 0.5$ μT may be caused, at least partly, by this spontaneous flux.

In Fig. 5.3 (b), the $I_c(H_a)$-dependence for a zigzag array with 80 facets having a substantially smaller facet length of 5 μm is shown, presenting a maximum $I_c = 2.0$ μA at $H_a = 2.8$ μT. Also for this very dense zigzag structure, the $I_c(H_a)$-dependence is highly symmetric. A very low ratio of 2% between the critical current at zero magnetic field and the maximal critical current is found, and the zero field value is less than 0.5% of the expected value for the equivalently long straight junction.

The field dependencies of the critical currents of these zigzag structures clearly exhibit the characteristic features also seen for the $YBa_2Cu_3O_{7-\delta}$ case, as shown in Chapter 4, namely the absence of a global maximum at $H_a = 0$ and the sharp increase in the critical current at a given applied magnetic field. This behavior can only be explained by the facets being alternatingly biased with or without an additional π-phase change. This provides a direct evidence for a π-phase shift in the pair wave function for orthogonal directions in momentum space and thus for a predominant $d_{x^2-y^2}$ order parameter symmetry.

From the calculated J_c and λ_J mentioned above, the junctions are estimated to be in the small facet limit. The self field effect is expected to be highly reduced. This is manifested itself in highly symmetric $I_c(H_a)$-dependencies for all the junctions on the sample. The variation in the Josephson critical current densities between the facets is also expected to be relatively small. This can be seen from a relatively low zero-field-peak of the $I_c(H_a)$-dependencies. For the same reason, the variation in the facet length is estimated to be very low. A high variation in both parameters (facet length and critical current density) will lead to a significantly-increased zero-field peak. This increased zero-field value can also be induced by an additional real s-wave admixture to the dominant $d_{x^2-y^2}$-wave of the order parameter symmetry in the $Nd_{1.85}Ce_{0.15}CuO_4$ electrode. Since $Nd_{2-x}Ce_xCuO_{4-y}$ has a tetragonal structure, *i.e.*, $a = b$, an additional real s-wave admixture to the pairing symmetry is not expected to emerge in this material.

If the order parameter were to comprise an imaginary s-wave admixture, the $I_c(H_a)$-dependencies for the zigzag junctions would be expected to display distinct asymmetries, especially for low fields, as discussed in Chapter 4. In addition, the critical current at zero applied field is expected to increase with the fraction of s-wave admixture. From the high degree of symmetry of the measured characteristics of Figs 5.3 (a) and 5.3 (b) and the very low zero field I_c, no sign of an imaginary s-wave symmetry admixture to the predominant $d_{x^2-y^2}$ symmetry can be distinguished.

Overdoped $Nd_{2-x}Ce_xCuO_{4-y}$ ($x = 0.165$)

To investigate a possible change of the order parameter symmetry with doping, similar zigzag structures using $Nd_{1.835}Ce_{0.165}CuO_4$/Nb junctions were fabricated.

Figure 5.4 (a) shows the $I_c(H_a)$-dependence measured at $T = 4.2$ K for a $Nd_{1.835}Ce_{0.165}CuO_4$/Nb zigzag junction with 8 facets of 25 μm width. This result was registered using voltage criterion $V_c = 0.5$ μV at $T = 4.2$ K. Clearly one can observe a maximum I_c of 2.4 μA at $H_a = 0.75$ μT. This zigzag junction shows also a highly symmetric $I_c(H_a)$ pattern for both polarities of current bias and applied magnetic field. The critical current at $H_a = 0$ falls to less than 23% of its peak value. Obviously, also these characteristics indicate a predominant $d_{x^2-y^2}$-wave symmetry.

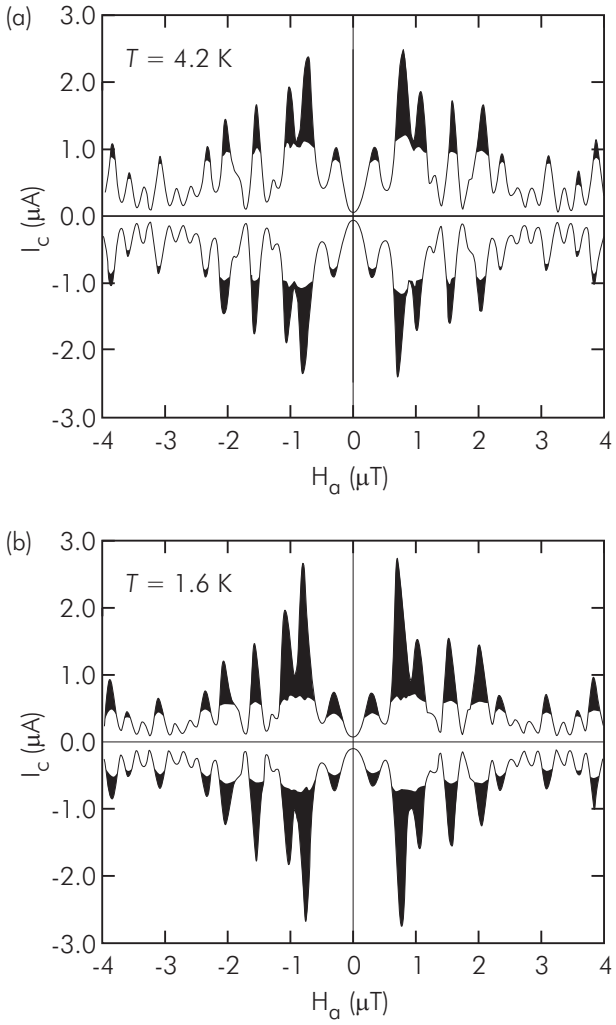

Figure 5.4: Critical current I_c as a function of applied magnetic field H_a for a $Nd_{1.835}Ce_{0.165}CuO_4$/Nb zigzag array comprised of 8 facets of 25 μm width, measured at (a) $T = 4.2$ K, and (b) $T = 1.6$ K.

The sign change of the $d_{x^2-y^2}$-wave symmetry is the dominant effect determining the $I_c(H_a)$-dependencies of this zigzag junction. A lower zero-field value and the symmetry of the pattern around zero applied magnetic field are indications that there is no transition to an s-wave symmetry.

Temperature dependence of the pairing symmetry

A possible temperature-dependent change in the order parameter symmetry for optimally doped and overdoped $Nd_{2-x}Ce_xCuO_{4-y}$ was investigated by lowering the measurement temperature to 1.6 K [113]. This is the temperature range over which a change in the order parameter symmetry is expected, as reported for $Pr_{2-x}Ce_xCuO_{4-y}$ from specific heat measurements [113].

Figure 5.4 (b) presents the $I_c(H_a)$-dependence of the same zigzag junction as presented in Section 5.3 with 8 facets of 25 μm width measured at 1.6 K. The pattern has maximum peaks appearing at ± 0.75 μT applied magnetic field. The pattern at 1.6 K is characterized by a larger maximum of $I_c = 2.8$ μA and a larger hysteresis in the current voltage characteristics than that at $T = 4.2$ K. It is clear that when cooling down the samples to $T = 1.6$ K all the basic features displayed by the structures at $T = 4.2$ K remain unaltered. The very minor asymmetries in the pattern, *e.g.*, between the second maxima, are unchanged with temperature indicating that they may originate from an artifact error in the measurements such as the stray field or trapped flux away from the junction.

From this, it can be concluded that there is no indication for an order parameter symmetry crossover for $Nd_{1.85}Ce_{0.15}CuO_{4-y}$ in this temperature range, as was recently reported for $Pr_{2-x}Ce_xCuO_{4-y}$ [113]. A similar result for an optimally doped sample was observed, when cooling down this sample to $T = 1.6$ K all the basic features displayed by the structures at $T = 4.2$ K remain unaltered as well.

5.4 Concluding remarks

In conclusion, phase-sensitive order parameter symmetry test experiments based on $Nd_{2-x}Ce_xCuO_{4-y}$-Nb zigzag junctions were performed. The results provide clear evidence for a predominant $d_{x^2-y^2}$ order parameter symmetry in the $Nd_{2-x}Ce_xCuO_{4-y}$. This corroborates the conclusions of studies performed with grain boundary junctions in the optimally doped compounds. To verify various recent reports on possible order parameter changes with overdoping and with decreasing temperature, the influence of those parameters has been studied. No change in the symmetry was observed when overdoping the $Nd_{2-x}Ce_xCuO_{4-y}$ compound. Further, the order parameter symmetry was found to remain unaltered between $T = 1.6$ K and $T = 4.2$ K.

Because of the larger J_c's as compared to grain boundary junctions, the cuprate-Nb zigzag configuration presents a good instrument for further detailed order-parameter symmetry test experiments. This may include a comparison between $Nd_{2-x}Ce_xCuO_{4-y}$ and other electron-doped compounds such as $Pr_{2-x}Ce_xCuO_{4-y}$ and $La_{2-x}Ce_xCuO_{4-y}$.

Chapter 6

Half-integer flux quantum effects in 1-d π-ring arrays

In chapters 4 and 5, one-dimensional arrays of 0-π Josephson junctions in a zigzag configuration are considered, in which their facet-length is noticeably smaller than the Josephson penetration depth. In that case, the sign difference between the currents flowing through the 0- and π-facets causes a cancelation of the critical current at zero magnetic field. This results in a strongly modified magnetic field dependence of the critical current as compared to that for a conventional Josephson junction in the absence of π-phase shifts. The latter case is characterized by the well-known Fraunhofer-like magnetic field dependence of the critical current.

Intriguingly, under certain conditions, the built-in π-phase shift in 0-π junctions can result in a phenomenon of spontaneous magnetization, even in the absence of a bias current or an applied field. In the limit of the facet-length being much larger than the Josephson penetration depth, the 0-π junction has a doubly degenerate time-reversed ground state, which is characterized by a spontaneous generation of a half magnetic-flux quantum, with a magnitude of $\frac{1}{2}\Phi_0$ ($\Phi_0 = h/2e = 2.07 \times 10^{-15}$ Wb). In this case, the self-generated half magnetic-flux quantum can be associated with an additional π-phase-shift. The magnetic field dependence of the critical current of the 0-π junction then effectively changes and becomes identical to those for a conventional junction in a large facet limit. In this chapter, investigations on half magnetic-flux quantum effects in various 0-π zigzag junctions will be presented.

6.1 Introduction

A system with a spontaneous current and magnetic flux ground state was proposed first by Bulaevskii *et al.* [61] when considering a superconducting ring with a Josephson junction containing magnetic impurities. The spontaneous current emerges due to a phase slip relating to a spin-flip scattering by magnetic impurities. Geshkenbein, Larkin, and Barone [2, 3] proposed a new vortex state of half magnetic-flux quanta which can exist at the domain walls between different degenerate superconducting

states in multicrystals, depending on the symmetry properties of the order parameter in the superconducting phases. This half magnetic-flux quantum state is energetically favored and it exists at the intersection of the three boundaries between three crystal grains even in the absence of externally applied magnetic fields. In the context of high-T_c superconductors with a $d_{x^2-y^2}$-wave order parameter symmetry, Sigrist and Rice [4, 115] proposed a structure which could lead to this spontaneous generation of half magnetic-flux quanta. The structure proposed by Sigrist and Rice [4, 115] was a superconducting ring comprising two Josephson junctions between a high-T_c and a low-T_c superconductor.

6.1.1 Spontaneous flux in π-rings

In a Josephson junction, the phases of the order parameters of both electrodes simply adjust to minimize the Josephson coupling energy, $\propto -\cos(\varphi_2 - \varphi_1)$, by setting the phase difference, $\varphi_2 - \varphi_1$, equal to $n2\pi$, with n an integer. In exception for Josephson contacts along the nodal directions of the d-wave symmetry, therefore, the connection by a single straight and smooth junction between two d-wave superconductors or between a d-wave and an s-wave superconductor does not, by itself, lead to any special observable effects but a conventional Josephson effect. On the other hand, an intriguing effect, the spontaneous generation of half-integer magnetic-flux quanta, can be expected to arise in coupled Josephson junctions involving superconductors with a d-wave symmetry. This can be understood by considering a superconducting ring with two facets between a $d_{x^2-y^2}$-wave and an s-wave superconductor as depicted in Fig. 6.1. The $d_{x^2-y^2}$-wave symmetry in the high-T_c superconductor segment of the ring introduces a π-phase-shift between the two junctions in the ring. In such a system there is no way to simultaneously minimize the energy of both junctions, and at the same time, to keep no phase gradient in the superconductors. The system has to choose whether it is favorable to keep zero phase gradient in the superconductors and to pay the maximal energy loss at the junction, or whether it is favorable to lower the junction energy at the expense of a phase gradient in the superconductor. This means frustration for this loop, and consequently such a loop will be referred to as a frustrated loop or a π-ring. The phase gradient physically means the existence of a finite current, and thus a spontaneous magnetic-flux. Because of the relationship between the enclosed flux and the quantum-phase in a superconducting ring, the spontaneous flux provides a further π-phase change between the facets, leading to a lowering of the Josephson coupling energy. This will be discussed in more details in the following.

As described in Chapter 2, the superconducting order parameter $|\Psi|e^{i\varphi}$ must be a single-valued function, and its phase φ is allowed to wind only by an integral multiple of 2π when going around a closed contour, leading to the fluxoid quantization in a superconducting ring. This means that the fluxoid has to be an integer multiple of flux quanta $n\Phi_0$ ($n = 0, 1, 2, ...$). For a superconducting ring incorporating N junctions, the fluxoid condition can be described as

$$\Phi_a + I_s L + \frac{\Phi_0}{2\pi} \sum_{i=1}^{N} \phi_i = n\Phi_0 \tag{6.1}$$

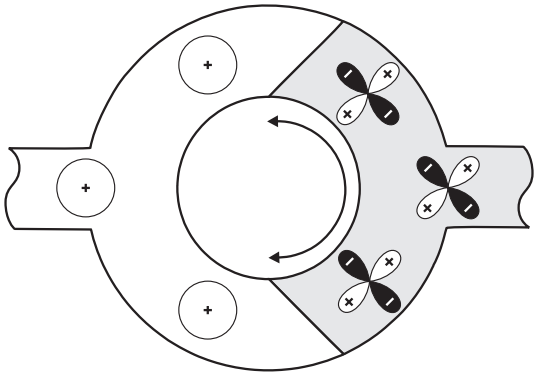

Figure 6.1: Sketch of a superconducting π-ring consisting of a 0- and π-facet from combination of a $d_{x^2-y^2}$-wave and an s-wave superconductor.

where ϕ_i is the phase difference across the junction i, Φ_a the applied flux, L the self-inductance, and I_s the circulating current.

The groundstate properties of the frustrated system can be determined by considering the free energy of a π-ring with one junction, given by [4, 115]

$$F(\Phi, \Phi_a) = \frac{\Phi_0^2}{2L}\left\{\left(\frac{\Phi - \Phi_a}{\Phi_0}\right)^2 - \left(\frac{L|I_c|}{\pi\Phi_0}\cos\left(\frac{2\pi}{\Phi_0}\Phi + \theta\right)\right)\right\} \tag{6.2}$$

where $\Phi = \Phi_a + LI_s$ is the total magnetic flux threading through the loop, and the phase shift $\theta = 0$ or π corresponds to an absence or a presence of a π-phase shift in the ring, respectively. The circulating current I_s as a function of applied field can be obtained by minimizing F with respect to I_s, and this leads to

$$\frac{I_s}{|I_c|} = -\sin\left(\frac{2\pi}{\Phi_0}\Phi_a + \gamma\frac{I_s}{|I_c|} + \theta\right) \tag{6.3}$$

where the dimensionless parameter $\gamma = 2\pi L|I_c|/\Phi_0$. The dependencies of the circulating supercurrent on applied fields are depicted in Fig. 6.2 (a) for a 0-ring, and in Fig 6.2 (c) for a π-ring. The dashed lines are for $\gamma = 0.4$, and solid lines for $\gamma = 2.0$. The ground state properties of the systems are determined by γ. For $\gamma < 1$, the I_s's for both 0- and π-ring are single-valued periodic functions. However, in a small applied field, the shielding currents oppose the applied flux for the 0-ring but are aligned with the applied flux for the π-ring. If $\gamma > 1$, then for the 0-ring I_s is multi-valued near $\Phi_a = \Phi_0/2$, and for π-ring near $\Phi_a = 0$. The π-ring has a spontaneous magnetization which is aligned with a small externally applied field. In general, as the junctions grow stronger ($\gamma \geq 1$), it is favorable for a π ring to lower its energy at the expense of a phase gradient in the superconductors which means the existence of a spontaneous finite current.

At zero applied field $\Phi_a = 0$, and for very large I_c, the circulating supercurrent

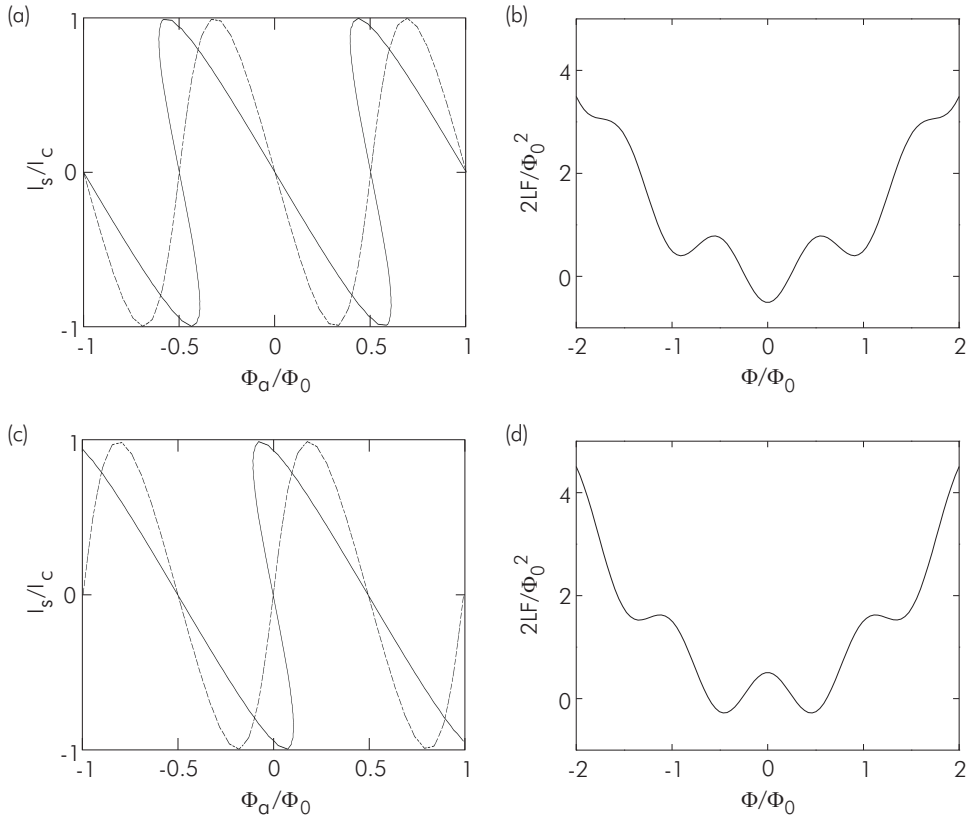

Figure 6.2: Circulating current as a function of applied field for (a) a 0-ring and (c) a π-ring. The dashed lines are for $\gamma = 0.4$, and the solid lines for $\gamma = 2.0$. The free energy of the systems as a function of total flux ($\gamma = 10$) in the ring for (b) a 0-ring and (d) a π-ring. The π-ring has a doubly degenerate ground state which is characterized by a spontaneous generation of half-integer flux-quanta at zero applied field.

for a π-ring ($\theta = \pi$) in Eq. 6.3 can be approximated by

$$I_s \simeq \frac{\mp\pi I_c}{\gamma + 1} = \frac{\mp\pi}{\dfrac{2\pi L}{\Phi_0} + \dfrac{1}{I_c}} \tag{6.4}$$

Providing that $LI_c \gg \Phi_0$ leads to

$$I_s L \simeq \mp\frac{1}{2}\Phi_0 \tag{6.5}$$

The ground state of a frustrated loop is characterized by a spontaneous current or a corresponding spontaneous magnetization of a half-integer flux-quantum $\frac{1}{2}\Phi_0$ at zero

applied field, providing that $LI_c \gg \Phi_0$. In Fig. 6.2 (b) and (d), the free energy as a function of the total flux Φ in the ring is plotted from Eq. 6.2 for the unfrustrated and frustrated systems, respectively, assuming $\gamma = 10$. The free energy for the unfrustrated system has a stable state centered at $\Phi = 0$, while the frustrated one has a doubly degenerate ground state at $\pm\frac{1}{2}\Phi_0$.

The spontaneous magnetization in a superconducting ring with N junctions in the presence of an odd number of π-phase-shifts has been considered as well by Tsuei and Kirtley [5, 26], leading basically to the same result, as described in the following.

For a π-ring with two junctions as depicted in Fig. 6.1, the fluxoid quantization can be expressed by

$$\Phi_a + I_s L + \frac{\Phi_0}{2\pi} \sum_{i=1}^{2} \phi_i = n\Phi_0 \tag{6.6}$$

where ϕ_i is the phase difference across the junction i. For superconducting loops incorporating Josephson junctions with relatively large I_c's, the circulating supercurrent $I_s = I_{ci} \sin(\phi_i + \theta)$ can be approximated by

$$\frac{I_s}{I_{ci}} \simeq \phi_i + \theta \tag{6.7}$$

where θ again equals to π to represent the π-phase difference between the two junctions in the loop. The circulating supercurrent can be obtained by combining Eq. 6.7 into the flux quantization condition of Eq. 6.6. In the absence of external applied fields and taking $n = 0$ for the ground state of the system, this leads to

$$I_s = \frac{\pi}{2\pi \left(\dfrac{L}{\Phi_0} \right) + \displaystyle\sum_{i=1}^{2} \left(\frac{1}{I_{ci}} \right)} \tag{6.8}$$

and if the condition of $LI_{ci} \gg \Phi_0$ is fulfilled, the π-ring is characterized by a spontaneous generation of a magnetic flux of

$$I_s L \approx \frac{\Phi_0}{2} \tag{6.9}$$

even at zero applied field and bias current, as was the case for the single-junction π-loop described above.

6.1.2 First direct observation

A spontaneously-generated half-integer magnetic-flux quantum has been observed first in a tricrystal ring experiment [5]. The tricrystal geometry has been discussed in Chapter 2. In short, the frustrated three-junction ring is located at the tricrystal meeting point, and as reference two two-junction rings and one ring with no junction are either at the bicrystal grain boundary or not at a grain boundary as shown in Fig. 6.3 (a). The frustrated three-junction ring has a total π-phase change when circulating around the ring due to the $d_{x^2-y^2}$-wave symmetry, and thus a spontaneous magnetization is expected in the ring. The control rings are in a 0-ring configuration

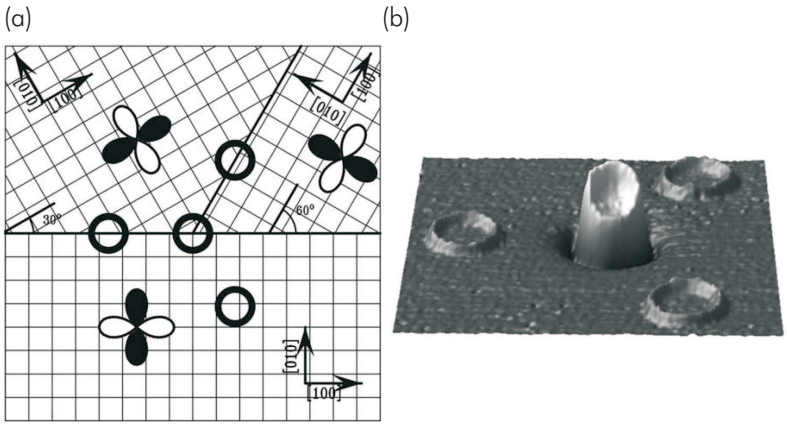

Figure 6.3: (a) Sketch of a tricrystal ring experiment (b) Spontaneous generation of a half-integer magnetic-flux quantum observed in the tricrystal ring experiment (taken from [51]).

(no additional π-phase shift) and should exhibit the standard integer flux quantization.

Figure 6.3 (b) shows a scanning SQUID microscopy image of a tricrystal sample cooled to 4.2 K in a magnetic field estimated to be less than 0.4 μT. It was found that the central frustrated ring has $\frac{1}{2}\Phi_0$ total flux in it, while the control rings contained no magnetic flux. The control rings were visible in the image due to the mutual inductance coupling between the rings and the pick-up SQUID loop.

By using this tricrystal geometry, Tsuei, Kirtley, and co-workers observed a spontaneous generation of a half-integer magnetic-flux quanta in other high-T_c cuprates, such as $GdBa_2Cu_3O_{7-\delta}$ [116], $Tl_2Ba_2CuO_{6+\delta}$ [117], $Bi_2Sr_2CaCu_2O_{8+\delta}$ [118], $Nd_{1.85}Ce_{0.15}CuO_{4-\delta}$ [94], and $Pr_{1.85}Ce_{0.15}CuO_{4-\delta}$ [94], indicating that $d_{x^2-y^2}$-wave pairing symmetry is dominant in all these cuprates.

6.1.3 Spontaneous-flux in zigzag junctions

When the inner diameter of the superconducting π-ring sketched in Fig. 6.1 equals to zero, the ring is reduced to a corner junction. In this case, the π-phase-shift rises between the two adjacent facets. Zigzag arrays can then be regarded as a one-dimensional array of corner junctions. The characteristic value of LI_c/Φ_0 is now substituted by the ratio between facet length a and the Josephson penetration depth λ_J.

The dependencies of the critical current I_c on applied magnetic field H_a for zigzag junctions with facet length $a \ll \lambda_J$ (small-facet limit) have been discussed in Chapter 4 and 5. In short, the $d_{x^2-y^2}$-wave symmetry in the high-T_c superconductor causes a sign difference between the currents flowing through the 0- and π-facet. This results in a cancelation of the critical current at zero magnetic field and in an anomalous

$I_c(H_a)$-dependence. In this short facet limit, a uniform critical current density distribution in the junction is assumed, and the self field effect from the supercurrent can be neglected. However, for facets in the long limit ($a \gg \lambda_J$), this assumption is no longer valid because the presence of the self-field from the supercurrent introduces a perturbation to the phase-difference profile (current density distribution) along the junction, even in zero external applied field. In this case, the total critical current can be calculated by first determining the phase-difference profile along the junction. In the following, the single 0-π (corner) junction will first be considered, after which the analysis will be extended to zigzag arrays comprised of multiple corner junctions.

The electrodynamics of a conventional long limit junction is described by the sine-Gordon equation [30] and has been discussed in detail in [24, 31]. The sine-Gordon equation can be extended to include the effects of π-shifts:

$$\frac{\partial^2 \phi}{\partial x^2} = \frac{1}{\lambda_J^2} \sin\left[\phi(x) + \theta\right] \tag{6.10}$$

where θ is equal to 0 for a 0-facet and π for a π-facet. By using appropriate boundary conditions, this differential equation can be solved numerically such as described for example in Ref. [119]. The free energy for 0-π junctions in the presence of a spontaneous magnetic flux (a vortex solution) is the sum of the Josephson energy and the magnetic energy as

$$F_V = \frac{\Phi_0 J_c h}{2\pi} \int_{-a}^{a} \left[1 - \cos\left[\phi(x) + \theta(x)\right] + \frac{\lambda_J^2}{2}\left(\frac{\partial \phi}{\partial x}\right)^2\right] dx \tag{6.11}$$

while the free energy in the absence of spontaneous magnetic flux (no-vortex solution) is

$$F_0 = \frac{\Phi_0 J_c h}{2\pi} \int_{-a}^{a} [1 - \cos\theta(x)] dx \tag{6.12}$$

The free energy of a single 0-π junction with a linear configuration has been discussed by Xu *et al.* [120] for the limiting case of $a/\lambda_J \to \infty$ and by Kirtley *et al.* [119] for intermediate cases.

The solutions for the free energy of 0-π junctions described in Eq. 6.12 have been calculated numerically using the sine-Gordon equation solver developed by Kirtley *et al.* [121], applying a method as described in Ref. [119]. Figure 6.4 (a) presents the phase difference across the junction as a function of position for various ratios between facet length and the Josephson penetration depth, a/λ_J = 0.5, 1, 2, 4, 8, and 16, for a symmetric 0-π junction. The ratio of the free energy for the solution with spontaneous flux F_V to that with no flux F_0 is plotted as a function of a/λ_J in Fig. 6.4 (b). The solution with spontaneous flux always has a lower energy than the solution with no flux, and thus it is favorable for a symmetric 0-π junction to generate some flux in its ground state. The flux distribution in the 0-π junctions is presented in Fig. 6.4 (c), and the total flux spontaneously-generated in the system in Fig. 6.4 (d). At a large ratio of a/λ_J, the spontaneous generated flux approaches a value of $\frac{1}{2}\Phi_0$.

Kirtley *et al.* [119] also addressed the question of spontaneous flux generation in asymmetric 0-π junctions. They found that in this case the state with no flux has the

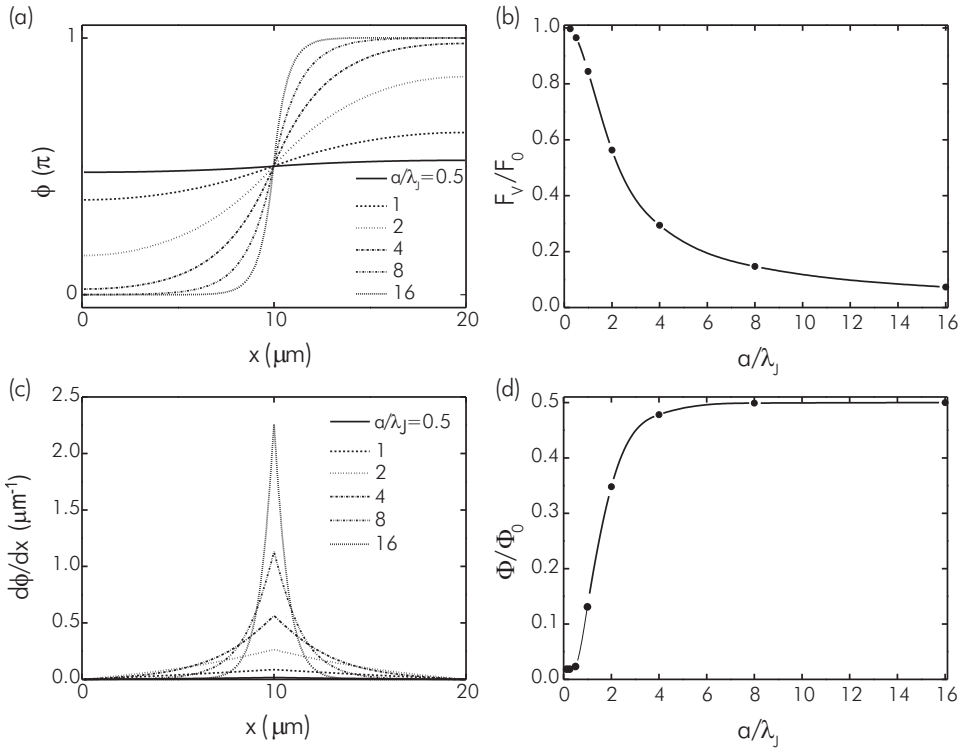

Figure 6.4: (a) Phase difference across the junction, (b) the relative free energy of the system with a spontaneous flux to that with no flux , (c) the distribution of the spontaneous magnetic field, and (d) the total self-generated flux of a 0-π junction for $a/\lambda_J = 0.5,\ 1,\ 2,\ 4,\ 8,$ and 16. In these calculations a is fixed to 10 μm.

lowest free energy for short junctions, and thus there is no spontaneously-generated flux, up to a critical value of $a/\lambda_J \lesssim 1$.

In general, when the facet length is much larger than the Josephson penetration depth ($a/\lambda_J \to \infty$), the spontaneously-generated flux is equal to a half-integer magnetic-flux quantum. In this case, the spontaneous flux can be regarded as an additional π-phase shift, and thus the total additional phase-difference is simply changed to 0 or 2π, depending on the polarity of the spontaneous flux. This means that the π-facet effectively changes into a 0-facet. The $I_c(H_a)$-dependence for 0-π junctions in the presence of the spontaneously-generated half magnetic-flux quantum is then basically identical to the long straight junction. However this approximation is not valid in intermediate case [119]. It has been shown in Ref. [119] that, in an intermediate case up to $a/\lambda_J = 10$, the $I_c(H_a)$-dependence still has a minimum at zero applied field, but its depth has been significantly reduced.

A zigzag junctions is basically an array of corner junctions. Using a similar method to a single 0-π junction [119], the sine-Gordon equation for zigzag junctions can be

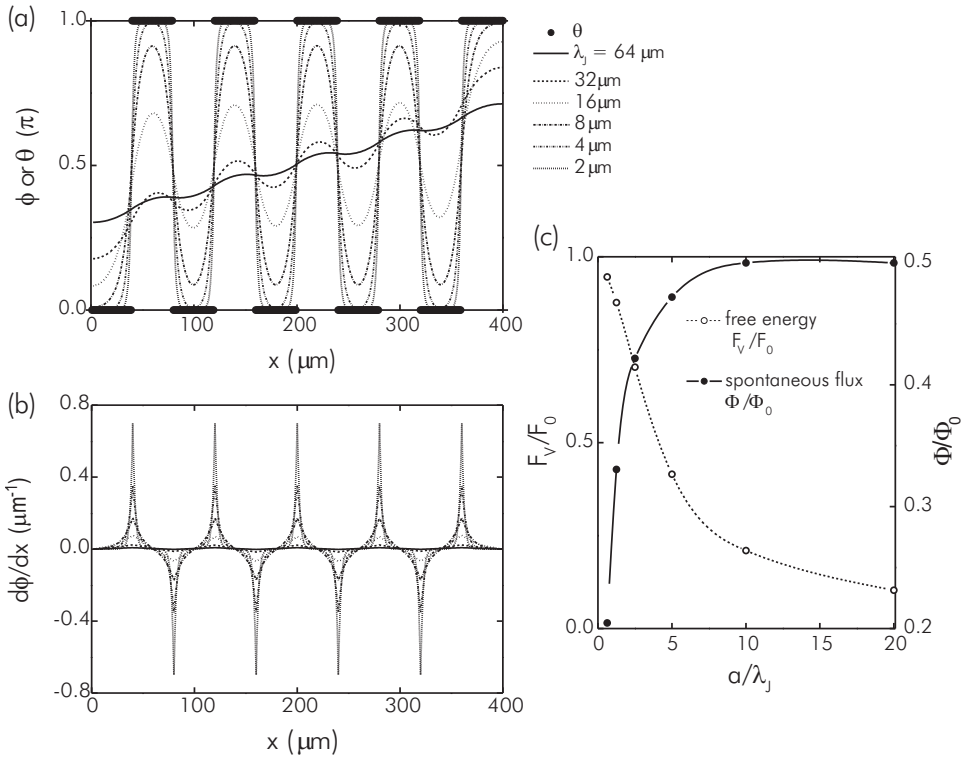

Figure 6.5: (a) Phase and (b) magnetic field as a function of position in a zigzag junction with 9 π-rings for Josephson penetration depth $\lambda_J = 64,\ 32,\ 16,\ 8,\ 4,$ and 2. (c) The relative free energy and total spontaneous flux at each corner of the zigzag junction as a function of ratio between facet-length and Josephson penetration depth.

solved numerically [121]. Figure 6.5 presents a solution of the sine-Gordon equation for a zigzag junction with 10 facets of 40 μm width. The sine-Gordon equation for the zigzag junction is solved for Josephson penetration depth of 64, 32, 16, 8, 4, and 2 μm. Figure 6.5 (a) and (b) show the phase difference and spontaneous flux distribution along the junctions for various Josephson penetration depth values. The relative free energy and the total flux at the corners are presented in Fig. 6.5 (c). The system is always ended up in a perfect antiferromagnetic arrangement of the fractional-fluxes, and the spontaneous fluxes approach a value of $\frac{1}{2}\Phi_0$ when $\lambda_J \approx 4$ μm.

The simulation results therefore suggest that a spontaneously generated half-flux quantum is expected to emerge at every corner of the zigzag junction when $a \gg \lambda_J$. The $I_c(H_a)$-dependence and spontaneous flux measurements on the zigzag samples with $a \gg \lambda_J$ will be presented in Section 6.2. Prior to the measurement results, sample design aspects will be first given.

6.2 Measurement results

To spontaneously generate complete half-integer flux-quanta, the facet-dimensions in the zigzag junctions have to be much larger than the Josephson penetration depth, $a \gg \lambda_J$ (large facet limit). Since the Josephson penetration depth is inversely proportional to the square root of the critical current density, $\lambda_J \sim \sqrt{1/J_c}$, the critical current density has to be relatively large. By adjusting the Au-barrier thickness d, the junction critical current density can be tuned in a wide range from 0.01 kA/cm^2 for $d \sim 120$ nm, up to values approaching 100 kA/cm^2 for $d \sim 7$ nm.

For the experiments discussed in this chapter, the samples were realized from a 150 nm $YBa_2Cu_3O_{7-\delta}$ base electrode and 160 nm Nb top electrode while the Au-barrier thickness is varied between 6 to 12 nm. With this, the critical current density varies between $10 - 100$ A/cm^2. The samples were also designed to comprise zigzag junctions with various facet lengths on a single chip, ranging from 5 μm to 40 μm.

To investigate the spontaneous magnetization effect of half-integer flux-quanta in one-dimensional π-ring arrays (zigzag junctions), various samples have been fabricated. For each sample, transport measurements were performed prior to imaging by a scanning SQUID microscope. Transport measurements include investigations on the $I(V)$-characteristics and the $I_c(H_a)$-dependencies.

6.2.1 The $I_c(H_a)$-dependencies

The $I(V)$-characteristics and the $I_c(H_a)$-dependencies were measured in a helium cryostat at 4.2 K. In this section, experimental data will be presented on a sample consisting of four zigzag junctions of; 80 facets of 5 μm, 10 of 40 μm, 40 of 5 μm, and 8 facets of 25-μm width, four straight junctions of which two are 5-μm and two are 50-μm wide facing either $\langle 100 \rangle$ direction, and two straight junctions of 100- and 200-μm width facing a $\langle 110 \rangle$ direction.

Figure 6.6 shows the $I(V)$-characteristics and the $I_c(H_a)$-dependence for straight junctions at 4.2 K. In Fig. 6.6 (a), the $I_c(H_a)$-dependence for a 5-μm junction is depicted, and in the inset its typical $I(V)$-characteristic at zero applied field. The $I_c(H_a)$-dependence of the 5-μm junction resembles closely the Fraunhofer pattern described by Eq. 2.26, with a maximum in the critical current of $I_c = 0.28$ mA at zero applied magnetic flux. By estimating the effective area for current transport across the junction A to be the thickness of the base electrode h times the width of the junction a ($A = h \times a$), a corresponding critical current density of $J_c = 3.7 \times 10^4$ A/cm^2 is obtained for this 0.15×5 μm^2 junction. From this and by using Eq. 2.27, the Josephson penetration depth λ_J for this sample is estimated to be approximately 2 μm. From the Fraunhofer-like $I_c(H_a)$-dependence of the 5 μm junction, and from the estimated-ratio between junction length and the Josephson penetration depth of $a/\lambda_J \approx 2.5$, it can be concluded that the 5-μm junction is still in the small limit or at least still in the intermediate limit.

The $I_c(H_a)$-dependence for a 50-μm straight junction is presented in Fig. 6.6 (b), and in the inset its $I(V)$-characteristic. For this junction $a/\lambda_J \approx 25$, which implies that the junction is well within the large facet limit. It can be obviously observed in Fig. 6.6 (b) that the $I_c(H_a)$-dependence of this 50-μm junction resembles that

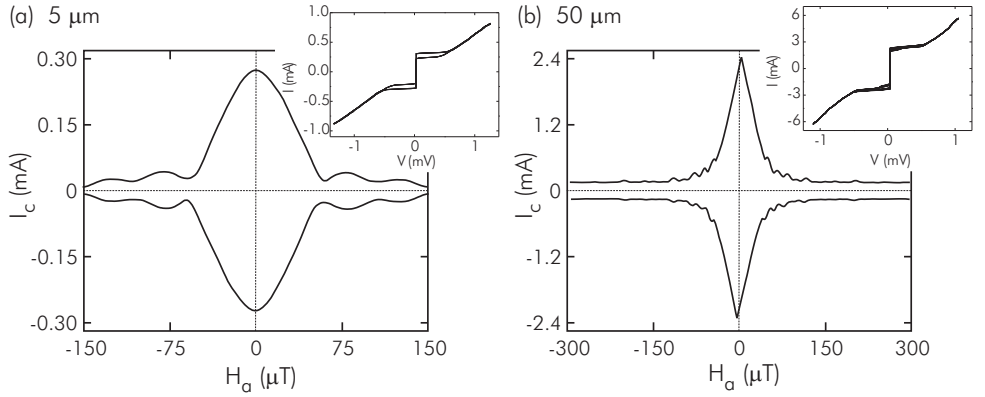

Figure 6.6: The $I_c(H_a)$-dependence for (a) a 5 μm straight junction and (b) a 50 μm straight junction. The typical $I(V)$-characteristic at zero applied field are shown in the insets.

for straight junctions in the large facet limit [31]. The maximum critical currents of $I_c = 2.4$ μm are slightly shifted from zero applied magnetic flux. However, the maxima are symmetric through the point of origin. It has been discussed in detail in [31] and now believed that the self field effect from the supercurrent has resulted in the shifting of the maximum I_c from zero applied field and in a presence of asymmetry of the maxima (and in general the $I_c(H_a)$-dependence) between positive and negative applied fields. However, a symmetry should be observed when both bias current and applied field were simultaneously reversed in polarity, *i.e.* the pattern has a symmetry through the point of origin.

The ratio of I_c between the 50- and 5-μm junction of $I_c(50\ \mu\text{m})/I_c(5\ \mu\text{m}) = 8.6$ is comparable to the ratio between the facet-lengths of both junctions. The reduced I_c from the expected value of 2.8 mA to a value of ~ 2.4 mA for the 50-μm junction is due to the wide junction effects. In addition to this, both junctions are placed ~ 5 mm apart, thus a slightly variation in the Au-barrier thickness is expected, leading to a small variation in the critical current density of both junctions. Furthermore, the flux can be easily trapped in a long junction and thus effectively reducing the critical current at zero applied field. The normal-state resistance R_n for the 5-μm junction is 1.5 Ω, which gives an I_cR_n product of 0.42 mV and $R_nA = 1 \times 10^{-8}$ Ωcm^2. For the 50-μm junction, $R_n = 0.1$ Ω, yielding an I_cR_n of 0.24 mV and R_nA of 7.5×10^{-9} Ωcm^2.

The $I_c(H_a)$-dependencies for $YBa_2Cu_3O_{7-\delta}$/Nb zigzag junctions are presented in Fig. 6.7 for various configurations. For zigzag junctions with 5-μm facet length, it is clear that the maxima in the critical currents were observed at a nonzero applied field as depicted in Fig. 6.7 (a) for an 80-facets junction and (c) for a 40-facets junction. A maximum critical current of $I_c \sim 5$ mA was obtained at $H_a \approx 12.5$ μT for the 80-facets junction. At zero applied field, the critical current has significantly increased to a value of $I_c \sim 2$ mA from a zero expected-value. In contrast to a zigzag junction in the small facet limit for which the critical current at zero applied field is reduced to

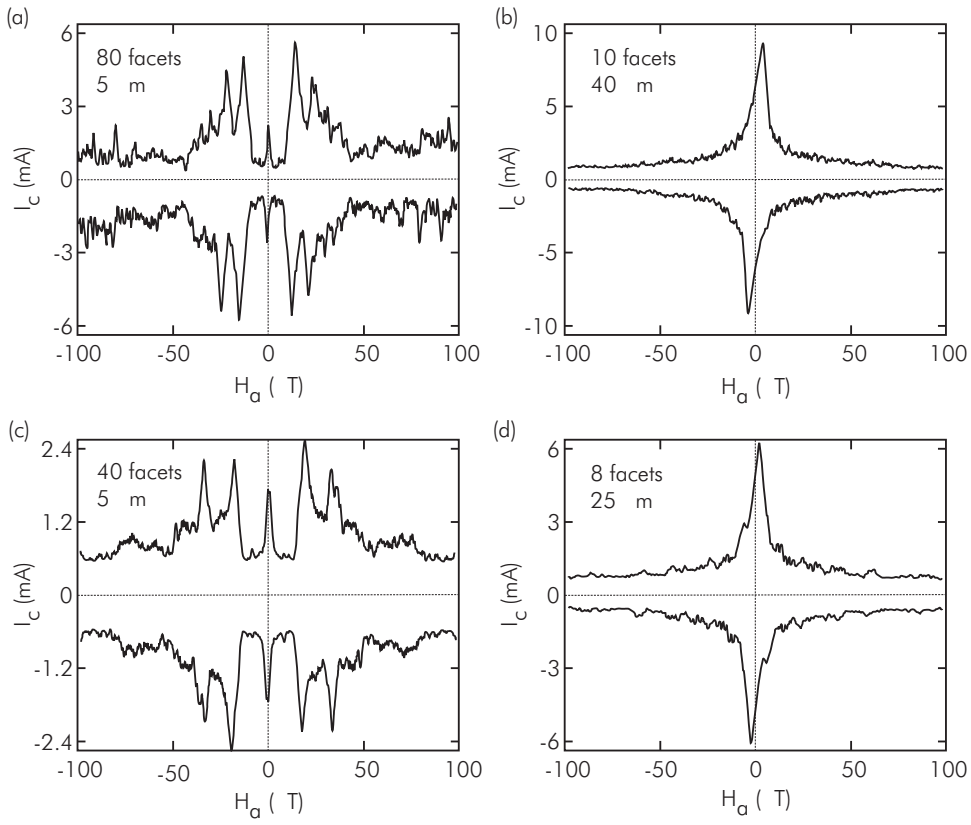

Figure 6.7: The magnetic field dependencies of the critical currents for zigzag junctions with (a) 80 facet of 5 μm width, (b) 10 facet of 40 μm width, (c) 40 facet of 5 μm width, and (d) 8 facet of 25 μm width. For this sample, the Josephson penetration depth $\lambda_J \approx 2$ μm.

a value approaching zero in the absence of disorder in the junctions, the ratio of the critical current at zero field to that at $H_a \approx 12.5$ μT falls to a value of approximately 40%. The significantly increased I_c from the zero expected value at zero applied field is in agreement with the theoretical model for $0 - \pi$ junctions in the intermediate facet limit [119].

Although other possible explanations, such as imperfections in the junctions and a real s-wave admixture component, can not be neglected, the $I_c(H_a)$ patterns for zigzag junctions with $a \ll \lambda_J$ as discussed in Chapter 4 indicate that such components are very small. Furthermore, the $YBa_2Cu_3O_{7-\delta}$ films are twinned on a considerably smaller length scale than the facets. If there is a real s-wave admixture component, its contribution to the supercurrent at zero magnetic field is expected to be averaged out. Therefore, it can be concluded that the zigzag junction with 80 facets of 5 μm width presented in Fig. 6.7 (a) is not well within the small-limit, instead it is still in

the intermediate limit. A similar conclusion can be extracted from the value of the ratio between the facet-length and the Josephson penetration depth of $a/\lambda_J \approx 2.5$, taking λ_J equal to the Josephson penetration depth of the reference junctions.

Figure 6.7 (c) shows a similar pattern for a 40-facet array of 5 μm-facet width, with a maximum I_c of ~ 2.5 mA at $H_a \approx 20$ μT. In this pattern, a minimum with a reduced depth of the critical current $I_c \approx 1.8$ mA at zero applied field can be clearly observed. For this particular junction, the critical current at $H_a = 0$ increases even to approximately 72% of its peak value. These results indicate that some self-generated magnetic flux could be present in the junction. The spontaneous flux and possibly some self-fields may have resulted in the pronounced asymmetry in the $I_c(H_a)$-dependence for both junctions. Remark that from the calculation presented in Ref. [119] the $I_c(H_a)$-dependencies for 0-π junctions still have maxima at a finite applied field and a minimum with a reduced depth at zero applied field even for an a/λ_J-value up to ~ 10. So, the results presented in Fig. 6.7 (a) and (c) are well in agreement with this theoretical prediction.

As the a/λ_J-ratio increases, the critical current at zero field is expected to be higher and the spontaneous flux approaches a value of $\frac{1}{2}\Phi_0$ per corner point. Figure 6.7 plots the $I_c(H_a)$-patterns for larger-facet junctions. A zigzag junction with 10 facets of 40-μm width is presented in Fig. 6.7 (b) and with 8 facets of 25-μm in (d). The $I_c(H_a)$-dependencies show a maximum of $I_c \approx 9$ mA for the 10-facet junction and $I_c \approx 6$ mA for the 8-facet junction. The maximum I_c for both junctions were observed around zero applied field. The patterns have a symmetry through the point of origin, but a symmetry breaking was observed between positive and negative applied fields. Taking $\lambda_J = 2$ μm, the a/λ_J-values are 20 for the 10-facet junction and 12.5 for the 8-facet junction. Both the $I_c(H_a)$-dependence and the a/λ_J-ratios imply that both junctions are well within the wide-facet limit. Since the a/λ_J-ratios for both junctions presented in Fig. 6.7 (b) and (d) are considerably larger than 10, the results are also in well agreement with the theoretical prediction presented in Ref. [119] .

To summarize, a half-integer flux-quantum is spontaneously generated at the corners of a zigzag junction when $a \gg \lambda_J$. The formation of the half-vortices can be regarded as an additional phase of π, and thus the expected $I_c(H_a)$-dependence will be effectively changed and identical to that for a long straight junction. Therefore, a spontaneously generated magnetic flux approaching a value of $\frac{1}{2}\Phi_0$ is expected to be present at every corner of the zigzag junctions with 10 facets of 40 μm width and 8 facets of 25 μm width. Meanwhile, the 80 facets of 5 μm width and 40 facets of 5 μm width junction are expected to generate fractional vortices which are less than a half-integer flux-quantum. The imaging experiments by scanning SQUID microscopy will be presented in the following.

6.2.2 Magnetic imaging by scanning SQUID microscopy

Figure 6.8 (a) shows a scanning SQUID microscopy image of a zigzag array with 10 facets of 40-μm width. In this figure, Niobium is at the bottom-left and $YBa_2Cu_3O_{7-\delta}$ at the top-right corner. The sample was cooled in nominally zero field, and imaged with a 4-μm diameter octagonal pickup loop SQUID at 4.2 K. A spontaneously induced magnetic flux is clearly seen at every corner of the zigzag array. The image

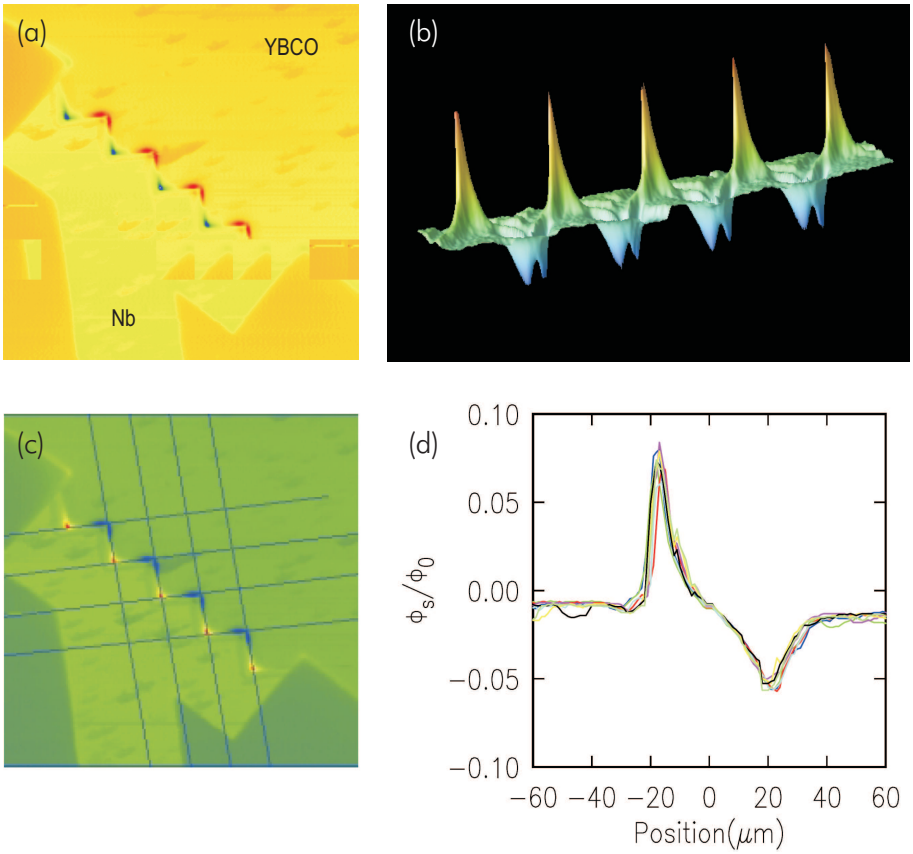

Figure 6.8: [color] (a) Scanning SQUID micrograph of half-integer flux-quanta at the corners of a zigzag structure with 10 facets of 40 μm width. (b) A 3D rendering of (a). (c) The position along the junction where the cross section image of the spontaneous flux in (d) was calculated.

shows that the lowest energy state of the system is characterized by an arrangement of positive (pointing out of the sample surface as shown in red) and negative (pointing into the sample surface as shown in blue) half-vortices on alternate corners (arranged in an antiferromagnetic fashion). This antiferromagnetic ordering was found to be very robust, occurring for many cool-downs and for different samples with comparable geometries. In Fig. 6.8 (b), a three-dimensional rendering of the image is shown with the positive vortices pointing downward. It shows that the half-vortices which are at the Niobium side [presented by blue color in Fig. 6.8 (a) and pointing upward in Fig. 6.8 (b)] are uniformly sharper than the half-vortices at the $YBa_2Cu_3O_{7-\delta}$ side [presented by red color in Fig. 6.8 (a) and pointing downward in Fig. 6.8 (b)]. In addition, the half-vortices at the $YBa_2Cu_3O_{7-\delta}$ site have a distinct dip to them right

at the corner. This dip and the asymmetry between positive and negative vortices is due to the Nb counter electrode overhang on the $YBa_2Cu_3O_{7-\delta}$ base electrode. While the source of the vortices is well localized, the overhanging Nb spreads it out differently between corners at the Nb and $YBa_2Cu_3O_{7-\delta}$ side. Nevertheless, the flux is equal in shape for all the corners which are positioned at the same side. From this it can be seen that J_c is uniform along the facets. In figure 6.8 (d), the cross-sections of the half-vortices along the zigzag junction is presented with the cross-sectional paths shown in Fig. 6.8 (c).

This experiment is the first direct observation of coupling of spontaneously generated half-integer magnetic-flux quanta. Later on in this section, experiments on the other samples will be presented, where the coupling of spontaneously generated half-integer magnetic-flux quanta is studied in more details.

In Section 6.1.3, the solution of the sine-Gordon equation for a zigzag junction with 10 facets of 40 μm width has been presented, and schematically depicted in Fig. 6.5. For this, the sine-Gordon equation has been solved for Josephson penetration depth of 64 μm, and further as the sample is cooled down, the Josephson penetration depth is decreased to 32, 16, 8, 4, and 2 μm. In this case, the spontaneous vortices always end up in a perfect antiferromagnetic arrangement because no

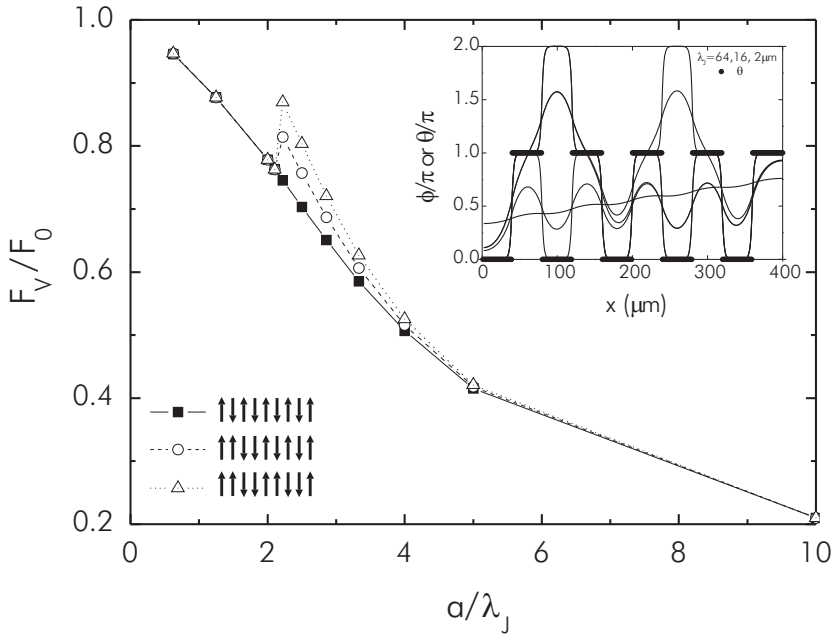

Figure 6.9: (a) The solution for the phase and (b) the relative free energy for a zigzag junction with various initial states (shown with small arrows in the legends). The Josephson penetration depth is decreased as the sample is cooled-down. The state with a perfect antiferromagnetic arrangement is always favorable than with a defect.

perturbation in its initial condition is introduced. But if the calculation is started with an initial defect, for instance with two positive and two negative half-vortices next to each other, a meta stable solution is found. This solution was also obtained numerically using the sine-Gordon equation solver developed by Kirtley *et al.* [121]. The phase difference distribution for various initial states is presented in Fig. 6.9 (a) for $\lambda_J = 64, 16$, and 2 μm. The solution for a system with a perfect antiferromagnetic arrangement of the $\uparrow\downarrow\uparrow\downarrow\uparrow\downarrow\uparrow\downarrow$ arrangement in its initial state is shown with a solid line, and with a defect in its initial state having the $\uparrow\uparrow\downarrow\downarrow\uparrow\downarrow\uparrow\downarrow$ and $\uparrow\uparrow\downarrow\downarrow\uparrow\uparrow\downarrow\downarrow$ arrangements are presented with a dashed and dotted line, respectively. The relative free energy for different initial states as mentioned above is depicted in Fig. 6.9 (b) as a function of the ratio between the facet length and Josephson penetration depth. It shows that it costs the system more energy in the intermediate limit ($a \sim \lambda_J$) to have a state which deviates from a perfect antiferromagnetic one, and that when $a \ll \lambda_J$ or $a \gg \lambda_J$ it has no significant difference in the energy cost for the system to have a state with or without a perfect antiferromagnetic one. It is noted here that the calculation only includes the current term, but not the field coupling. It can be therefore explained that during the cooling down process, the Josephson penetration depth goes from being very long, in which case it does not matter whether there are defects or not, to being very short, where again defects do not matter, through an intermediate range where defects cost lots of energy. At those temperatures the antiferromagnetic ordering sets in and freezes in because the barrier energy, the energy to flip the polarity of the spontaneous vortices, is much larger than $k_B T$.

To estimate the energy needed to flip the polarity of the spontaneous flux in zigzag junctions, the solutions for the free energy of 0-π junctions described in Eq. 6.12 have been calculated numerically using the sine-Gordon equation solver developed

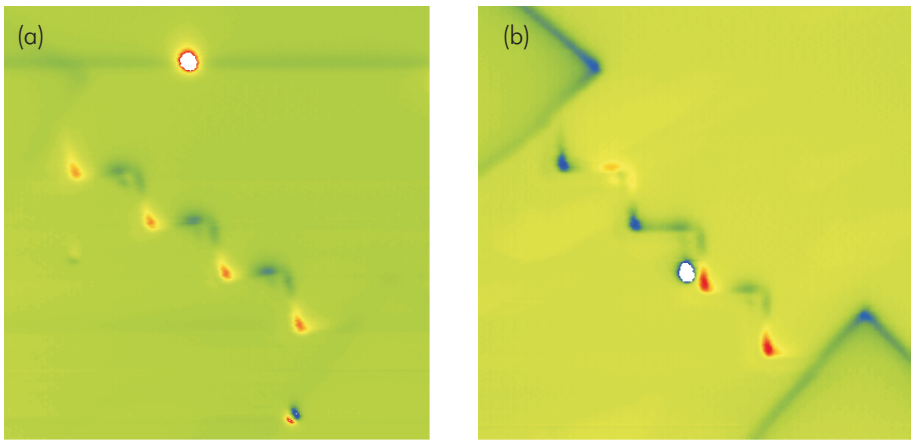

Figure 6.10: [color] (a) Half-vortices in a zigzag junction with 8 facets of 25 μm width. An Abrikosov vortex was found trapped far enough from the corners leaving the vortices in a nice antiferromagnetic ordering. (b) The antiferromagnetic ordering was distorted by an Abrikosov Vortex trapped near one of the corners.

by Kirtley *et al.* [121], applying a method as described in Ref. [119]. The results show that the free energy per facet, when the junction is in perfect antiferromagnetic ordering, is $\approx -5 \times 10^6$ K/$\lambda_J(\mu\text{m})$. The energy cost to form a defect, by flipping one spin, is $\approx 7.2 \times 10^5 \exp[-45/\lambda_J(\mu\text{m})]$. This implies that when the free energy per facet is comparable to k_BT, the energy cost to form a defect is $\approx 7.2 \times 10^5$ K: it is extremely energetically favorable to form perfect antiferromagnetic ordering in zigzag junctions.

Remark that although the antiferromagnetic ordering was very robust for different cool-downs and for different samples with a comparable geometry, deviations from antiferromagnetic arrangement were also observed when a magnetic field was applied during cool-down, or when Abrikosov vortices were found trapped in (or near) the junction interface. Figure 6.10 shows arrangement of spontaneously generated vortices in a zigzag junction with 8 facets of 25 μm width and with an Abrikosov vortex trapped in the Nb or $YBa_2Cu_3O_{7-\delta}$ electrode. In Fig. 6.10 (a), an Abrikosov vortex was found trapped at quite a distance from the half-vortex arrays leaving them in a nice antiferromagnetic arrangement, while in Fig. 6.10 the antiferromagnetic ordering was distorted by an Abrikosov vortex trapped near one of the corners.

6.2.3 Half magnetic-flux quanta in background fields

In a nominal zero field, the half-vortices in a zigzag junction interact strongly with one another to form an antiferromagnetic arrangement. To study the ordering of these half-vortices in the presence of applied fields, the sample was cooled down in various background fields [121]. A nominal cooling rate of 1 mK/sec through T_c was used. A low frequency oscillation of a few tens of milliKelvin in temperature was observed during cool-downs.

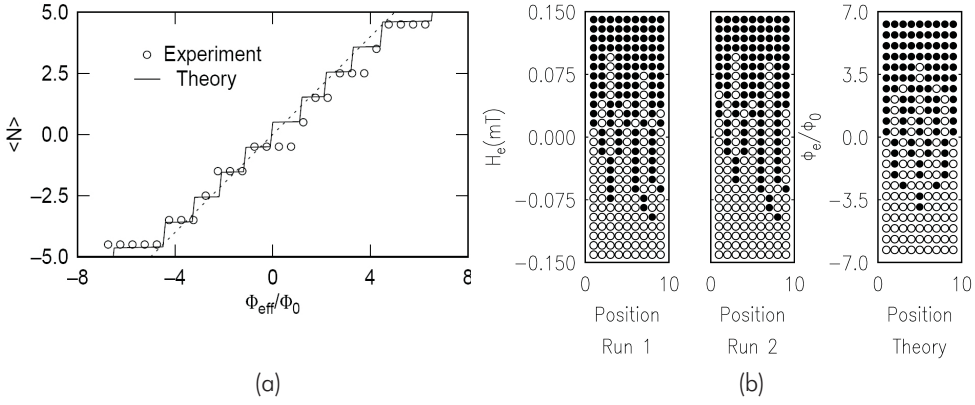

Figure 6.11: (a) The total flux in a zigzag junction with 10 facets of 40 μm width as a function of effective flux through the junction. (b) Visualization of the arrangement of the half-vortices in the same zigzag junction.

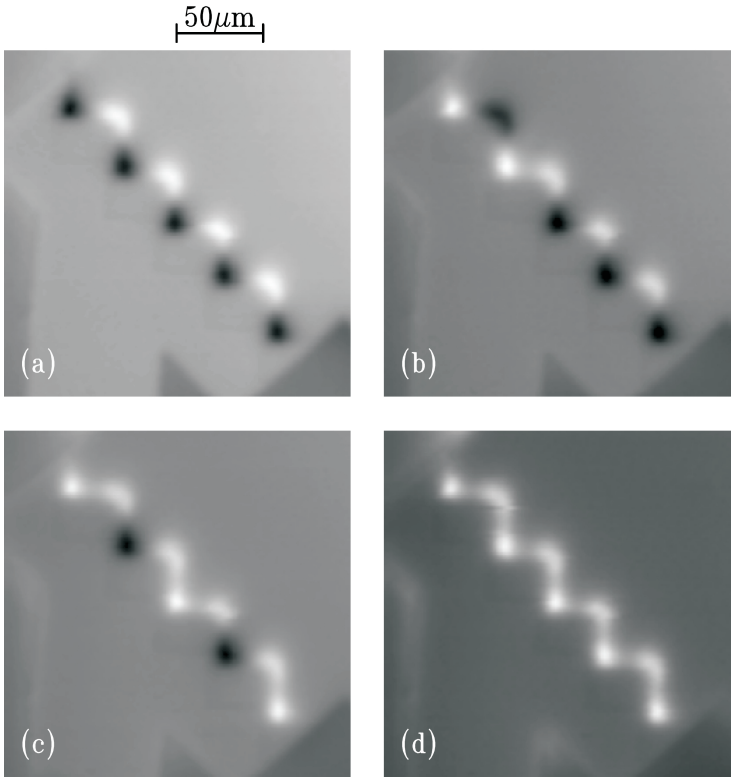

Figure 6.12: Scanning SQUID microscope images of zigzag junctions with 10 facets of 40 μm, cooled in fields of (a) 0 nT, (b) 32 nT, (c) 74 nT, and (d) 110 nT, and imaged at 4.2 K.

Figure 6.11 (a) plots the total flux in a zigzag junction with 10 facets of 40 μm width as a function of the effective flux through the junction, for a number of different cool-downs. The experimental results are described by the open circles and the theory by the solid line. The arrangement of the vortices is visualized in Fig. 6.11 (b) with black circles representing positive vortices (pointing out of plane of the sample) and white ones negative vortices (pointing into the sample). The theory was obtained by solving the sine-Gordon equation using a procedure in Ref. [20, 119] by increasing the total effective applied fields in a $0.25\Phi_0$ step. The cooling of the sample was simulated by gradually shortening the Josephson penetration depth. The vertical axis is the effective flux upon cooling. At high positive fields all the half-vortices point out of the plane, and at high negative fluxes all of the half-vortices point into the plane. Close to zero field the vortices take on an antiferromagnetic arrangement. Figure 6.12 shows some examples of the flux arrangement when zigzag junctions are cooled in externally applied magnetic field.

There are some disorder effects in the cooling process, as evidenced by the slight

differences between two experimental runs as depicted in Fig. 6.11 (b). The simulation results qualitatively present a similar but more symmetric arrangement than the experiment with respect to inversion in position, or with respect to field reversal.

Nevertheless, the amount of intermediate states between the completely antiferromagnetic and completely ferromagnetic ordering coincides pretty well. One possible source of the observed asymmetry might be field gradients. However, putting a linear field gradient into the model did not improve the fit with experiment [20]. Another source of asymmetry may be due to the coalescence of domains with short range ordering. Once this ordering has set in, it costs quite some energy to change it. The asymmetry of the junction and lead geometry might also lead to this asymmetry. The qualitative agreement between theory and experiments supports that the antiferromagnetic coupling of the half-integer flux-quanta is through the phase at the superconducting state and that the antiferromagnetic order is the ground state of the system.

6.2.4 Coupling of half magnetic-flux quanta in connected versus unconnected structures

In the zigzag configurations as described previously, all the half-vortices were generated in a singly connected superconducting structure; the question therefore arises as to whether the antiferromagnetic ordering is purely due to an interaction via the superconducting connection between the vortex-generating corners or also to a magnetic interaction between the fractional vortices. To investigate this, an array of corner junctions with a similar configuration as the zigzag junction but with 2.5-μm-wide slits etched halfway between the π-rings has been fabricated. In this situation there is no superconducting connection between the separate flux-generating corners, leaving only the magnetic dipole-dipole coupling as the dominant interaction.

Figure 6.13 (a) and (b) shows optical photographs of a connected and unconnected zigzag structure, respectively. Those structures were fabricated on the same chip and placed close to each other to warrant identical circumstances but far enough to prevent flux coupling between different zigzag junctions. In addition, the chip contained several reference junctions. At temperature $T = 4.2$ K, these reference junctions showed a typical critical current per micrometer junction width of $I_c/w \approx 0.1$ mA/μm. From this, a value for the Josephson penetration depth $\lambda_J \approx 1$ μm ($T = 4.2$ K) is deduced. The scanning SQUID microscopy images are shown in Fig. 6.13 (c) for a connected zigzag structure and (d) for an unconnected one. The images were made at a temperature of 4.2 K, with an octagonal pick-up loop of 4 μm in diameter. Both images were obtained at the same cool down, with the sample cooled and imaged in a magnetic induction < 0.5 μT.

In Fig. 6.13 (c), a spontaneously induced magnetic flux is clearly seen at every corner of the zigzag structure. For this junction the distance between the corners $a = 40$ μm, which implies that the facets are well within the wide limit. The figure shows that this section of the junction spontaneously generated 16 half-vortices which were arranged in an antiferromagnetic fashion. This antiferromagnetic ordering was very robust, occurring for different samples with comparable geometries as also having been shown in the previous sections.

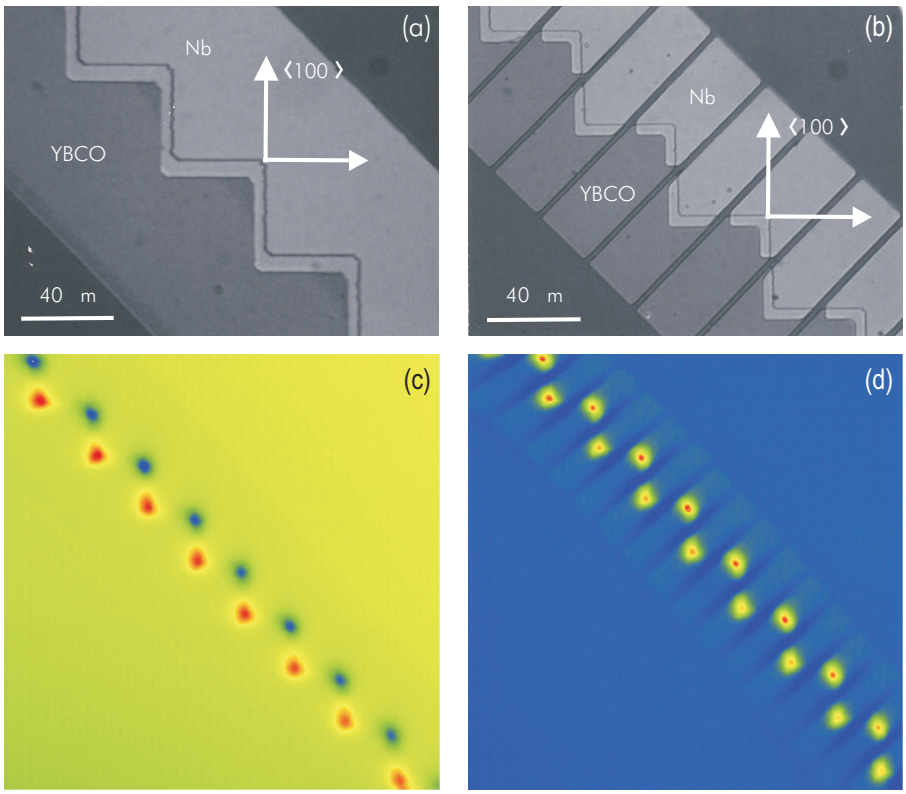

Figure 6.13: [Color] Generation of half-integer flux-quanta in connected and unconnected $YBa_2Cu_3O_{7-\delta}$-Au-Nb zigzag structure. The layouts of the zigzag structures are shown in (a) for connected and (b) for unconnected structures. The scanning SQUID micrographs of (c) 16 antiferromagnetically ordered half-vortices at the corners of a connected zigzag structure, and (d) 16 ferromagnetically ordered half-vortices at the corners of a unconnected zigzag structure.

It is noteworthy here that in this particular sample, the half-vortices are more symmetric between positive and negatives ones, as compared to the previous sample described in Section 6.2.2. For the half-vortices at the $YBa_2Cu_3O_{7-\delta}$ side, the fluxes were not spread out but much more localized. This is due to a shorter Nb overhang of $2-3$ μm as compared to the $5-6$ μm for the sample of Fig. 6.8. Figure 6.13 (d) shows a scanning SQUID image for an unconnected zigzag structure with a distance between the corners equals to the facet length in the connected array, $a = 40$ μm. In this case, a ferromagnetic arrangement of the fractional flux quanta was observed. The magnetic interaction between the half-integer flux-quanta at this distance is expected to be very weak, and alignment along minute spurious background fields in the scanning SQUID microscope is anticipated to be the dominating mechanism for their parallel arrangement.

When the distance was decreased to about 20 μm, with a slit width of 1.5 μm, a tendency towards an antiferromagnetic coupling was observed as shown in Fig. 6.14 (c). This image was made from the same chip which was cooled at the same time as the previous two images in Fig. 6.14 (a-b). The half-vortices now seem to have pretty random alignments. The random configuration can not be simply explained by, *e.g.*, a small background field, because all connected and unconnected zigzag junctions were cooled at the same time under the same conditions.

To further test the strength of the magnetic field coupling, two connected zigzag junctions were placed in parallel close together, but electrically disconnected from one another, as shown in Fig. 6.14 (d-f) connected junctions were also fabricated. Fig. 6.14 (d) shows a section of a 40 μm facet double junction that shows in-phase alignment between the two anti-ferromagnetically ordered 1D chains. Because this

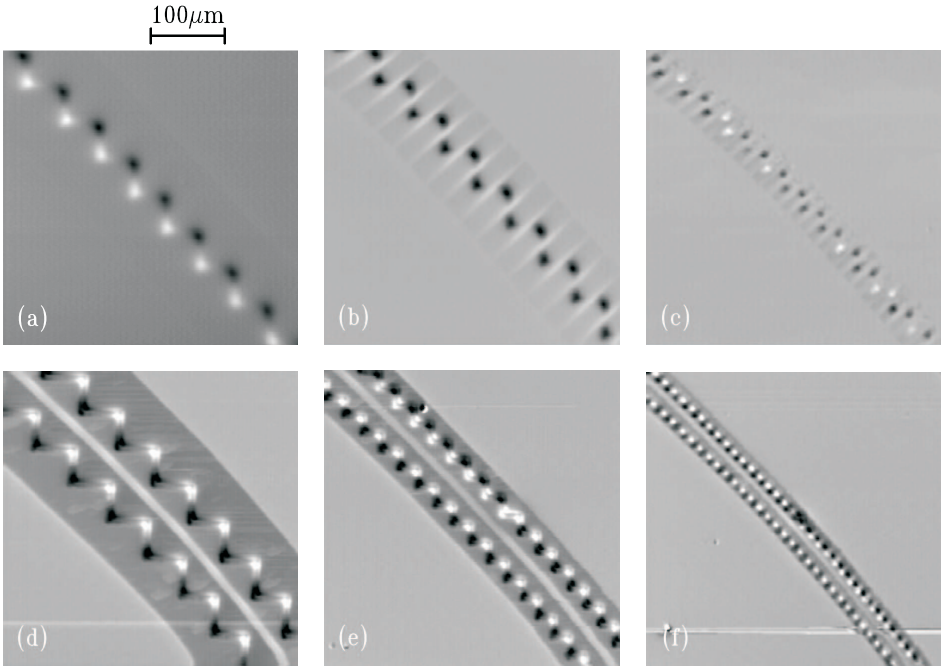

Figure 6.14: Scanning SQUID microscope images of zigzag junctions, cooled in nominally zero field, and imaged with a 4 μm diameter pickup loop. (a) Connected zigzag junction with 40 μm facet lengths. (b) Unconnected zigzag junction with 40 μm between facet corners. (c) Unconnected zigzag junction with 20 μm between facet corners. Two parallel zigzag junction with (d) 40 μm, (e) 20 μm, and (f) 10 μm between facet corners. The apparent curvature of the junctions in these images is an artifact of the scanning mechanism. A tendency towards an antiferromagnetic ordering was observed instead of a perfect ferromagnetic ordering for an unconnected zigzag junction with a shorter corner-to-corner distance of 20 μm.

arrangement places the positive half-fluxons in the lower left chain closest to the negative half-fluxons in the upper right chain, this is the lowest energy arrangement. However, in sections of the 1D chains which show defects, as in the center of the upper right chains in Fig. 6.14 (e) and (f), the interchain alignment goes from in-phase to out-of-phase when the interchain ordering has a defect, but one chain does not develop a second defect to align the interchain spins. Therefore it appears that the energy cost to create a defect is larger than the energy gain from making neighboring chains in-phase. It appeared that also in this case the phase coupling was stronger than the field coupling.

It can be concluded that antiferromagnetic coupling is also energetically favored in unconnected zigzag junctions, but not nearly as strong as in connected zigzag junctions. This was explored further in coupled two-dimensional arrays, which will be described in Chapter 7.

Flux calibration

To calibrate the flux in the zigzag samples, Kirtley [121] used a method as follows. The total flux through the SQUID pickup loop over a circle area is numerically integrated and appropriately normalized by drawing concentric circles in the data, centered on one of the Josephson vortices, as illustrated in Fig. 6.15 (b). To integrate the flux in the data, WinImage[1] software was used.

The integrated fluxes are then plotted as a function of the circle area. Since the circle area becomes larger and larger, the total-flux value oscillates between positive and negative limits, as the next positive or negative Josephson vortex is included in the circle area.

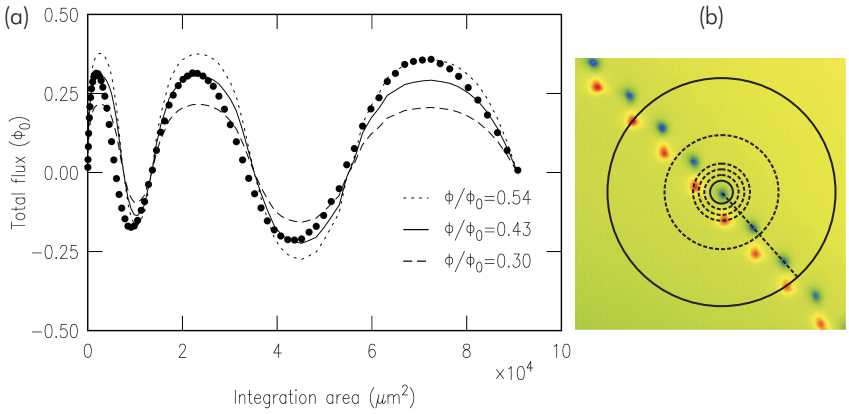

Figure 6.15: [Color] (a) Total flux in the junction as function of an increasing integration area as illustrated in (b). The total fluxes obtained from the experiment are represented by the black dots and those from theory with different fitting parameter by the solid lines. (b) Illustration of the integration area in the data.

The points in Fig. 6.15 (a) represent the data. The lines are fits with magnetic monopoles of alternating sign at the appropriate positions. The fitting parameters were the effective height z of the SQUID pickup loop above the sample surface, and the absolute value of the total flux in each Josephson vortex. The best fit was obtained for $z = 7$ μm, $\Phi = 0.43 + (0.11 - 0.13)\Phi_0$, using a doubling of the chi-square χ^2 as a measure of the uncertainty.

The peak heights in Fig. 6.13 (c) have a standard deviation of about 0.12 times the average peak heights. This means that the total flux in the Josephson vortices are uniform to at least that fractional value.

6.3 Concluding remarks

One-dimensional zigzag Josephson arrays are considered, in which the facet-length is noticeably larger than the Josephson penetration depth. In this case, the built-in π-phase shift in a zigzag Josephson array results in a phenomenon of spontaneous magnetization even in the absence of a bias current or an applied field.

In the limit of the facet-length being much larger than the Josephson penetration depth, the zigzag array has a doubly degenerate time-reversed ground state, which is characterized by a spontaneous generation of half magnetic-flux quanta at every corner, with a magnitude of $\frac{1}{2}\Phi_0$ ($\Phi_0 = h/2e = 2.07\times10^{-15}$ Wb). In this case, the self generated half-vortices can be regarded as an additional π-phase shift. The $I_c(H_a)$-dependence of the zigzag junction then effectively changes and becomes identical to those for a conventional junction in a large facet limit.

Using scanning SQUID microscopy, the spontaneous vortices in the zigzag junction have been observed and studied. The coupling of the half-integer flux-quanta was compared between connected and unconnected zigzag junctions. It was found that antiferromagnetic coupling is energetically favored in both connected and unconnected zigzag junctions. The spontaneous vortex images of the connected and unconnected junctions, which were cooled under the same conditions, show that the antiferromagnetic coupling in the unconnected zigzag junction is not as strong as in the connected zigzag junction.

Based on these results, Goldobin *et al.* [122] theoretically proposed that the ordering fashion of spontaneously generated half-integer magnetic-flux quanta in connected $0-\pi$-zigzag-structures could be controllably altered by applying a current bias. The initial antiferromagnetic ordering can than be totally modified, and becomes *e.g.*, a piece-wise ferromagnetic ordering. Simply put, in this case, the negative and positive half-integer flux quanta have been separated from each other under the influence of the Lorentz force, acting in different directions for a given direction of the biased-current. Thus from the initial state $\uparrow\downarrow\uparrow\downarrow\uparrow\downarrow\uparrow\downarrow$ it is proposed that one could arrive via *e.g.*, an intermediate state $\uparrow\uparrow\downarrow\downarrow\uparrow\uparrow\downarrow\downarrow$ to the completely separated case $\uparrow\uparrow\uparrow\uparrow\downarrow\downarrow\downarrow\downarrow$. The experimental tests for this theoretical proposal seem to be easily accessible using the low-T_c/high-T_c-junction-technology described in this thesis.

[1] WinImage software was written by Dr. J. R. Kirtley at IBM.

Chapter 7

Ordering and manipulation of half flux-quanta in 2-d π-ring arrays

For unconnected corner junctions at sufficiently close distances, the half flux quanta are becoming antiferromagnetically arranged owing to magnetic interaction. To further explore this, two-dimensional π-ring arrays have been realized in various configurations. The results of the experiments on these two-dimensional Josephson arrays will be discussed in this chapter. The first configuration for which the generation and coupling of half-integer flux quanta were investigated, was the triangular array. This geometry is of particular interest, as with the preferential antiferromagnetic coupling between the half-integer flux quanta, it provides a model example of a strongly frustrated system, characterized by a highly degenerate ground state.

Investigations of spin interactions on the unfrustrated geometries are a common way in which the Néel long range ordering of a spin system can be investigated. Therefore, coupling of the half flux-quanta was also investigated and compared between frustrated and unfrustrated geometries. Scanning SQUID microscopy has been used to study the ordering of half flux quanta in these structures. The possibility of manipulating the polarities of individual half flux quanta is also demonstrated.

7.1 Introduction

7.1.1 The superconducting π-ring as an Ising spin

In Chapter 6, it has been shown that a superconducting ring with a built-in π-phase shift has a doubly degenerate time-reversed ground state, which is characterized by the spontaneous generation of half magnetic-flux quanta of $\pm\frac{1}{2}\Phi_0$ ($\Phi_0 = h/2e = 2.07\times10^{-15}$ Wb). In Fig. 7.1, this doubly degenerate ground state is represented by a plot of the π-ring free energy as a function of the flux in the ring. The spontaneous flux in the ring can basically take either the downward or upward direction, corresponding

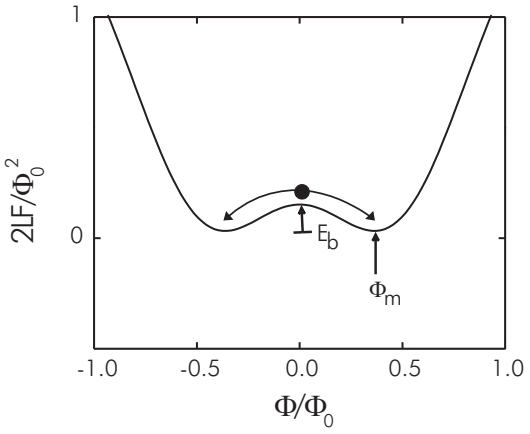

Figure 7.1: Doubly degenerate ground states of π-rings with a spontaneous generation of magnetic flux $\pm\Phi_m$. E_b is the barrier energy between the two states.

to the clockwise or anticlockwise circulating supercurrent, respectively. With this, it is possible to think of a π-ring as an Ising system [123]. In general, the Ising spin can be described by a variable σ, which can take only two values: ± 1.

The energy barrier between the positive spontaneous flux (spin up) and negative flux (spin down) ground states of a π-ring can be derived from the free energy of such systems. The free energy F of a superconducting π-ring of inductance L interrupted by a Josephson junction with a critical current I_c is described by Eq. 6.2. In the limit $1 - t \ll 1$ ($t = \frac{T}{T_c}$) and $\Phi_a = 0$, the spontaneous flux Φ_m can be obtained by minimizing F with respect to Φ. This yields

$$\frac{\Phi_m}{\Phi_0} = \sqrt{\frac{3}{2\pi^2}\left(1 - \frac{1}{\beta}\right)} \tag{7.1}$$

where $\beta = 2\pi L I_c/\Phi_0$. The barrier energy E_b to flip the sign of the rings' circulating supercurrent is then

$$E_b = F(\Phi = 0) - F(\Phi = \Phi_m) \tag{7.2}$$

and this leads to

$$E_b = \frac{3 I_c \Phi_0}{4\pi}\left(1 - \frac{1}{\beta}\right)^2 \tag{7.3}$$

The energy barrier is temperature dependent (because of the temperature dependence of I_c), the lower the temperature the higher the barrier.

The spontaneous generation of a half magnetic flux quantum in a single π-ring has been used in various phase sensitive pairing symmetry tests to provide an unambiguous signature for $d_{x^2-y^2}$-wave order parameter symmetry in high-T_c copper oxide superconductors [26], and as a potentially practical application of $d_{x^2-y^2}$ superconductivity [50]. These experiments were mainly conducted by using grain boundaries in

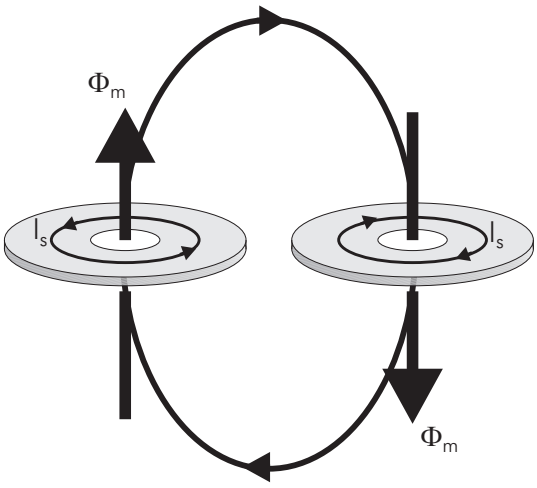

Figure 7.2: Two isolated π-rings are placed in close proximity. Antiparallel alignment of the spontaneous fluxes is favorable between the two rings.

high-T_c superconductors, induced by the epitaxial deposition on tri- or tetracrystalline substrates [26, 50]. However, this technique does not lend itself to the construction of coupled π-ring arrays, especially in a large number. Using thin-film ramp-type $YBa_2Cu_3O_{7-\delta}$/Au/Nb Josephson contacts, on the contrary, it has been possible to realize coupled π-ring arrays [17, 19, 21, 22], as presented in Chapter 6. The freedom in fabricating π-rings in a large number and in various geometries results from the standard optical photolithography technique that is used.

Linear arrays of π-rings have been presented in Chapter 6, which includes both connected and unconnected arrays. In unconnected linear π-ring arrays at sufficiently close distance, the half flux quanta are becoming antiferromagnetically coupled owing to magnetic interaction. The antiferromagnetic flux-coupling between two superconducting π-rings, in the presence of a spontaneous magnetization in the rings, can be understood by considering two of such rings, which are electrically isolated and placed in close proximity in zero applied field as illustrated in Fig. 7.2. Suppose that both isolated π-rings spontaneously generate half magnetic-flux quanta of $\frac{1}{2}\Phi_0$ in their ground state, and that the spontaneous flux in the left ring is pointing upwards. The flux from the left ring will close its loop through the second ring because of the dipolar nature of the magnetic field. The induced field from the left ring is then pointing down in the right ring. The spontaneous flux in the right ring basically has a possibility to choose either directions. If an upward direction is chosen, then the spontaneous flux in the right ring must be larger than $\frac{1}{2}\Phi_0$ in order to compensate the induced field from the left ring and simultaneously to comply with the condition that the flux in the ring must be equal to $\frac{1}{2}\Phi_0$. On the other hand, if it is pointing down then the spontaneous flux is less than $\frac{1}{2}\Phi_0$, because the half magnetic-flux quanta condition is accomplished by the induced field from the left ring. The latter situation is favorable

for the π-ring since it costs the system less energy. Thus the spontaneous flux in the right ring is effectively biased into a spin down state by the induced flux from the left ring. The flux from the right ring then also closes its loop through the left ring, favoring its spin up state. There is thus a net antiferromagnetic interaction between rings.

The dynamics of flux-coupled superconducting π-rings are determined by the coupling energy between the spontaneous flux of the rings E_c and the energy barrier between the rings' spin-up ($+\Phi_m$) and spin-down ($-\Phi_m$) states E_b. If the left and right ring in Fig. 7.2 are labeled by i and j, respectively, the coupling energy E_c between the rings can be written as

$$E_c = M_{ij}|I_i||I_j|\sigma_i\sigma_j \tag{7.4}$$

where M_{ij} is the mutual inductance between the two rings, $|I_i|$, $|I_j|$ are the amplitudes of the circulating supercurrents in the rings, and $\sigma_i = \pm 1$ are the Ising variables assigned to ring i, indexing the directions of the flux. If the circulating currents in both rings are the same, then

$$E_c = M_{ij}I_i^2\sigma_i\sigma_j \tag{7.5}$$

From the spontaneous flux of Eq. 7.1 and in the limit $1 - t \ll 1$, the circulating supercurrent in the rings is

$$I_i = \frac{\Phi_m}{L} = \frac{\Phi_0}{L}\sqrt{\frac{3}{2\pi^2}\left(1 - \frac{1}{\beta}\right)} \tag{7.6}$$

and the coupling energy between the rings is approximated by

$$E_c = \frac{M_{ij}\Phi_m^2}{L^2}\sigma_i\sigma_j \tag{7.7}$$

The coupling energy between the rings is proportional to their mutual inductance, and it grows as $E_c \sim (1 - T/T_c)^2$. The effect that opposes the coupling between the spontaneous fluxes is the increase of the barrier energy. As the rings cool below T_c, the supercurrent densities grow until two distinct circulating states become allowed for $\beta > 1$.

When the system is cooled in zero applied field, then at temperatures important in the cooling process, close to the transition temperature T_c of Nb, the energy barrier between spin up and spin down states is very small. Then the transitions between the two states can occur spontaneously in both rings. Thermally activated switching between spin up and spin down states has a transition rate [20, 124]

$$r \approx \frac{\beta_c}{2\pi\tau}e^{-E_b/k_BT} \tag{7.8}$$

where $\beta_c = 2\pi I_c R^2 C/\Phi_0$ is the junction hysteresis parameter, and $\tau \equiv \Phi_0/2\pi I_c R$ is the junction characteristic time.

Both E_b and E_c increase rapidly with decreasing temperature, and the increase of the barrier energy leads to slower flipping rates until the flipping stops when $E_b/k_BT_f \approx 1$, where T_f is the freezing temperature of the flipping.

7.1.2 Two dimensional antiferromagnetic Ising spins

Arranging π-rings on a lattice with an antiferromagnetic interaction between the rings' spontaneous flux, two-dimensional Ising antiferromagnet models can be realized. Until now, such systems have been studied with, for example, arrays of all-low-T_c superconducting rings biased at an external magnetic flux of $1/2\Phi_0$ per ring [125–128], and with low-T_c Josephson junction arrays [129]. Fluctuations in the dimensions of those rings, resulting in variations in the flux bias and a lifting of the degeneracy, have been found to be a major complication in these investigations [126–128]. The spontaneously generated flux in the $YBa_2Cu_3O_{7-\delta}$-Au-Nb structures provides an advantage

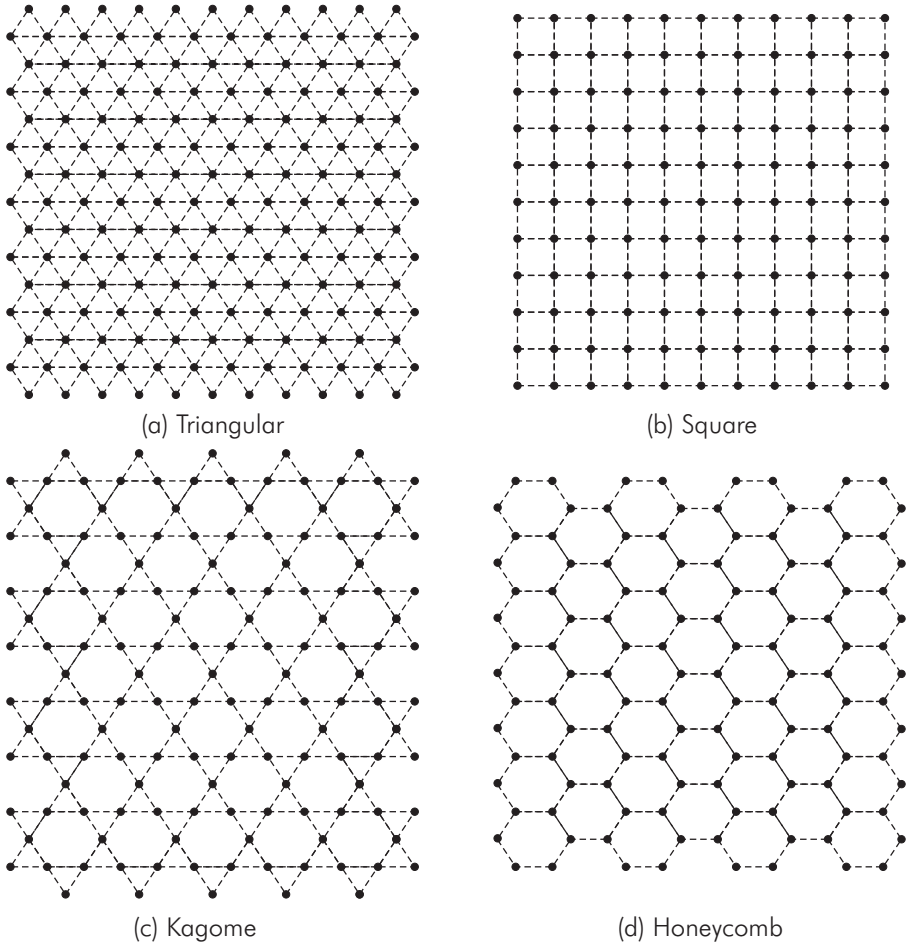

Figure 7.3: Geometries of (a) triangular, (b) square, (c) kagomé, and (d) honeycomb lattices. The black dots represent the half-flux quantum sites. The dashed lines are drawn only for clarity.

in this respect, as the two flux states in these elements are intrinsically degenerate.

In arrays of conventional rings, since the experiments have to be done in a large applied field [127], the long range antiferromagnetic coupling is destroyed by variations in ring size, which act as random additional fields. This should not be the case for arrays of π-rings, where the interesting field region is as close to zero as feasible. In this respect, π-rings biased at close to zero field present a fundamental advantage over conventional rings biased close to $\frac{1}{2}\Phi_0$ per ring.

Various two-dimensional arrays of π-rings have been constructed. The four basic lattices were the triangular, square, honeycomb, and kagomé lattices, shown schematically in Fig. 7.3.

Frustrated systems

The first configuration for which the generation and coupling of half-integer flux quanta were investigated, was the triangular array. This geometry is of particular interest, as with the preferential antiferromagnetic coupling between the half-integer flux quanta, it provides a model example of a strongly frustrated system, characterized by a highly degenerate ground state [130]. Frustration arising from the lattice geometry is called geometrical frustration. An example of geometrical frustration is schematically shown in Fig. 7.4 for a triangular geometry. The isotropic antiferromagnetic coupling between the spins, $E_{c1,2} = E_{c2,3} = E_{c3,1}$, leaves the third spin undetermined, while the first and the second spins choose an antiparallel arrangement. Therefore, there is a competition between the spins' interactions. Because of this competing interaction no configuration of Ising spins can minimize the energy of all interactions simultaneously. Even in the ground state ($T = 0$) some interactions are broken, *i.e.*, remain in the energetically unfavorable configuration. The frustrated triangular and kagomé lattices are sketched in Fig. 7.3 (a) and (c), respectively. In the case of a kagomé lattice there exists two kinds of polygons: triangles and hexagons. Because of the geometrical frustration in the triangles, there is no way to minimize

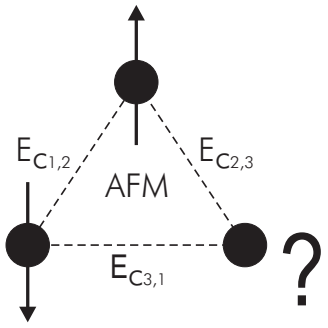

Figure 7.4: Frustration in a triangular geometry with an isotropic antiferomagnetic (AFM) coupling between the spins.

the energy in a unique way in such lattices [131]. The number of energetic ground states diverges with system size [132]. As a result, the ground state is highly degenerate even at $T = 0$ [131], and there is no long range ordering. Even though there can be no long order for the Ising model in this lattice, short range correlations are still possible. In this case, the correlations are limited only to *e.g.*, nearest or next-nearest neighboring spins.

Unfrustrated systems

The natural way to investigate the existence of Néel long range order in two dimensional Ising systems is to put the spins onto lattices of an unfrustrated geometry. The unfrustrated square and honeycomb lattices are sketched in Fig. 7.3 (b) and (d), respectively. These unfrustrated lattices basically can be separated into two sublattices (bipartite), satisfying the condition that all the nearest neighbors of the first lattice belong to the second lattice (Fig. 7.5). This is the ground state of the bipartite lattice, which exhibits a long range ordering. In this ground state, all the vortices in the first sublattice point upward and those in the second sublattice downward.

Low dimensional antiferromagnets are an area of much current interest in the field of magnetism, and there are important unanswered questions about the effects of lattice geometry and competing interactions on the ordering and dynamical properties of such systems [131]. Making the spin systems lithographically leaves one considerable freedom to tailor their properties, and to realize two-dimensional spin systems in many different configurations. This is in contrary to conventional three-dimensional magnetic materials, in which chemical structures place strong constraints on the sys-

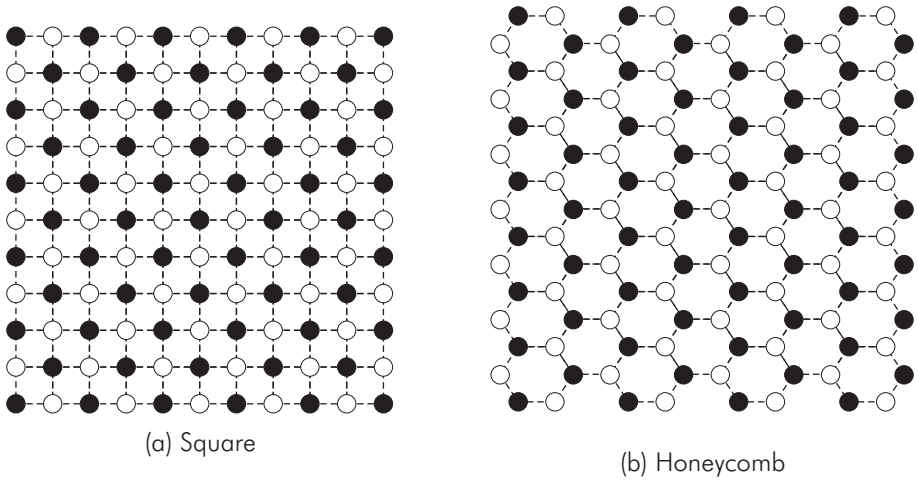

Figure 7.5: The groundstate of two-dimensional (a) square and (b) honeycomb Ising spins with a nearest neighbor antiferromagnetic interaction. Black dots represent spins pointing upward, and white dots downward. This ordered state is known as the Néel state.

tems available for study. More interestingly, spontaneously generated half-integer flux quanta present an analogue to Ising-spins instead of to continuously rotatable spins, which make the investigation on the spin-systems relatively easier.

Furthermore, although the magnetic compound $SrCr_8Ga_4O_19$ with continuous magnetic moments residing primarily on Kagomé lattices has been recently discovered [133–135], no magnetic material with Ising-antiferromagnet spins residing on Kagomé lattices has been found yet. In addition no experimental evidence of the geometrical frustration on the Kagomé lattice is known [130]. In the following, experimental results using large arrays of photolithographically patterned π-rings as a model spin system will be presented.

7.2 Measurement results

Images of spontaneously-generated half-flux quanta in the two-dimensional π-ring lattices were taken by a high-resolution scanning SQUID microscope. The SQUID microscope images shown here were made by snap shooting the frozen spin configurations in the lattices at 4.2 K. The samples were cooled down through the Niobium T_c in nominal zero field with a typical cooling rate of 10 mK/sec. The induced field from the scanning SQUID microscope was estimated < 0.5 μT.

7.2.1 Magnetic imaging of triangular π-ring arrays

The first lattice samples were realized from two dimensional arrays of $0 - \pi$ corner-junctions in a triangular arrangement. Various arrays were fabricated on a single chip. The differences between the arrays on that chip were in the dimensions of, and

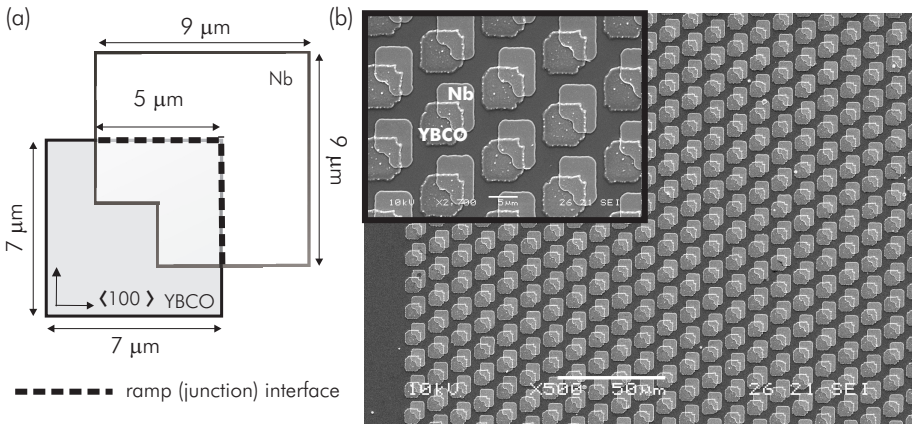

Figure 7.6: (a) Sketch of a 0-π junction used as the element for triangular arrays shown in (b) SEM micrograph of a triangular array of $0 - \pi$ junctions. In this case the facet size is 5 μm and the distance between the center of nearest neighboring rings is 12.5 μm.

the separation between the elements. The building blocks of the lattices are shown schematically in Fig. 7.6 (a). This element is a corner junction with a 5 μm facet length, and it is arranged on a lattice with a 12.5 μm separation between the center of nearest neighboring elements. Another array, which is built from 10 μm facet corner junctions, has a 25 μm separation between nearest neighboring elements.

As discussed in Chapter 6, the spontaneous flux in $0-\pi$-junctions is determined by the ratio between the facet-length and the Josephson penetration depth a/λ_J, while the Josephson penetration depth itself is inversely proportional to the square root of the critical current density. For a symmetric case, spontaneous flux is expected at any value of a/λ_J, but it approaches a half flux quantum when $a/\lambda_J = 4$. Set by a limitation in the maximum critical current density of $10^4 - 10^5$ A/cm^2 that can be achieved in current $YBa_2Cu_3O_{7-\delta}$/Nb ramp-type technology, the smallest $0-\pi$ junction is designed to comprise of facets with 5 μm width. Assuming a critical current density of 5×10^4 A/cm^2, a ratio of $a/\lambda_J \sim 4$ is obtained for the $5-\mu$m-wide and 150-nm-thick junction area. Figure 7.6 shows Scanning Electron Microscopy (SEM) images of a π-ring array built from 0-π junctions in a triangular arrangement. In this array, the facet size is 5 μm, and the separation between the rings is 12.5 μm. The thickness of $YBa_2Cu_3O_{7-\delta}$ and Nb layer are 150 nm and 160 nm, respectively. In total, the lattice has 16,000 π-rings of $0-\pi$ junctions.

Figure 7.7 depicts scanning SQUID micrographs of the arrangement of the fractional flux quanta in a section of a triangular array for two different cooling downs. In these images the brighter dots represent rings with supercurrents circulating clockwise and the darker dots counter-clockwise. In total, about 25,000 half flux quanta

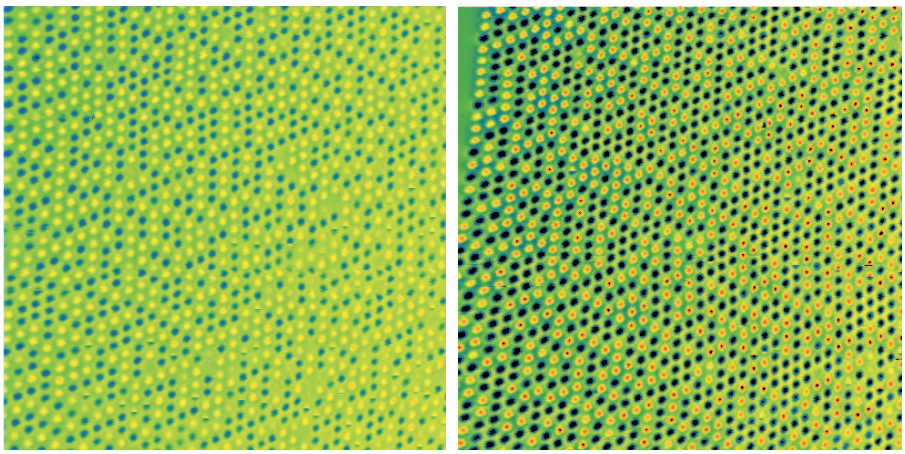

Figure 7.7: [Color] Scanning SQUID micrographs of the flux state in a section of a triangular lattice built from $0-\pi$ junctions at 4.2 K for two different cool downs (a) and (b), respectively. Each dot represents a half-vortex, generated by a $0-\pi$ junction with a facet length of 5 μm shown in Fig. 7.6.

were observed on a single chip, of size 5 mm×10 mm.

To estimate the freezing temperature of the spin configuration, the energy formulations described earlier in this chapter are used. Consider the condition at the temperatures important in the cooling process, *i.e.*, close to the Nb superconducting transition temperature T_c. The temperature dependence of the critical current at $1 - t \ll 1$ ($t = T/T_c$) can be approximated as

$$I_c(t) \sim I_c(0)(1 - t) \tag{7.9}$$

For 5 μm facet length rings the self-inductance is estimated $\sim$ 16 pH, and the mutual inductance between rings spaced by 12.5 μm is $\sim$ 0.2 pH. The freezing of the individual rings occurs when $\frac{E_b}{k_B T_f} \approx 1$, where T_f is the freezing temperature. From Eq. 7.9 and assuming that $I_c(0) = 0.5$ mA and T_c of Nb is 9 K, the freezing for the 5 μm facet rings was estimated to occur at $1 - t_f = 2.2 \times 10^{-2}$ ($t_f = T_F/T_c$). At this temperature $E_c/k_B T_f = 0.64$. For comparison, the barrier and coupling energy for these rings at the freezing temperature were estimated in the order of 18 K and 1.5 K, respectively. The increase of the barrier energy grows much more rapidly than the increase of the ring interactions.

Despite the random appearance of the spin configurations in the triangular lattices presented in Fig. 7.7, some broken (long-range) correlations can be clearly seen. A question to be addressed is then whether the apparently random configurations were due to the geometrical frustration effects or to the dynamic (quenched) disorders. To analyze this, the short-range correlation of the spin configurations is used and will be discussed in the following.

Short-range correlation of the spin configurations

The predominant interactions in two-dimensional spin arrays occurs between nearest-neighboring spins. A measure of such short-range correlations is the bond order parameter σ [127, 136]. This quantity is defined as

$$\sigma = 1 - \frac{x_{\mathrm{AFM}}}{2 x_\uparrow x_\downarrow} \tag{7.10}$$

where x_{AFM} is the fraction of antiferromagnetic near-neighboring bonds, which are bonds between a half-flux quanta pointing upwards and its nearest neighbors pointing downwards, and $x_\uparrow (x_\downarrow)$ are the fractions of half-integer flux quanta pointing upwards (downwards), respectively. For a completely random spin configuration, the antiferromagnetic bond fraction is equal to $2x_\uparrow x_\downarrow$. This would mean that, *e.g.*, for an equal number of up and down spins in a lattice, the fraction of antiferromagnetic bonds is 50% of the total bond. From this, the bond order parameter for a completely random spin distribution is $\sigma = 0$. An excess of ferromagnetic bonds over the random case results in $\sigma > 0$, and of antiferromagnetic bonds $\sigma < 0$. A completely correlated antiferromagnet would give a bond order σ of -1.

Figure 7.8 plots the theoretical σ-values as a function of the fraction of up-spins. For unfrustrated lattices the theoretical best-value is represented by the solid lines and for frustrated lattices by the dashed lines. The most-negative possible value of σ for the unfrustrated lattice ranges from $\sigma = 0$ when $x_\uparrow = 0$ or 1 to $\sigma = -1$ when

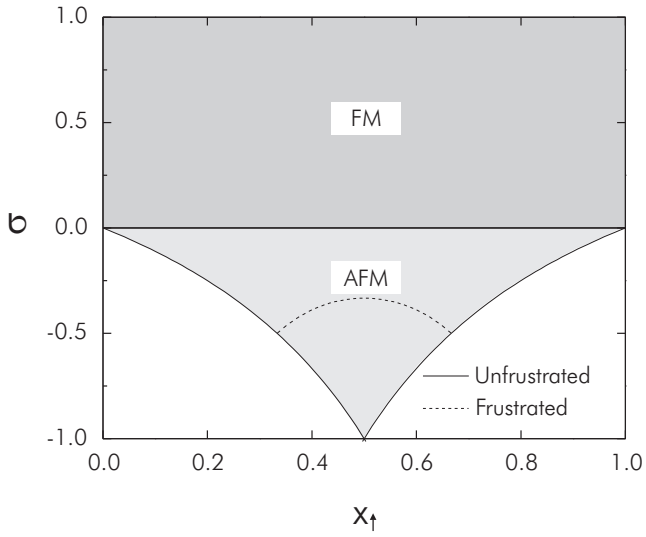

Figure 7.8: Bond order parameter σ describing the short range correlation between spins as a function of concentration of up spins. $\sigma > 0$ indicates ferromagnetic (FM) correlations, and $\sigma < 0$ antiferromagnetic (AFM) correlations. Unfrustrated nearest neighbor antiferromagnetic systems are bound by the solid line, and frustrated systems by the dashed line.

$x_\uparrow = 0.5$. This is due to the fact that for $x_\uparrow \leq 0.5$ the most antiferromagnetic possible case in the unfrustrated lattices is when each up spin is surrounded by down spins. Thus, the best antiferromagnetic-bond fraction $x_{\uparrow,\mathrm{best}}$ is equal to $2x_\uparrow$. The best σ for an unfrustrated lattice for a given spin-up fraction is therefore given by

$$\sigma_{\mathrm{best}} = \frac{x_\uparrow}{x_\uparrow - 1} \tag{7.11}$$

This bound in σ values is represented by the solid lines in Fig. 7.8.

For frustrated lattices, geometrical constraints do not allow up spins to avoid each other when $1/3 < x_\uparrow < 2/3$, *i.e.*, it becomes impossible to place up spins such that there is no parallel alignment between nearest-neighboring spins in the lattices. In this case, the best sigma is obtained by keeping the fraction of antiferromagnetic constant and equal to that for the best sigma of $x_\uparrow = 1/3$ or $2/3$. Therefore, the best sigma value for the frustrated lattice has a hump when $1/3 < x_\uparrow < 2/3$. This can be described by

$$\sigma_{\mathrm{best}} = \frac{x_\uparrow^2 - x_\uparrow + \frac{1}{3}}{x_\uparrow^2 - x_\uparrow} \tag{7.12}$$

and is shown by the dashed hump-line in Fig. 7.8. In this range, the difference in σ between frustrated and unfrustrated lattices becomes prominent.

For the half-flux quantum image in Fig. 7.7 (a), there are 718 up half-vortices, 727 down half-vortices, 2246 antiferromagnetic (AFM) bonds, 1847 ferromagnetic (FM)

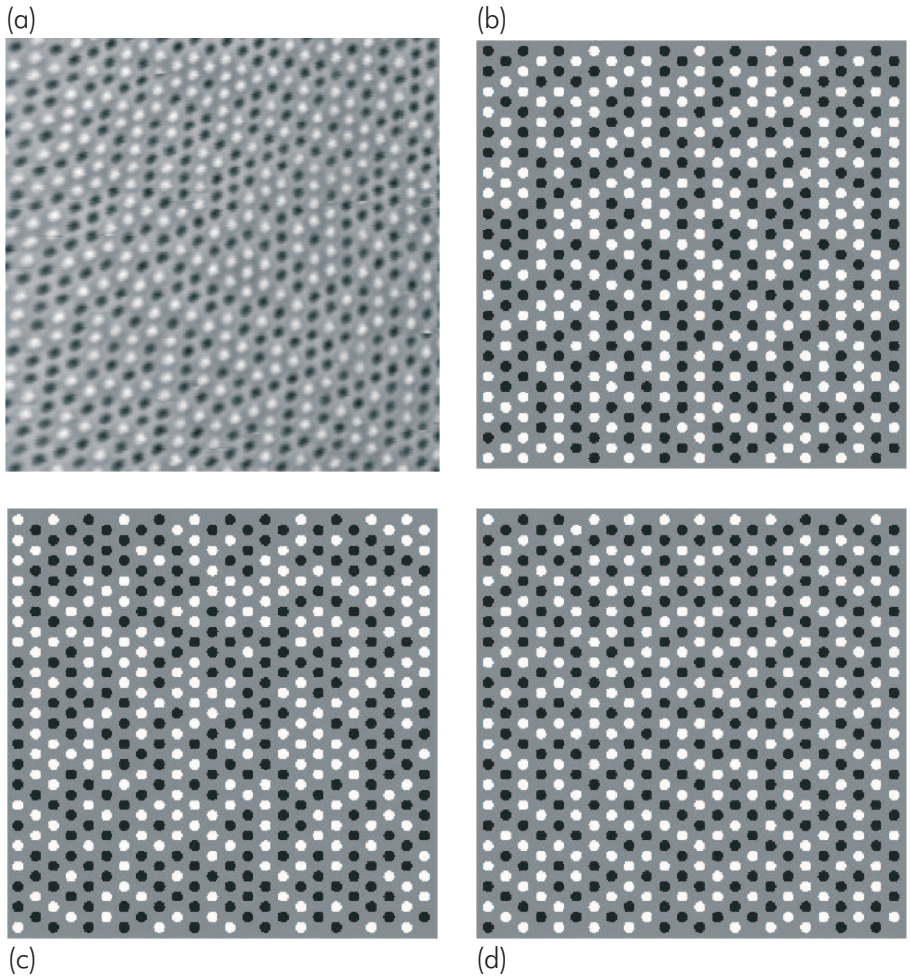

Figure 7.9: (a) Scanning SQUID microscopy image of a triangular array of $0-\pi$ junctions with a facet length of 5 μm and spins spacing of 12 μm, cooled and imaged in zero field. (b) Results of a Monte-Carlo simulation of the cooling process, with the same bond order $\sigma = -0.12$ as (a). (c) An array with randomly assigned spins, with equal probabilities of spin up and spin down. (d) Simulation resulting in nearly the minimum possible bond order at $x_\uparrow = x_\downarrow = 0.5$ of $\sigma = -0.32$.

bonds, giving a bond order of $\sigma = -0.0975$. A similar analysis on Fig. 7.7 (b) shows a bond order of $\sigma = -0.1037$, with a half-vortex up ratio of $x_\uparrow = 0.444$. The theoretical best bond order at $x_\uparrow = x_\downarrow = 0.5$ for a frustrated lattice, like the triangular lattice, is about -0.34. Experiments on the larger facet arrays showed much smaller AFM correlations. The above obtained numbers (about -0.1) are comparable to the results of [127] for a triangular array of 0-rings biased at $\sim \frac{1}{2}\Phi_0$ per ring by an external

magnetic field. However, one should realize that the experiments in [127] were done with rings about 5 times smaller, and more closely spaced, than the smallest rings employed in the 0-π corner junctions. Nevertheless, antiferromagnetic correlations can be seen in π-ring arrays.

To explain the difference between the best theoretical sigma value and the experiment value, Kirtley [121] developed a Metropolis Monte Carlo simulation to simulate the cooling process of the rings using the model outlined in the introduction section. Briefly, in these simulations a step is taken in temperature. The probability of a spin flip $P_i = (1 - T/T_c)^2 \exp^{-E_b/k_B T}$ is calculated for each ring [20]. A suitably normalized random number is generated. If this number is less than the spin flip probability, the spin of the ring is flipped. The process is repeated throughout the array, and iterated a number of times at each temperature. The cooling rate is decreased, and the number of iterations at each temperature is increased, until the results are independent of each.

Figure 7.9 (a) shows a scanning SQUID microscopy image of a triangular array of π-rings, with facet length 5 μm, and nearest neighbor spacing 12.5 μm, cooled and imaged in zero field. In this image the white dots represent rings with supercurrents circulating clockwise; the black dots have counter-clockwise circulation. The image in Fig. 7.9 (a) corresponds to $\sigma = -0.12$. The anti-ferromagnetic correlation in Fig. 7.9 (a) is apparent in the small number and sizes of clusters of rings with the same sign. Figure 7.9 (b) is the result of a Metropolis Monte Carlo simulation of the cooling process, for a 30×30 element array. For Fig. 7.9 (b) the coupling energy E_c was scaled well with the estimated value mentioned in Section 7.2.1, which produces the same bond order σ as was observed experimentally. Figure 7.9 (a) and (b) show striking similarities in the size and number of small clusters and straight lines of rings with the same spin. For comparison, the image of Fig. 7.9 (c), which has randomly assigned spins, shows larger clusters. Figure 7.9 (d), which shows modeling with E_c scaled up from the estimates above by a factor of 2, resulting in $\sigma = -0.32$, nearly the minimum bond order possible, has almost no same-spin clusters. Note that the modeling provides a natural explanation for incomplete antiferromagnetic ordering in these arrays, with no need to invoke disorder effects. Since the π-rings are cooled in zero field, they should not be susceptible to disordering due to lithographic variations in the size of the rings, as has been suggested for arrays of 0-rings. Increasing the coupling energy between half magnetic-flux quanta is expected to increase the sigma value in this experiment. This can be invoked by increasing the circulating supercurrent in the rings and decreasing the ring separation. This experiment will be presented later in this chapter.

Manipulating the spontaneous-flux polarities

In this section, the possibility to flip the polarity of the half-integer magnetic-flux quanta is shown. Once the sample is cooled down to $T = 4.2$ K, the energy required to alter the polarity of a half magnetic-flux quantum is considerably larger than the thermal energy ($E_b \approx I_c \Phi_0/\pi > 10^4$ K), which is reflected in the temporal stability of the flux pattern. To alter the polarity of the half magnetic-flux quanta, an externally applied magnetic field is required.

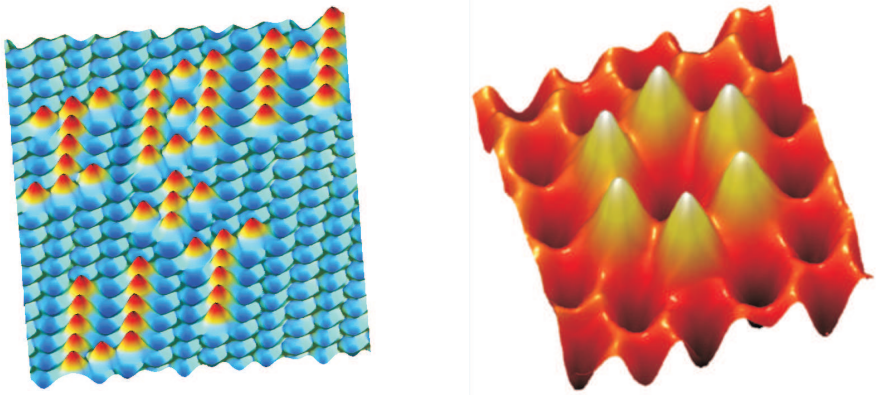

Figure 7.10: [Color] Scanning SQUID microscopy images of two dimensional triangular array of π-loop. In this array, (a) 'IBM+UT' and (b) a hexagonal pattern of six half flux quanta were written by reversing the polarity of selected elements at zero field and $T = 4.2$ K, after cooling in a magnetic field so that all half-vortices initially have the same polarity.

Therefore, by applying locally a magnetic field, the polarity of the individual half-integer flux quanta can be manipulated, enabling the possibilities of storing information or of constructing desired patterns of fractional flux. This is demonstrated in Fig. 7.10. After cooling down the sample in a background magnetic field, which leads to a uniform polarity of half magnetic-flux quanta, a half-vortex pattern demonstrating 'IBM+UT' letters written by setting the polarity of corresponding half-fluxons is demonstrated and shown in Fig. 7.10 (a). Similarly in Fig. 7.10 (b), six half-fluxons in a hexagonal arrangement with opposite polarity to the surrounding half flux quanta are shown. These two patterns were realized in the triangular lattice with 25 μm ring to ring spacing. The polarity of the half flux quanta in this sample with facet length $a = 10$ μm was set by scanning a SQUID susceptometer [78] over the junction at a rate of 0.005 mm/sec while applying a 2 mA current through the excitation coil (this coil is 21 μm in diameter, and concentric and co-planar with the 8 μm square pick-up loop). This corresponds to a field of approximately 50 μT at the junction. Reversing the current direction reversed the resultant polarity of the half-vortex. Remark that, once the sample is heated up above the critical temperature, the information will be destroyed.

Kirtley [121] estimated that the critical field required to flip the polarity of the half-vortex is roughly in agreement with numerical calculations. To estimate theoretically the applied flux required to flip the flux polarity, the sine-Gordon solver [121] discussed in Chapter 6 was used.

Figure 7.11 shows the solution of the Sine-Gordon equation for the 5 μm $0 - \pi$-junction, with a Josephson penetration depth of 1.5 μm. The figure displays $d\phi/dx$,

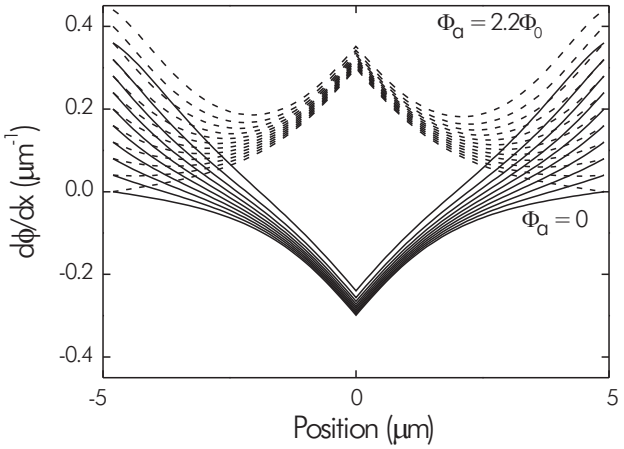

Figure 7.11: The solution of the Sine-Gordon equation for the 5 μm $0-\pi$-junction, with a Josephson penetration depth of 1.5 μm. The applied flux starts out at zero, and is increased in $0.2\Phi_0$ steps (solid lines). The sign of the half-vortex flips at an applied flux of about $2\Phi_0$. The applied flux is then reduced to zero (dashed lines), leaving the half-flux quantum in the opposite state.

where ϕ is the quantum mechanical phase. The flux per unit length per Φ_0 is $\frac{1}{2}\pi d\phi/dx$. To observe the flipping, the applied flux in the calculation is increased in steps until the polarity of the flux is altered. This is shown with solid lines in Fig. 7.11. In this figure, the applied flux starts out at zero, and is increased in $0.2\Phi_0$ steps. The sign of the half-vortex flips at an applied flux of about $2\Phi_0$. The applied flux is then reduced to zero (dashed lines), leaving the half-flux quantum in the opposite state. The prediction for the larger rings with 10 μm facet length, a critical applied flux of about $4\Phi_0$, is also in reasonable agrement with the measurement [121]. When the applied flux is further increased above the critical field, multiple Josephson vortices enter, and then leave again as the flux is lowered, leaving only the half-vortex with the opposite sign.

In addition to the spontaneous flux formation, the writing of half flux quanta patterns provides a diverse basis for both fundamental studies and potential applications. Flipping the polarity of a half-flux quantum while looking at the polarity of another half flux quantum, for example, one can study the possibility to transfer information from one site to another site in the arrays.

Flux calibration

To measure the uniformity of the spontaneous supercurrents in 0-π junction arrays, Kirtley [121] calculated the peak heights of the spontaneously-generated fluxes in the triangular arrays. Figure 7.12 shows a histogram of the peak heights for the data in Fig. 7.7 (b). The peak positions in the histogram are not symmetric because of interactions between the pickup loop and the corner junctions.

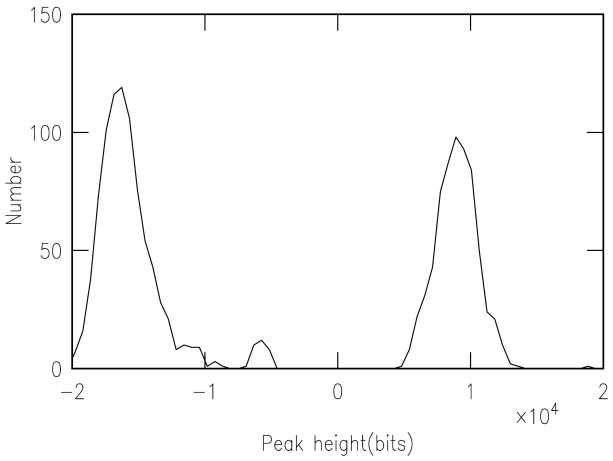

Figure 7.12: The histogram of the peak heights for the data in Fig. 7.7.

The spontaneous currents generated in the corner junctions in the triangular array of Fig. 7.7 were remarkably uniform, as indicated by a full width at half-maximum of the distribution in peak heights which was about 0.28 times the average peak height.

Some spread in the distribution of spontaneous currents is not a dominant source of disorder in the π-ring array cooling experiments because it will cause fluctuations in the amplitude, as opposed to fluctuations in sign, of the ring-ring coupling.

7.2.2 Imaging of the half-vortices arrangement in frustrated versus unfrustrated arrays

For Ising spins on an antiferromagnetic triangular lattice, the ground state is expected not to be unique [131] and there is no long-range antiferromagnetic order. The absence of long-range order originates from geometrical frustration. The magnetic behavior of the ring arrays on this lattice therefore should be different from the magnetic behavior in unfrustrated lattices. To investigate this, the half-vortex arrangements were studied in unfrustrated lattices, and compared with those in frustrated lattices.

Magnetic-coupling optimizations

Another approach employed to build the arrays was by using π-SQUIDs as elements of the lattices. Such elements are sketched in Fig. 7.13. π-SQUIDs have some advantages compared to $0-\pi$ junctions. To spontaneously generate a half magnetic-flux quantum, it is necessary that $2\pi LI_c$ exceeds Φ_0 for a π-SQUID, while for 0-π junctions the requirement is $a \gg \lambda_J \sim 1/\sqrt{J_c}$. In other words, the spontaneously generated fluxes in π-rings are dependent on the critical current I_c and in $0-\pi$ junctions on the critical current density J_c. The junction critical currents in a π-ring can be simply increased by using a much thicker film, and thus enabling smaller planar dimensions. Another

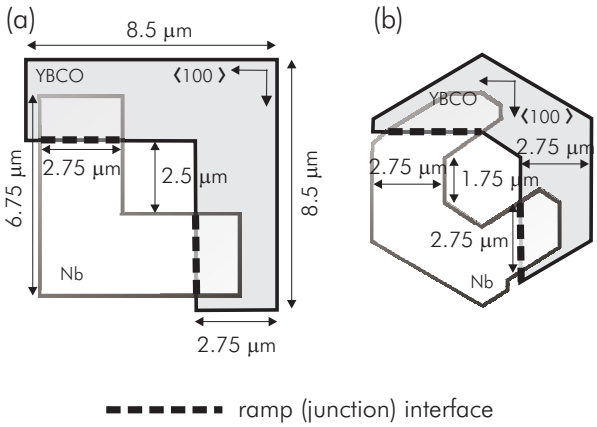

Figure 7.13: Structures of π-rings used as elements for two dimensional lattices; (a) a square-shaped π-SQUID, and (b) an hexagon-shaped π-SQUID.

advantage is that the π-SQUIDs have a higher inductance L than $0-\pi$ junctions with a comparable geometry. This would allow a somewhat lower J_c for π-SQUIDs, still leading to half flux quanta generation. In addition, the flux in the π-SQUIDs is expected to be better shaped because it is not influenced by the Nb overhang as is the case for $0-\pi$ junctions.

To estimate the required π-SQUID dimensions, assume that the current density J_c is $10^4 \mathrm{A/cm}^2$ and the junction thickness 150 nm. For a π-SQUID with inside diameter R, width a, thickness t, the critical current is $I_c = J_c \times at$. An estimate for the ring inductance is $L = 1.25\mu_0 R$ [137]. The factor 1.25 gets bigger for smaller w/R ratios. Assuming that $w = R$, one can show that the requirement $2\pi L I_c = \Phi_0$ becomes

$$R = \sqrt{\frac{\Phi_0}{2.5\pi^2 \mu_0 J_c t}} \tag{7.13}$$

This condition is satisfied for $R = 2.1$ μm, which leads to an outside diameter of 6.3 μm. For a 0-π junction, the requirement is $a > 4.2$ μm so that the length of a facet will be longer than the Josephson penetration depth, assuming the same current density. As a consequence, one can make smaller rings than corner junctions, and still see spontaneous magnetization. Furthermore, the increase in inductance with decreasing a/R would seem to make the advantage of rings slightly stronger. Figure 7.14 plots the spontaneous magnetization as a function of ring inductance L for a π-ring, compared with the spontaneous magnetization as a function of junction width a for a symmetric 0-π junction. For a comparable J_c, the biggest advantage of using π-SQUIDs is that one can just use a thicker layer to end up in the limit of spontaneous half-flux quanta formation, while keeping the planar dimensions small.

To investigate the long-range ordering and frustration effects in the two dimensional antiferromagnetic Ising spins, the magnetic coupling between the flux-generator

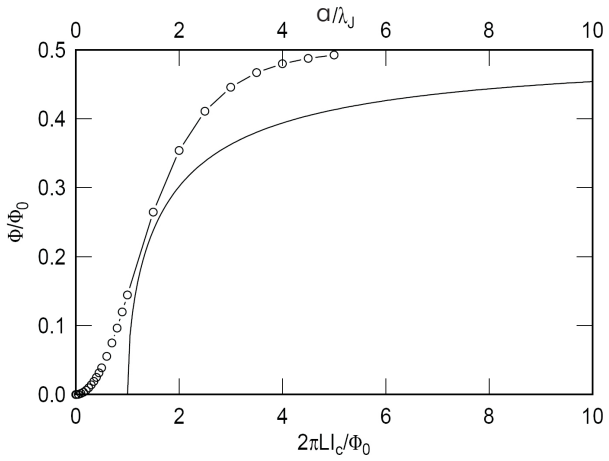

Figure 7.14: The spontaneous magnetization as a function of ring inductance L for a π-ring, and as function of junction width a for a symmetric 0-π junction.

rings at the freezing temperature must be as large as possible, and with a relatively small barrier between the two degenerate states. Both the barrier energy E_b and the coupling energy E_c are temperature dependent. The ratio between E_c and E_b goes as

$$\frac{E_c}{E_b} \sim \frac{M}{L^2 I_c \left(1 - \frac{1}{\beta}\right)} \tag{7.14}$$

Hence, to optimize the magnetic coupling, the mutual inductance M of the rings has to be as large as possible. To maximize the mutual inductance, the rings should be as close to each other as possible, and with as high a critical current density across the junction as possible. However the smallest dimensions of the rings are limited by above mentioned conditions. In addition, lithography also sets a limit to how close the rings can be placed.

Figure 7.15 shows scanning electron micrographs of π-ring arrays in four different lattices: square, triangular, honeycomb, and kagomé, built from $YBa_2Cu_3O_{7-\delta}$/Nb π-SQUIDs. The thickness of $YBa_2Cu_3O_{7-\delta}$ and Nb layer are 300 nm and 160 nm, respectively. To maximize the mutual inductance, the rings were made in square shapes on the square lattices and in hexagonal shapes on the triangular, honeycomb, and kagomé lattices. For both shapes, the inner diameter of the rings is 2.75 μm and the gap between rings is 3.00 μm. In total, the square, triangular, honeycomb, and kagomé lattices have 19600, 22400, 15200, and, 19200 rings, respectively. Note that in the triangular, honeycomb, and kagomé lattices, the rings' dimensions and nearest neighbor spacings are identical, and so, presumably, are the nearest neighbor interactions. Only the lattice connectivity is changed, *i.e.*, all lattices are based on the same triangular arrangement, but some elements are missing in the honeycomb and the kagomé lattice, leaving the remaining elements in the

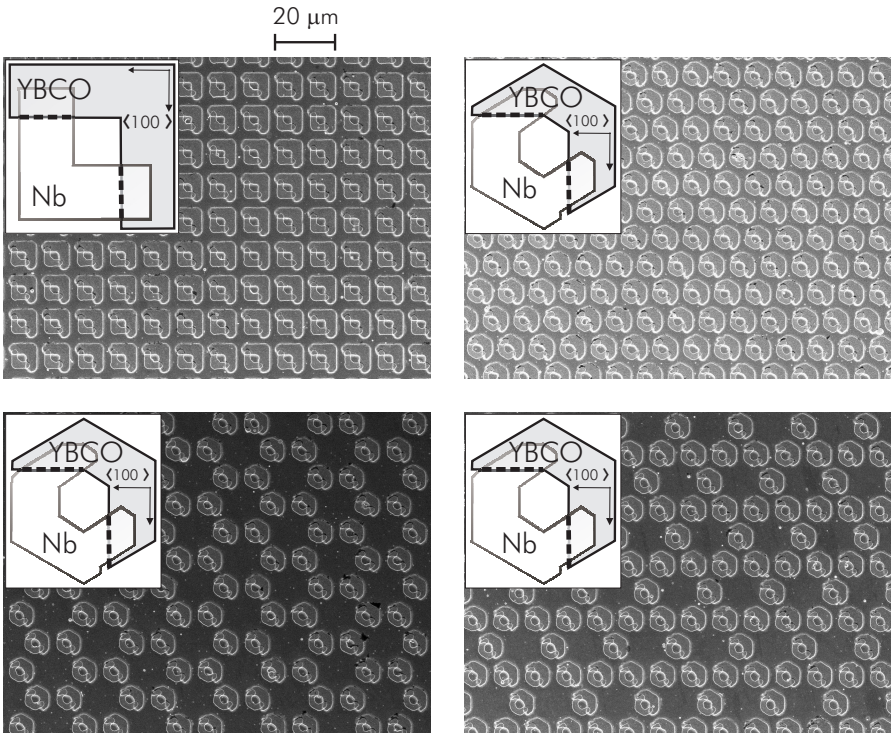

Figure 7.15: SEM micrographs of π-ring arrays with a square (top left), triangular (top right), honeycomb (bottom left), and kagomé lattice (bottom right).

unfrustrated honeycomb and the frustrated kagomé configuration, respectively. For these lattices, also the next nearest neighbor spacings are identical. For the square lattice, in addition to the difference in the ring shape which is square, the next nearest neighbor spacings are also different than the other three lattices.

Imaging results

Figure 7.16 shows scanning SQUID micrographs of the arrangement of the fractional flux quanta in sections of four different lattices: the square, triangular, honeycomb, and kagomé. In these images, the white dots represent rings with supercurrents circulating clockwise, and thus spontaneous fluxes pointing downward; the black dots represent rings with counter-clockwise circulating supercurrents, and thus fluxes pointing upward. The ring configurations presented for the unfrustrated square lattice in Fig. 7.16 (a) and the unfrustrated honeycomb lattice in Fig. 7.16 (c) show that there are no obvious long-range correlations in these arrays. For both configurations, the distribution of the spins also appears to be random. Nevertheless, if one carefully looks, for example, at the left top corner of the honeycomb lattice, there is a nice an-

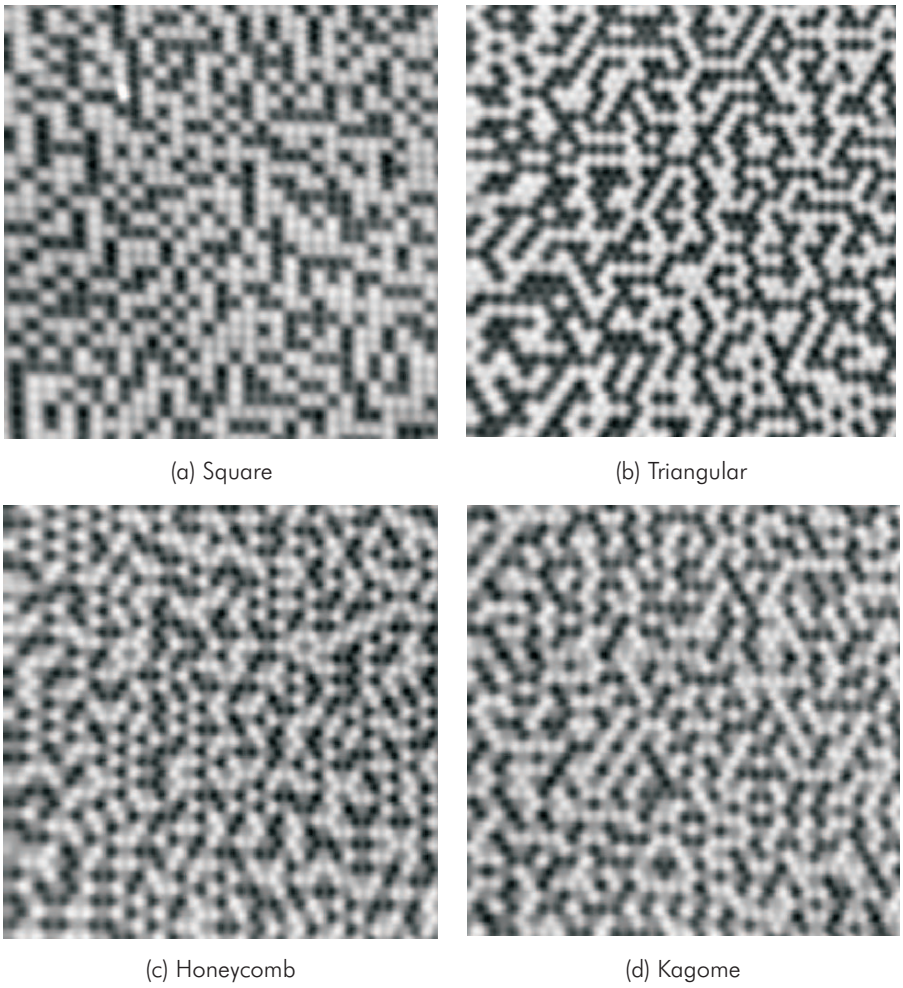

Figure 7.16: Scanning SQUID micrographs of the (a) square, (b) triangular, (c) honeycomb, and (d) kagomé lattices. The black dots represent spins up and white dots spins down.

tiferromagnetic ordering at that specific area. In this case, up to 25 half magnetic-flux quanta are antiferromagnetically arranged.

To see the effects of the lattice geometry, the bond order parameter for frustrated and unfrustrated lattices can be compared, since the difference between all the lattices but the square one is only the lattice geometry. The square lattice is built from a building block which is different than that for the other three lattices. In addition, it has a shorter next-nearest neighbor distance of 11.5 μm, while the others have 22.4 μm. Therefore, the bond order parameter for the triangular, honeycomb, and

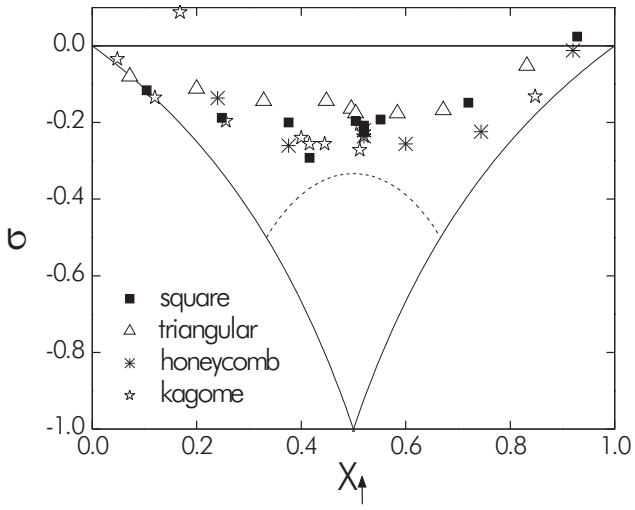

Figure 7.17: σ as a function of the fraction of upward pointing half magnetic-flux quanta for the square, triangular, honeycomb, and kagomé lattice.

kagomé lattices can be compared directly. From the scanning SQUID micrographs presented in Fig. 7.16, the bond order parameters were deduced, which are -0.16, -0.24, -0.25, and -0.26 for the triangular, kagomé, honeycomb, and square lattices, respectively, at $x_\uparrow \sim 0.5$. Except for the triangular array, there is no significant difference between the bond order parameters for both the frustrated and unfrustrated lattices, indicating that most of the disorder in the frustrated lattices is due to the dynamical disorder instead of geometrical frustration effects.

Figure 7.17 shows the bond order parameter for both the unfrustrated and frustrated lattices, as a function of the up-spin fraction in the lattices. The fraction of the up-spins, and thus the down-spins, was modified by cooling the sample in a background field. The transition from all spins up to all spins down was found to be very sharp, which is about 0.9 μT from 80% to 20% spins up. For these rings, one flux quantum is equivalent to 70 μT. This means that the transition width is about 1% of Φ_0. This value is very comparable to the results for unconventional rings discussed in [127], even though the $0-\pi$ rings are much larger.

It can been seen in Fig. 7.17 that there is some scatter in the bond order parameter versus field curves, but there are some real qualitative differences between the arrays: the honeycomb and kagomé lattices have the strongest correlations, peaking at a sigma of -0.25. The triangular lattice has weaker correlations, peaking at about -0.16. Therefore, it can be concluded that open lattices, like the kagomé and honeycomb have stronger antiferromagnetic correlations than the triangle one, and that the effect of lattice geometry is more significant in the triangular lattice. The unfrustrated square lattice has also comparable antiferromagnetic correlations, but recall that in the square lattice the next nearest neighbor spacing is considerably smaller than

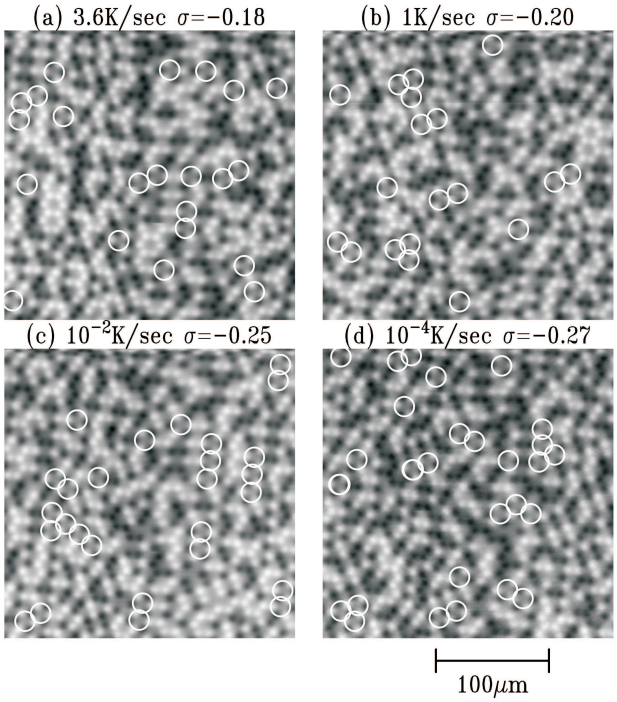

Figure 7.18: Scanning SQUID microscopy images of a honeycomb array in the geometry illustrated in Fig. 7.15, cooled in nominally zero field through the Nb superconducting transition temperature at different cooling rates. The white circles superimposed on the images label 6-ring loops in the honeycomb lattice in which the rings are perfectly antiferromagnetically ordered.

that for the other lattices, leading to presumably a stronger next nearest neighbor interactions.

From the simulation [121], it appears that much of the disorder observed in these array cooling experiments can be attributed to the dynamical effects, as opposed to geometrical frustration effects. This is supported by the fact that the best bond orders obtained for the unfrustrated square and honeycomb lattices are approximately the same as those for the frustrated kagomé lattice.

For the triangular lattice, the best bond order of -0.16 obtained from Fig. 7.16 is considerably better than those obtained from the triangular lattices discussed in Section 7.2.1. In the latter case, the best bond order is only -0.10. The increased bond orders are perhaps due to the increase in current densities and the reduction in inter-ring separation, reducing the dynamical disorder effects. Therefore, the disorder in the triangular arrays may partly be due to the dynamical disorder, but from the significant negative sigma value one may also anticipate that it is partly due to the frustration-effects. The system may not have reached its energetically ground state,

as for this it may need much more time to adjust all the spins during cool-down. The antiferromagnetic ordering therefore should be improved if the arrays are cooled more slowly through the Nb superconducting transition.

Figure 7.18 shows scanning SQUID microscopy images of a honeycomb array in the geometry illustrated in Fig. 7.15, cooled in nominally zero field through the Nb superconducting transition temperature at different cooling rates. Each panel is labeled with the cooling rate and experimentally determined bond order σ. The antiferromagnetic ordering increases with slower cooling rates. One question that can be asked is: Do particular regions of the arrays order more strongly than others? The white circles in Fig. 7.18 outline the 6-member rings in the honeycomb arrays in which all neighbors are antiferromagnetically ordered. This provides a convenient way of visualizing regions of local order. It appears that there are no correlations between the positions of the ordered 6-member rings from cooldown to cooldown, and it can be concluded that the ordered regions are randomly distributed in space.

7.3 Concluding remarks

Two-dimensional isolated π-ring arrays have been realized in various configurations. In isolated π-ring arrays at sufficiently close distances, the half flux quanta are becoming antiferromagnetically arranged owing to magnetic interaction.

The first configuration, for which the generation and coupling of half-integer flux quanta were investigated, was the triangular array. This geometry is of particular interest, as with the preferential antiferromagnetic coupling between the half-integer flux quanta, it provides a model example of a strongly frustrated system, characterized by a highly degenerate ground state. Coupling of the half flux-quanta was also investigated and compared between frustrated and unfrustrated geometries. Investigations of spin interactions on the unfrustrated geometries are a natural way, in which the Néel long range ordering of a spin system can be investigated. It was found that the honeycomb and kagomé lattices have stronger AFM correlations than the triangular lattice, and that the effect of lattice geometry is significant in the triangular lattice. No complete Néel long range ordering has been observed yet in the unfrustrated lattices due to the dynamic disorder. Further detailed studies are still needed.

Bibliography

[1] **Galleher, J.**, The Mobius Transformation, Mobius Product & Services, 2000.

[2] **Geshkenbein, V. B.** and **Larkin, A. I.**, *The Josephson effect in superconductors with heavy fermions*, JETP Lett., Vol. 43, pp. 395, 1986.

[3] **Geshkenbein, V. B., Larkin, A. I.** and **Barone, A.**, *Vortices with half magnetic flux quanta in heavy-fermion superconductors*, Phys. Rev. B, Vol. 36, pp. 235, 1987.

[4] **Sigrist, M.** and **Rice, T. M.**, *Paramagnetic effect in high-T_c superconductors - a hint for d-wave superconductivity*, J. Phys. Soc. Jpn., Vol. 61, pp. 4283, 1992.

[5] **Tsuei, C. C., Kirtley, J. R., Chi, C. C., Yu-jahnes, L. S., Gupta, A., Shaw, T., Sun, J. Z.** and **Ketchen, M. B.**, *Pairing symmetry and flux quantization in a tricrystal superconducting ring of $YBa_2Cu_3O_{7-\delta}$*, Phys. Rev. Lett., Vol. 73, pp. 593, 1994.

[6] **Terzioglu, E.** and **Beasley, M. R.**, *Complementary Josephson junction devices and circuits: A possible new approach to superconducting electronics*, IEEE Trans. Appl. Supercond., Vol. 8, pp. 48, 1998.

[7] **Ioffe, L. B., Geshkenbein, V. B., Feigel'man, M. V., Fauchere, A. L.** and **Blatter, G.**, *Environmentally decoupled sds-wave Josephson junctions for quantum computing*, Nature, Vol. 398, pp. 679, 1999.

[8] **Blatter, G., Geshkenbein, V. B.** and **Ioffe, L. B.**, *Design aspects of superconducting-phase quantum bits*, Phys. Rev. B, Vol. 63, pp. 174511, 2001.

[9] **Gao, J., Aarnink, W. A. M., Gerritsma, G. J.** and **Rogalla, H.**, *Controlled preparation of all high-T_c SNS-type edge junctions and dc squids*, Physica C, Vol. 171, pp. 126, 1990.

[10] **Smilde, H. J. H.**, Josephson Contacts between High-T_c and Low-T_c Superconductors, Ph.D. thesis, Universiteit Twente, 2001.

[11] **Smilde, H. J. H., Hilgenkamp, H., Rijnders, G., Rogalla, H.** and **Blank, D. H. A.**, *Enhanced transparency ramp-type Josephson contacts through interlayer deposition*, Appl. Phys. Lett., Vol. 80, pp. 4579, 2002.

[12] **Jaklevic, R. C., Silver, A. H., Lambe, J.** and **Mercereau, J. E.**, *Quantum interference effects in Josephson tunneling*, Phys. Rev. Lett., Vol. 12, pp. 159, 1964.

[13] **Martinoli, P.** and **Leemann, C.**, *Two dimensional Josephson junction arrays*, J. Low Temp. Phys., Vol. 118, pp. 699, 2000.

[14] **Keene, M. N., Jackson, T. J.** and **Gough, C. E.**, *Demonstration of the phase coherence of the superconducting wavefunctions between conventional and high-T_c superconductors*, Nature, Vol. 340, pp. 210, 1989.

[15] **Gao, J., Boguslavskij, Y., Klopman, B. B. G., Terpstra, D., Gerritsma, G. J.** and **Rogalla, H.**, *Characteristics of advanced $YBa_2Cu_3O_x/PrBa_2Cu_3O_x/YBa_2Cu_3O_x$ edge type junctions*, Appl. Phys. Lett., Vol. 59, pp. 2754, 1991.

[16] **Hilgenkamp, H., Mannhart, J.** and **Mayer, B.**, *Implications of $d_{x^2-y^2}$ symmetry and faceting for the transport properties of grain boundaries in high-T_c superconductors*, Phys. Rev. B, Vol. 53, pp. 14586, 1996.

[17] **Smilde, H. J. H., Ariando, Blank, D. H. A., Gerritsma, G. J., Hilgenkamp, H.** and **Rogalla, H.**, *d-wave-induced Josephson current counterflow in $YBa_2Cu_3O_7/Nb$ zigzag junctions*, Phys. Rev. Lett., Vol. 88, pp. 057004, 2002.

[18] **Ariando, Darminto, D., Smilde, H. J. H., Rogalla, H.** and **Hilgenkamp, H.**, *Phase-sensitive order parameter symmetry test experiments utilizing $Nd_{2-x}Ce_xCuO_{4-y}/Nb$ zigzag junctions*, To be published in Phys. Rev. Lett., 2005.

[19] **Hilgenkamp, H., Ariando, Smilde, H. J. H., Blank, D. H. A., Rijnders, G., Rogalla, H., Kirtley, J. R.** and **Tsuei, C. C.**, *Ordering and manipulation of the magnetic moments in large-scale superconducting π-loop arrays*, Nature, Vol. 422, pp. 50, 2003.

[20] **Kirtley, J. R., Tsuei, C. C., Ariando, Smilde, H. J. H.** and **Hilgenkamp, H.**, *Anti-ferromagnetic ordering in arrays of superconducting π-rings*, Submitted to Phys. Rev. B, 2005.

[21] **Smilde, H. J. H., Ariando, Rogalla, H.** and **Hilgenkamp, H.**, *Bistable superconducting quantum interference device with built-in switchable $\pi/2$ phase shift*, Appl. Phys. Lett., Vol. 85, pp. 4091, 2004.

[22] **Smilde, H. J. H., Ariando, Blank, D. H. A., Hilgenkamp, H.** and **Rogalla, H.**, *π-SQUIDs based on Josephson contacts between high-T_c and low-T_c superconductors*, Phys. Rev. B, Vol. 70, pp. 024519, 2004.

[23] **Gerritsma, G.**, *Using $Nb/YBa_2Cu_3O_{7-\delta}$-based π-SQUIDs in RSFQ logic circuits*, *Presentation at First Internatonal Workshop on the symmetry in Macroscopic Quantum States*, Augsburg, Germany, May 2002.

[24] **Tinkham, M.**, Introduction to Superconductivity, McGraw-Hill, Inc., 1996.

[25] **van Duzer, T.** and **Turner, C. W.**, Principles of Superconductive Devices and Circuits, Prentice-Hall, Inc., 1999.

[26] **Tsuei, C. C.** and **Kirtley, J. R.**, *Pairing symmetry in cuprate superconductors*, Rev. Mod. Phys., Vol. 72, pp. 969, 2000.

[27] **Takeuchi, I., Mao, S. N., Xi, X. X., Petersen, K., Lobb, C. J.** and **Venkatesan, T.**, *Observation of Josephson effect in $YBa_2Cu_3O_{7-x}/Nd_{1.85}Ce_{0.15}CuO_{4-y}$ bilayer junctions*, Appl. Phys. Lett., Vol. 67, pp. 2872, 1995.

[28] **Josephson, B. D.**, *Possible new effects in superconductive tunnelling*, Phys. Lett., Vol. 1, pp. 251, 1962.

[29] **Ferrell, R. A.**, *Josephson tunneling and quantum mechanical phase*, Phys. Rev. Lett., Vol. 15, pp. 527, 1965.

[30] **Owen, C. S.** and **Scalapino, D. J.**, *Inductive coupling of Josephson junctions to external circuits*, J. Appl. Phys., Vol. 41, pp. 2047, 1970.

[31] **Barone, A.** and **Paterno, G.**, Physics and Application of the Josephson Effect, John Wiley & Sons, 1982.

[32] **Tesche, C. D.** and **Clarke, J.**, *DC squid - noise and optimization*, J. Low Temp. Phys., Vol. 29, pp. 310, 1977.

[33] **Giaver, I.**, *Energy gap in superconductors measured by electron tunneling*, Phys. Rev. Lett., Vol. 5, pp. 147, 1960.

[34] **van Harlingen, D. J.**, *Phase-sensitive tests of the symmetry of the pairing state in the high-temperature superconductors—Evidence for $d_{x^2-y^2}$ symmetry*, Rev. Mod. Phys., Vol. 67, pp. 515, 1995.

[35] **Gor'kov, L. P.**, *Microscopic derivation of the Ginzburg-Landau equations in the theory of superconductivity*, Soviet Phys. JETP, Vol. 9, pp. 1364, 1959.

[36] **Anderson, P. W.**, The Theory of Superconductivity in the High-T_c Cuprates, Princeton University, 1997.

[37] **Janossy, B., Hergt, R.** and **Fruchter, L.**, *Contributions of pinning and anisotropy to torque in YBaCuO*, Physica C, Vol. 170, pp. 22, 1990.

[38] **Chien, T. R., Datars, W. R., Lan, M. D., Liu, J. Z.** and **Shelton, R. N.**, *Anisotropy of $YBa_2Cu_3O_{7-\delta}$ single crystals studied by torque magnetometry*, Phys. Rev. B, Vol. 49, pp. 1342, 1994.

[39] **Bickers, N. E., Scalapino, D. J.** and **White, S. R.**, *Conserving approximations for strongly correlated electron-systems - Bethe-Salpeter-equation and dynamics for the two-dimensional Hubbard-model*, Phys. Rev. Lett., Vol. 62, pp. 961, 1989.

[40] **Annet, J. F., Goldenfeld, N.** and **Renn, S. R.**, Physical Properties of High Temperature Superconductors II, World Scientific, 1990.

[41] **Ambegaokar, V.** and **Baratoff, A.**, *Tunneling between superconductors*, Phys. Rev. Lett., Vol. 10, pp. 486, 1963.

[42] **Ambegaokar, V.** and **Baratoff, A.**, *Errata: Tunneling between superconductors*, Phys. Rev. Lett., Vol. 11, pp. 104, 1963.

[43] **Ketterson, J. B.** and **Song, S. N.**, Superconductivity, Cambridge University Press, 1999.

[44] **Wollman, D. A., van Harlingen, D. J., Giapintzakis, J.** and **Ginsberg, D. M.**, *Evidence for $d_{x^2-y^2}$ pairing from the magnetic field modulation of $YBa_2Cu_3O_7$-Pb Josephson junctions*, Phys. Rev. Lett., Vol. 74, pp. 797, 1995.

[45] **Miller Jr., J. H., Ying, Q. Y., Zou, Z. G., Fan, N. Q., Xu, J. H., Davis, M. F.** and **Wolfe, J. C.**, *Use of tricrystal junctions to probe the pairing state symmetry of $YBa_2Cu_3O_{7-\delta}$*, Phys. Rev. Lett., Vol. 74, pp. 2347, 1995.

[46] **Wollman, D. A., van Harlingen, D. J., Lee, W. C., Ginsberg, D. M.** and **Leggett, A. J.**, *Experimental determination of the superconducting pairing state in YBCO from the phase coherence of YBCO-Pb dc SQUIDs*, Phys. Rev. Lett., Vol. 71, pp. 2134, 1993.

[47] **Mathai, A., Gim, Y., Black, R. C., Amar, A.** and **Wellstood, F. C.**, *Experimental proof of a time-reversal-invariant order parameter with a π shift in $YBa_2Cu_3O_{7-\delta}$*, Phys. Rev. Lett., Vol. 74, pp. 4523, 1995.

[48] **Brawner, D. A.** and **Ott, H. R.**, *Evidence for an unconventional superconducting order-parameter in $YBa_2Cu_3O_{6.9}$*, Phys. Rev. B, Vol. 50, pp. 6530, 1994.

[49] **Chesca, B.**, *Magnetic field dependencies of the critical current and of the resonant modes of dc SQUIDs fabricated from superconductors with $s + id_{x^2-y^2}$ order-parameter symmetries*, Ann. Phys. (Leipzig), Vol. 8, pp. 511, 1999.

[50] **Schulz, R. R., Chesca, B., Goetz, B., Schneider, C. W., Schmehl, A., Bielefeldt, H., Hilgenkamp, H., Mannhart, J.** and **Tsuei, C. C.**, *Design and realization of an all d-wave dc π-superconducting quantum interference device*, Appl. Phys. Lett., Vol. 76, pp. 912, 2000.

[51] **Kirtley, J. R.**, *SQUID microscopy for fundamental studies*, Physica C, Vol. 368, pp. 55, 2002.

[52] **Copetti, C. A., Rüders, F., Oelze, B., Buchal, C., Kabius, B.** and **Seo, J. W.**, *Electrical-properties of 45° grain-boundaries of epitaxial YBaCuO, dominated by crystalline microstructure and d-wave-symmetry*, Physica C, Vol. 253, pp. 63, 1995.

[53] **Mannhart, J., Mayer, B.** and **Hilgenkamp, H.**, *Anomalous dependence of the critical current of* 45° *grain boundaries in* $YBa_2Cu_3O_{7-x}$ *on an applied magnetic field*, Z. Phys. B, Vol. 101, pp. 175, 1996.

[54] **Hilgenkamp, H.** and **Mannhart, J.**, *Grain boundaries in high-*T_c *superconductors*, Rev. Mod. Phys., Vol. 74, pp. 485, 2002.

[55] **Mints, R. G.** and **Kogan, V. G.**, *Josephson junctions with alternating critical current density*, Phys. Rev. B, Vol. 55, pp. R8682, 1997.

[56] **Kirtley, J. R., Chaudhari, P., Ketchen, M. B., Khare, N., Lin, S. Y.** and **Shaw, T.**, *Distribution of magnetic flux in high-*T_c *grain-boundary junctions enclosing hexagonal and triangular areas*, Phys. Rev. B, Vol. 51, pp. 12057, 1995.

[57] **Mannhart, J., Hilgenkamp, H., Mayer, B., Gerber, C., Kirtley, J. R., Moler, K. A.** and **Sigrist, M.**, *Generation of magnetic flux by single grain boundaries of* $YBa_2Cu_3O_{7-x}$, Phys. Rev. Lett., Vol. 77, pp. 2782, 1996.

[58] **Il'ichev, E., Zakosarenko, V., Ijsselsteijn, R. P. J., Schultze, V., Meyer, H. G., Hoenig, H. E., Hilgenkamp, H.** and **Mannhart, J.**, *Non-sinusoidal current-phase relationship of grain boundary Josephson junctions in high-*T_c *superconductors*, Phys. Rev. Lett., Vol. 81, pp. 894, 1998.

[59] **Il'ichev, E., Grajcar, M., Hlubina, R., IJsselsteijn, R. P. J., Hoenig, H. E., Meyer, H. G., Golubov, A. A., Amin, M. H. S., Zagoskin, A. M., Omelyanchouk, A. N.** and **Kupriyanov, M. Y.**, *Degenerate ground state in a mesoscopic* $YBa_2Cu_3O_{7-x}$ *grain boundary Josephson junction*, Phys. Rev. Lett., Vol. 86, pp. 5369, 2001.

[60] **Golubov, A. A., Kupriyanov, M. Y.** and **Il'ichev, E.**, *The current-phase relation in Josephson junctions*, Rev. Mod. Phys., Vol. 76, pp. 411, 2004.

[61] **Bulaevskii, L. N., Kuzii, V. V.** and **Sobyanin, A. A.**, *Superconducting system with weak coupling to current in ground-state*, JETP Lett., Vol. 25, pp. 290, 1977.

[62] **Spivak, B. I.** and **Kivelson, S. A.**, *Negative local superfluid densities: The difference between dirty superconductors and dirty Bose liquids*, Phys. Rev. B, Vol. 43, pp. 3740, 1991.

[63] **Ryazanov, V. V., Oboznov, V. A., Rusanov, A. Y., Veretennikov, A. V., Golubov, A. A.** and **Aarts, J.**, *Coupling of two superconductors through a ferromagnet: Evidence for a* π *junction*, Phys. Rev. Lett., Vol. 86, pp. 2427, 2001.

[64] **Kontos, T., Aprili, M., Lesueur, J., Genet, F., Stephanidis, B.** and **Boursier, R.**, *Josephson junction through a thin ferromagnetic layer: Negative coupling*, Phys. Rev. Lett., Vol. 89, pp. 137007, 2002.

[65] **Baselmans, J. J. A., Morpurgo, A. F., van Wees, B. J.** and **Klapwijk, T. M.**, *Reversing the direction of the supercurrent in a controllable Josephson junction*, Nature, Vol. 397, pp. 43, 1999.

[66] **Baselmans, J. J. A., van Wees, B. J.** and **Klapwijk, T. M.**, *Controllable π SQUID*, Appl. Phys. Lett., Vol. 79, pp. 2940, 2001.

[67] **Baselmans, J. J. A., Heikkil, T. T., van Wees, B. J.** and **Klapwijk, T. M.**, *Direct observation of the transition from the conventional superconducting state to the π state in a controllable Josephson junction*, Phys. Rev. Lett., Vol. 89, pp. 207002, 2002.

[68] **Goldobin, E., Sterck, A., Gaber, T., Koelle, D.** and **Kleiner, R.**, *Dynamics of semifluxons in Nb long Josephson 0-π junctions*, Phys. Rev. Lett., Vol. 92, pp. 057005, 2004.

[69] **Verhoeven, M. A. J., Moerman, R., Bijlsma, M. E., Rijnders, A. J. H. M., Blank, D. H. A., Gerritsma, G. J.** and **Rogalla, H.**, *Nucleation and growth of $PrBa_2Cu_3O_{7-\delta}$ barrier layers on ramps in $DyBa_2Cu_3O_{7-\delta}$ studied by atomic force microscopy*, Appl. Phys. Lett., Vol. 68, pp. 1276, 1996.

[70] **Koster, G., Kropman, B. L., Rijnders, G. J. H. M., Blank, D. H. A.** and **Rogalla, H.**, *Quasi-ideal strontium titanate crystal surfaces through formation of strontium hydroxide*, Appl. Phys. Lett., Vol. 73, pp. 2920, 1998.

[71] **Dekkers, J. M., Rijnders, G., Harkema, S., Smilde, H., Hilgenkamp, H., Rogalla, H.** and **Blank, D. H. A.**, *Monocrystalline $YBa_2Cu_3O_{7-x}$ thin films on vicinal $SrTiO_3$ (001) substrates*, Appl. Phys. Lett., Vol. 83, pp. 5199, 2003.

[72] **Blank, D. H. A.** and **Rogalla, H.**, *Effect of ion milling on the morphology of ramp-type Josephson junctions*, J. Mater. Res., Vol. 12, pp. 2952, 1997.

[73] **Straub, R.**, Abbildung von Flussquanten in $YBa_2Cu_3O_{7-x}$ SQUIDs und Josephsonstromen in $YBa_2Cu_3O_{7-x}$-Niob Kontakten, Ph.D. thesis, Universitat Tubingen, 2003.

[74] **Gross, R.** and **Koelle, D.**, *Low-temperature scanning electron-microscopy of superconducting thin-films and Josephson-junctions*, Rep. Prog. Phys., Vol. 57, pp. 651, 1994.

[75] **Kirtley, J. R., Ketchen, M. B., Stawiasz, K. G., Sun, J. Z., Gallagher, W. J., Blanton, S. H.** and **Wind, S. J.**, *High-resolution scanning SQUID microscope*, Appl. Phys. Lett., Vol. 66, pp. 1138, 1995.

[76] **Kirtley, J. R., Ketchen, M. B., Tsuei, C. C., Sun, J. Z., Gallagher, W. J., Yu-Jahnes, L. S., Gupta, A., Stawiasz, K. G.** and **Wind, S. J.**, *Design and applications of a scanning SQUID microscope*, IBM J. Res. Develop., Vol. 39, pp. 655, 1995.

[77] **Bjornsson, P. G., Gardner, B. W., Kirtley, J. R.** and **Moler, K. A.**, *Scanning superconducting quantum interference device microscope in a dilution refrigerator*, Rev. Sci. Inst., Vol. 72, pp. 4153, 2001.

[78] **Gardner, B. W., Wynn, J. C., Bjornsson, P. G., Straver, E. W., Moler, K. A., Kirtley, J. R.** and **Ketchen, M. B.**, *Scanning superconducting quantum interference device susceptometry*, Rev. Sci. Inst., Vol. 72, pp. 2361, 2001.

[79] **Troeman, A.**, Fabrication and characterization of sub-micron sized DC SQUIDs based on Niobium nanobridges, Master's thesis, University of Twente, 2003.

[80] **Smilde, H. J. H., Hilgenkamp, H., Gerritsma, G. J., Blank, D. H. A.** and **Rogalla, H.**, *Realization and properties of ramp-type $YBa_2Cu_3O_{7-\delta}/Au/Nb$ junctions*, Physica C, Vol. 350, pp. 269, 2001.

[81] **Smilde, H. J. H., Hilgenkamp, H., Gerritsma, G. J., Blank, D. H. A.** and **Rogalla, H.**, *Y-Ba-Cu-O/Au/Nb ramp-type Josephson junctions*, IEEE Trans. Appl. Supercond., Vol. 11, pp. 501, 2001.

[82] **Mints, R. G.** and **Papiashvili, I.**, *Self-generated magnetic flux in $YBa_2Cu_3O_{7-x}$ grain boundaries*, Phys. Rev. B, Vol. 62, pp. 15214, 2000.

[83] **Zenchuk, A.** and **Goldobin, E.**, *Analysis of ground states of 0-π long Josephson junctions*, Phys. Rev. B, Vol. 69, pp. 024515, 2004.

[84] **Hu, C. R.**, *Midgap surface states as a novel signature for $d_{x^2-y^2}$-wave superconductivity*, Phys. Rev. Lett., Vol. 72, pp. 1526, 1994.

[85] **Kashiwaya, S.** and **Tanaka, Y.**, *Tunnelling effects on surface bound states in unconventional superconductors*, Rep. Prog. Phys., Vol. 63, pp. 1641, 2000.

[86] **Rosenthal, P. A., Beasley, M. R., Char, K., Colclough, M. S.** and **Zaharchuk, G.**, *Flux focusing effects in planar thin-film grain-boundary Josephson-junctions*, Appl. Phys. Lett., Vol. 59, pp. 3482, 1991.

[87] **Humphreys, R. G.** and **Edwards, J. A.**, *$YBa_2Cu_3O_7$ thin-film grain-boundary junctions in a perpendicular magnetic-field*, Physica C, Vol. 210, pp. 42, 1993.

[88] **Clem, J. R.** and **Huebener, R. P.**, *Application of low-temperature scanning electron-microscopy to superconductors*, J. Appl. Phys, Vol. 51, pp. 2764, 1980.

[89] **Huebener, R. P.**, *Applications of low-temperature scanning electron-microscopy*, Rep. Prog. Phys., Vol. 47, pp. 175, 1984.

[90] **Chang, J. J.** and **Scalapino, D. J.**, *Effects of a focused laser-beam on the critical Josephson tunneling current*, Phys. Rev. B, Vol. 29, pp. 2843, 1984.

[91] **Chang, J. J.** and **Ho, C. H.**, *Nonlocal response to a focused laser-beam in one-dimensional Josephson tunnel-junctions*, Appl. Phys. Lett, Vol. 45, pp. 182, 1984.

[92] **Bosch, J., Gross, R., Koyanagi, M.** and **Huebener, R. P.**, *Direct probing of the spatial-distribution of the maximum josephson current in a superconducting tunnel junction*, Phys. Rev. Lett., Vol. 54, pp. 1448, 1985.

[93] **Bosch, J., Gross, R., Koyanagi, M.** and **Huebener, R. P.**, *Measurement of the spatial-distribution of the maximum Josephson current in superconducting tunnel-junctions*, J. Low Temp. Phys., Vol. 68, pp. 245, 1987.

[94] **Tsuei, C. C.** and **Kirtley, J. R.**, *Phase-sensitive evidence for d-wave pairing symmetry in electron-doped cuprate superconductors*, Phys. Rev. Lett., Vol. 85, pp. 182, 2000.

[95] **Chesca, B., Ehrhardt, K., Mossle, M., Straub, R., Koelle, D., Kleiner, R.** and **Tsukada, A.**, *Magnetic-field dependence of the maximum supercurrent of $La_{2-x}Ce_xCuO_{4-y}$ interferometers: Evidence for a predominant $d_{x^2-y^2}$ superconducting order parameter*, Phys. Rev. Lett., Vol. 90, pp. 057004, 2003.

[96] **Ekin, J. W., Zu, Y., Mao, S., Venkatesan, T., Face, D. W., Eddy, M.** and **Wolf, S. A.**, *Correlation between d-wave pairing behavior and magnetic-field-dependent zero-bias conductance peak*, Phys. Rev. B, Vol. 56, pp. 13746, 1997.

[97] **Kashiwaya, S., Ito, T., Oka, K., Ueno, S., Takashima, H., Koyanagi, M., Tanaka, Y.** and **Kajimura, K.**, *Tunneling spectroscopy of superconducting $Nd_{1.85}Ce_{0.15}CuO_{4-\delta}$*, Phys. Rev. B, Vol. 57, pp. 8680, 1998.

[98] **Alff, L., Beck, A., Gross, R., Marx, A., Kleefisch, S., Bauch, T., Sato, H., Naito, M.** and **Koren, G.**, *Observation of bound surface states in grain-boundary junctions of high-temperature superconductors*, Phys. Rev. B, Vol. 58, pp. 11197, 1998.

[99] **Skinta, J. A., Kim, M. S., Lemberger, T. R., Greibe, T.** and **Naito, M.**, *Evidence for a transition in the pairing symmetry of the electron-doped cuprates $La_{2-x}Ce_xCuO_{4-y}$ and $Pr_{2-x}Ce_xCuO_{4-y}$*, Phys. Rev. Lett., Vol. 88, pp. 207005, 2002.

[100] **Kim, M. S., Skinta, J. A., Lemberger, T. R., Tsukada, A.** and **Naito, M.**, *Magnetic penetration depth measurements of $Pr_{2-x}Ce_xCuO_{4-\delta}$ films on buffered substrates: Evidence for a nodeless gap*, Phys. Rev. Lett., Vol. 91, pp. 087001, 2003.

[101] **Alff, L., Meyer, S., Kleefisch, S., Schoop, U., Marx, A., Sato, H., Naito, M.** and **Gross, R.**, *Anomalous low temperature behavior of superconducting $Nd_{1.85}Ce_{0.15}CuO_{4-y}$*, Phys. Rev. Lett., Vol. 83, pp. 2644, 1999.

[102] **Anlage, S. M., Wu, D. H., Mao, J., Mao, S. N., Xi, X. X., Venkatesan, T., Peng, J. L.** and **Greene, R. L.**, *Electrodynamics of $Nd_{1.85}Ce_{0.15}CuO_4$ - comparison with Nb and $YBa_2Cu_3O_{7-\delta}$*, Phys. Rev. B, Vol. 50, pp. 523, 1994.

[103] **Wu, D. H., Mao, J., Mao, S. N., Peng, J. L., Xi, X. X., Venkatesan, T., Greene, R. L.** and **Anlage, S. M.**, *Temperature dependence of penetration depth and surface resistance of $Nd_{1.85}Ce_{0.15}CuO_4$*, Phys. Rev. Lett., Vol. 70, pp. 85, 1993.

[104] **Andreone, A., Cassinese, A., Chiara, A. D., Vaglio, R., Gupta, A.** and **Sarnelli, E.**, *Temperature-dependence of the penetration depth in $Nd_{1.85}Ce_{0.15}CuO_{4-\delta}$ superconducting thin-films*, Phys. Rev. B, Vol. 49, pp. 6392, 1994.

[105] **Armitage, N. P., Lu, D. H., Peng, D. L., Kim, C., Damascelli, A., Shen, K. M., Ronning, F., Shen, Z. X., Onose, Y., Taguchi, Y.** and **Tokura, Y.**, *Superconducting gap anisotropy in $Nd_{1.85}Ce_{0.15}CuO_4$: Results from photoemission*, Phys. Rev. Lett., Vol. 86, pp. 1126, 2001.

[106] **Sato, T., Kamiyama, T., Takahashi, T., Kurahashi, K.** and **Yamada, K.**, *Observation of $d_{x^2-y^2}$-like superconducting gap in an electron-doped high-temperature superconductor*, Science, Vol. 291, pp. 1517, 2001.

[107] **Kokales, J. D., Fournier, P., Mercaldo, L. V., Talanov, V. V., Greene, R. L.** and **Anlage, S. M.**, *Microwave electrodynamics of electron-doped cuprate superconductors*, Phys. Rev. Lett., Vol. 85, pp. 3696, 2000.

[108] **Prozorov, R., Giannetta, R. W., Fournier, P.** and **Greene, R. L.**, *Evidence for nodal quasiparticles in electron-doped cuprates from penetration depth measurements*, Phys. Rev. Lett., Vol. 85, pp. 3700, 2000.

[109] **Hayashi, F., Ueda, E., Sato, M., Kurahashi, K.** and **Yamada, K.**, *Anisotropy of the superconducting order parameter of $Nd_{2-x}Ce_xCuO_4$ studied by STM/STS*, J. Phys. Soc. Jpn., Vol. 67, pp. 3234, 1998.

[110] **Chesca, B., Seifried, M., Dahm, T., Schopohl, N., Koelle, D., Kleiner, R.** and **Tsukada, A.**, *Observation of Andreev bound states in bicrystal grain-boundary Josephson junctions of the electron-doped superconductor $La_{2-x}Ce_xCuO_{4-y}$*, Phys. Rev. B, Vol. 71, pp. 104504, 2005.

[111] **Biswas, A., Fournier, P., Qazilbash, M. M., Smolyaninova, V. N., Balci, H.** and **Greene, R. L.**, *Evidence of a d- to s-wave pairing symmetry transition in the electron-doped cuprate superconductor $Pr_{2-x}Ce_xCuO_4$*, Phys. Rev. Lett., Vol. 88, pp. 207004, 2002.

[112] **Qazilbash, M. M., Biswas, A., Dagan, Y., Ott, R. A.** and **Greene, R. L.**, *Point-contact spectroscopy of the electron-doped cuprate superconductor $Pr_{2-x}Ce_xCuO_4$: The dependence of conductance-voltage spectra on cerium doping, barrier strength, and magnetic field*, Phys. Rev. B, Vol. 68, pp. 024502, 2003.

[113] **Balci, H.** and **Greene, R. L.**, *Anomalous change in the field dependence of the electronic specific heat of an electron-doped cuprate superconductor*, Phys. Rev. Lett., Vol. 93, pp. 067001, 2004.

[114] **Takagi, H., Uchida, S.** and **Tokura, Y.**, *Superconductivity produced by electron doping in CuO_2-layered compounds*, Phys. Rev. Lett., Vol. 62, pp. 1197, 1989.

[115] **Sigrist, M.** and **Rice, T. M.**, *Unusual paramagnetic phenomena in granular high-temperature superconductors—A consequence of d-wave pairing?*, Rev. Mod. Phys., Vol. 67, pp. 503, 1995.

[116] **Tsuei, C. C.** and **Kirtley, J. R.**, *Tricrystal tunneling evidence for d-wave pairing symmetry in cuprate superconductors*, J. Alloys Compd., Vol. 250, pp. 615, 1997.

[117] **Tsuei, C. C., Kirtley, J. R., Rupp, M., Sun, J. Z., Gupta, A.** and **Ketchen, M. B.**, *Pairing symmetry in single-layer tetragonal $Tl_2Ba_2CuO_{6+\delta}$ superconductors*, Science, Vol. 272, pp. 329, 1996.

[118] **Kirtley, J. R., Tsuei, C. C., Raffy, H., Li, Z. Z., Gupta, A., Sun, J. Z.** and **Megert, S.**, *Half-integer flux quantum effect in tricrystal $Bi_2Sr_2CaCu_2O_{8+\delta}$*, Europhys. Lett., Vol. 36, pp. 707, 1996.

[119] **Kirtley, J. R., Moler, K. A.** and **Scalapino, D. J.**, *Spontaneous flux and magnetic-interference patterns in 0-π Josephson junctions*, Phys. Rev. B, Vol. 56, pp. 886, 1997.

[120] **Xu, J. H., J. H. Miller, J.** and **Ting, C. S.**, *π-vortex state in a long 0-π Josephson junction*, Phys. Rev. B, Vol. 51, pp. 11958, 1995.

[121] **Kirtley, J. R.**, *Private communications.*

[122] **Goldobin, E., Koelle, D.** and **Kleiner, R.**, *Ground states and bias-current-induced rearrangement of semifluxons in 0-π long Josephson junctions*, Phys. Rev. B, Vol. 67, pp. 224515, 2003.

[123] **Ising, E.**, *Report on the theory of ferromagnetism*, Z. Phys., Vol. 31, pp. 253, 1925.

[124] **Kirtley, J. R., Tsuei, C. C.** and **Tafuri, F.**, *Thermally activated spontaneous fluxoid formation in superconducting thin film rings*, Phys. Rev. Lett., Vol. 90, pp. 257001, 2003.

[125] **Pannetier, B., Chaussy, J., Rammal, R.** and **Villegier, J. C.**, *Experimental fine tuning of frustration: Two-dimensional superconducting network in a magnetic field*, Phys. Rev. Lett., Vol. 53, pp. 1845, 1984.

[126] **Davidovic, D., Kumar, S., Reich, D. H., Siegel, J., Field, S. B., Tiberio, R. C., Hey, R.** and **Ploog, K.**, *Correlations and disorder in arrays of magnetically coupled superconducting rings*, Phys. Rev. Lett., Vol. 76, pp. 815, 1997.

[127] **Davidovic, D., Kumar, S., Reich, D. H., Siegel, J., Field, S. B., Tiberio, R. C., Hey, R.** and **Ploog, K.**, *Magnetic correlations, geometrical frustration, and tunable disorder in arrays of superconducting rings*, Phys. Rev. B, Vol. 55, pp. 6518, 1996.

[128] **Davidovic, D.**, Correlations, disorder, and frustration in arrays of magnetically-coupled superconducting rings, Ph.D. thesis, The Johns Hopkins University, 1996.

[129] **Lerch, P., Leemann, C., Theron, R.** and **Martinoli, P.**, *Dynamics of the phase-transition in proximity-effect arrays of Josephson-junctions at full frustration*, Phys. Rev. B, Vol. 41, pp. 11579, 1990.

[130] **Aeppli, G.** and **Chandra, P.**, *Seeking a simple complex system*, Science, Vol. 275, pp. 177, 1997.

[131] **Liebmann, R.**, Statistical Mechanics of Periodic Frustrated Ising Systems, Springer-Verlag Berlin Heidelberg, 1986.

[132] **Anderson, P. W.**, *Ordering and antiferromagnetism in ferrites*, Phys. Rev., Vol. 102, pp. 1008, 1956.

[133] **Obradors, X., Labarta, A., Isalgue, A., Tejada, J., Rodriguez, J.** and **Pernet, M.**, *Magnetic frustration and lattice dimensionality in* $SrCr_8Ga_4O_{19}$, Solid State Commun., Vol. 65, pp. 189, 1988.

[134] **Ramirez, A. P.** and **Cooper, G. P. E. A. S.**, *Strong frustration and dilution-enhanced order in a quasi-2D spin glass*, Phys. Rev. Lett., Vol. 64, pp. 2070, 1990.

[135] **Mendels, P., Keren, A., Limot, L., Mekata, M., Collin, G.** and **Horvatic, M.**, *Ga NMR study of the local susceptibility in Kagom-based* $SrCr_8Ga_4O_{19}$*: Pseudogap and paramagnetic defects*, Phys. Rev. Lett., Vol. 85, pp. 3496, 2000.

[136] **Coley, J. M.**, *An approximate theory of order in alloys*, Phys. Rev., Vol. 77, pp. 669, 1950.

[137] **Jaycox, J. M.** and **Ketchen, M. B.**, *Planar coupling scheme for ultra low-noise dc squids*, IEEE Trans. on Magn., Vol. MAG-17, pp. 400, 1981.

Summary

Using thin-film ramp-type Josephson contacts between a high-T_c and a low-T_c superconductor, experiments to study the $d_{x^2-y^2}$-wave-induced π-phase-shift effects in planar Josephson arrays have been enabled. The presented studies include the first experimental realization of various complex Josephson arrays with built-in π-phase shifts, investigations on the order parameter symmetry in various high-T_c cuprate superconductors, the first direct imaging of $d_{x^2-y^2}$-wave induced Josephson current counter flow, and half-integer magnetic-flux quantum effects in one- and two-dimensional arrays.

It is widely accepted that the high-T_c cuprate $YBa_2Cu_3O_{7-\delta}$ has a $d_{x^2-y^2}$-wave order parameter symmetry. For this reason, the first Josephson arrays for which the $d_{x^2-y^2}$-wave-induced π-phase-shift effects were investigated, were between the high-T_c cuprate $YBa_2Cu_3O_{7-\delta}$ and the low-T_c Nb superconductor. The investigations were first performed on Josephson arrays with a zigzag configuration. In this structure, the $d_{x^2-y^2}$-wave order parameter of the $YBa_2Cu_3O_{7-\delta}$ induces a difference of π in the Josephson phase-shift ϕ across the $YBa_2Cu_3O_{7-\delta}$-Nb barrier for neighboring facets.

One of the particularly interesting aspects of the zigzag junctions is presented by the dependencies of the critical current on magnetic fields. For facet lengths a in the small limit, *i.e.*, $a \ll \lambda_J$, with λ_J the Josephson penetration depth, the magnetic field dependence of the critical current of this type of junction presents an anomalous pattern. No zero-field maximum nor any obvious declining envelope around zero-field in the magnetic field dependence of the critical current occurs. In stark contrast to a standard Fraunhofer-like magnetic field dependence of the critical current for conventional Josephson junctions, sharp maximum-critical-current enhancements are clearly observed at $H_a \neq 0$, which can only be achieved from interference effects in junctions containing regions with 'negative' critical current densities (π-facets). Using low temperature scanning electron microscopy imaging experiments performed at the Universität Tübingen in the group of Prof. D. Koelle, these 'negative' critical currents were clearly observed. All of these experimental results provide additional evidence for a predominant $d_{x^2-y^2}$-wave order parameter symmetry in the $YBa_2Cu_3O_{7-\delta}$. Additionally, the highly symmetric magnetic field dependencies of the critical currents of these zigzag junctions indicate that there is only a small, if any, subdominant imaginary s-wave admixture to the $d_{x^2-y^2}$-wave order parameter symmetry.

Apart from demonstrating the experimental realization of high-quality complex Josephson-arrays comprising the high-T_c cuprate $YBa_2Cu_3O_{7-\delta}$, the zigzag Josephson junctions were shown to be viable structures to resolve controversial issues re-

garding the pairing symmetry in the high-T_c cuprate superconductors. This was demonstrated by the order parameter symmetry test experiments performed based on $Nd_{2-x}Ce_xCuO_{4-y}$/Au/Nb zigzag junctions.

The anomalous magnetic field dependencies of the critical currents for $Nd_{2-x}Ce_xCuO_{4-y}$/Au/Nb zigzag junctions, which presented similar patterns to $YBa_2Cu_3O_{7-\delta}$/Au/Nb zigzag junctions, provide clear evidence for a predominant $d_{x^2-y^2}$ pairing symmetry in the $Nd_{2-x}Ce_xCuO_{4-y}$. This corroborates the conclusions of studies performed with grain boundary junctions in the optimally doped compounds.

To verify various recent reports on possible order parameter changes with over-doping and with decreasing temperature in various electron-doped high-T_c cuprates, the influence of those parameters has also been investigated for the electron-doped $Nd_{2-x}Ce_xCuO_{4-y}$ compound. The results indicated that no change in the symmetry was observed when over-doping the $Nd_{2-x}Ce_xCuO_{4-y}$ compound. Further, the order parameter symmetry was found to remain unaltered between $T = 1.6$ K and $T = 4.2$ K. Because of the larger J_c's as compared to grain boundary junctions, the cuprate-Nb zigzag configuration presents a good instrument for further detailed order-parameter symmetry test experiments. It will be interesting to extend the studies to other electron-doped compounds such as $Pr_{2-x}Ce_xCuO_{4-y}$ and $La_{2-x}Ce_xCuO_{4-y}$.

Another interesting aspect of the zigzag junctions is that for facet lengths a in the wide limit, *i.e.*, $a \gg \lambda_J$, the lowest-energy ground state of the system is characterized by a spontaneous generation of a half-integer magnetic-flux quantum at each corner. The spontaneously-generated half-integer magnetic-flux quanta in zigzag junctions were imaged using a scanning SQUID microscope at the IBM T.J. Watson Research Center by Dr. John Kirtley. The obtained images showed clearly a spontaneously induced magnetic flux at every corner of the zigzag junctions. Within the accuracy of the experiment, the magnitude of the flux was calibrated to be $\frac{1}{2}\Phi_0$ at each corner. The spontaneous fluxes were very well antiferromagnetically ordered. This antiferromagnetic ordering was found to be very robust, occurring for many cool-downs and for different samples with comparable geometries.

Simply put, because of the relationship between the enclosed flux and the quantum-phase in a superconductor ring, the half-integer magnetic-flux quanta provide a further π-phase change between neighboring facets, either adding or subtracting to the $d_{x^2-y^2}$-wave-induced π-phase-shifts, depending on the half magnetic-flux quantum polarity. In both cases this leads to a lowering of the Josephson coupling energy. The antiferromagnetic ordering sets in and freezes in during the cooling down process when $\lambda_J \sim a$. At this period, the perfect antiferromagnetic ordering is expected to cost the lowest energy for the system.

In the above-mentioned experiments, the ordering of the half-integer magnetic flux-quanta occurs in a singly connected superconducting system. To study the magnetic coupling between the half magnetic-flux quanta, electrically isolated Josephson structures have been realized. Similar to connected structures, a preferentially antiferromagnetic ordering of half-integer magnetic-flux quanta was also observed for electrically isolated structures, when sufficiently closely spaced. This presents an analogue to the antiferromagnetic Ising-spin system, and opens a possibility to realize various two-dimensional Ising antiferromagnetic systems.

The first two-dimensional Ising system was realized in a triangular configuration. This geometry is of particular interest, as with preferential antiferromagnetic coupling between the half-integer magnetic-flux quanta, it provides a model example of a strongly frustrated system, characterized by a high-entropy, highly degenerate ground state. Until now, such systems have been studied, *e.g.*, with arrays of all low-T_c superconducting rings biased at an externally applied magnetic flux of $\frac{1}{2}\Phi_0$ per ring and with low-T_c Josephson junction arrays. Fluctuations in the dimensions of those rings, resulting in variations in the flux bias and a lifting of the degeneracy, have been found to be a major complication in these investigations. The $d_{x^2-y^2}$-wave-induced spontaneously-generated flux provides an advantage in this respect, as the two flux-states are intrinsically degenerate. This was demonstrated by the fact that, although the systems with spontaneously generated half-flux quanta were realized from elements which were placed much further apart, they have higher antiferromagnetic bond-order parameters than the systems with conventional rings. The observed disorder in the triangular array may partly be due to the geometric frustration effect, and partly to the dynamical disorder effects.

The natural way to investigate the existence of Néel long range order in two dimensional Ising systems is to put the spins onto lattices of an unfrustrated geometry. For this reason, coupling of the half magnetic-flux quanta was also investigated on unfrustrated geometries, such as the square and honeycomb lattice. Although no Néel long range ordering was observed for a larger area in the square and honeycomb lattice, there are nice antiferromagnetic orderings on some separated areas. A complete Néel long range order might have been hampered by the dynamic disorder.

The possibility of manipulating the polarities of individual half magnetic-flux quanta has also been demonstrated. The manipulation was done by locally applying a magnetic field, enabling the possibilities of storing information or of constructing desired patterns of half magnetic-flux quanta.

Finally, the work described in this thesis will provide a diverse basis for both fundamental studies and potential applications, including further investigations on details of the order parameter symmetry in the high-T_c cuprates, half-integer magnetic-flux quantum effects, correlation in two-dimensional Ising models, and to realize the theoretically proposed elements for superconducting (quantum) electronics such as complementary Josephson circuits and qubits.

Samenvatting

Gebruikmakend van dunne-laag 'ramp-type' Josephson contacten tussen een hoge-T_c en een lage-T_c supergeleider zijn experimenten mogelijk gemaakt om $d_{x^2-y^2}$-geïnduceerde π-faseverschuivingseffecten in planaire Josephson arrays te bestuderen. De gepresenteerde studies omvatten de eerste experimentele realisatie van verscheidene complexe Josephson arrays met ingebouwde π-faseverschuivingen, onderzoek van de ordeparametersymmetrie in verscheidene hoge-T_c koperoxide supergeleiders, de eerste directe afbeelding van $d_{x^2-y^2}$-geïnduceerde Josephson tegenstroom, en magnetische halve flux quantum effecten in één- en twee-dimensionale arrays.

Het wordt algemeen aangenomen dat de hoge-T_c koperoxide supergeleider $YBa_2Cu_3O_{7-\delta}$ een $d_{x^2-y^2}$ ordeparametersymmetrie heeft. Om die reden waren de eerste Josephson arrays waarvoor de $d_{x^2-y^2}$-geïnduceerde π-faseverschuivingseffecten werden bestudeerd tussen de hoge-T_c koperoxide supergeleider $YBa_2Cu_3O_{7-\delta}$ en de lage-T_c supergeleider Nb. Het onderzoek is eerst uitgevoerd voor Josephson arrays met een zigzag configuratie. In deze structuur induceert de $d_{x^2-y^2}$ orde-parameter van het $YBa_2Cu_3O_{7-\delta}$ een verschil π in de Josephson faseval ϕ over de $YBa_2Cu_3O_{7-\delta}$-Nb barrière voor aangrenzende facetten.

Eén van de aspecten van de zigzag juncties die in het bijzonder interessant is wordt gevormd door de magneetveld-afhankelijkheid van de kritische stroom. Voor facetlengtes a in de kleine limiet, d.w.z., $a \ll \lambda_J$, met λ_J de Josephson penetratiediepte, toont de magneetveld-afhankelijkheid van de kritische stroom voor dit type juncties een afwijkend patroon. Er bevindt zich bij nul magneetveld geen maximum noch een afnemende enveloppe van de kritische stroom. In sterk contrast met de standaard Fraunhofer-achtige magneetveld-afhankelijkheid van de kritische stroom voor conventionele Josephson juncties worden scherpe kritische stroom maxima waargenomen bij $H_a \neq 0$, hetgeen alleen bereikt kan worden door interferentie-effecten in juncties die 'negatieve' kritische stroomdichtheden bevatten (π-facetten). Gebruikmakend van lage temperatuur scanning electron microscopy uitgevoerd aan de Universität Tübingen zijn deze 'negatieve' kritische stromen duidelijk waargenomen. Al deze experimentele resultaten bieden aanvullend bewijs voor een overheersende $d_{x^2-y^2}$ ordeparametersymmetrie in het $YBa_2Cu_3O_{7-\delta}$. Tevens geven de zeer symmetrische magneetveld-afhankelijkheden van de kritische stromen van deze zigzag juncties een indicatie dat als er al een imaginaire s component is naast de $d_{x^2-y^2}$ ordeparametersymmetrie, deze slechts klein en ondergeschikt is.

Behalve het demonstreren van de experimentele realisatie van complexe Josephson arrays van hoge kwaliteit met de hoge-T_c supergeleider $YBa_2Cu_3O_{7-\delta}$, zijn de

zigzag Josephson juncties geschikte structuren gebleken om controversiële onderwerpen met betrekking tot de paringssymmetrie in de hoge-T_c koperoxide supergeleiders op te lossen. Dit is gedemonstreerd door de uitgevoerde ordeparametersymmetrie test experimenten gebaseerd op $Nd_{2-x}Ce_xCuO_{4-y}$/Au/Nb zigzag juncties.

De afwijkende magneetveld-afhankelijkheden van de kritische stromen voor $Nd_{2-x}Ce_xCuO_{4-y}$/Au/Nb zigzag juncties, die met de $YBa_2Cu_3O_{7-\delta}$/Au/Nb zigzag juncties vergelijkbare patronen vertoonden, leveren duidelijk bewijs voor een overheersende $d_{x^2-y^2}$ paringssymmetrie in het $Nd_{2-x}Ce_xCuO_{4-y}$. Dit versterkt de conclusies van studies die uitgevoerd zijn met korrelgrensjuncties in de optimaal gedoteerde samenstellingen.

Om de verscheidene recente meldingen van mogelijke ordeparameter veranderingen met overdotering en met afnemende temperatuur in verschillende elektron-gedoteerde hoge-T_c koperoxides te verifiëren is de invloed van deze parameters ook onderzocht voor de elektron-gedoteerde samenstelling $Nd_{2-x}Ce_xCuO_{4-y}$. De resultaten gaven geen indicatie voor een verandering in de symmetrie wanneer de samenstelling $Nd_{2-x}Ce_xCuO_{4-y}$ wordt overgedoteerd. Verder werd gevonden dat de ordeparametersymmetrie onveranderd blijft tussen $T = 1.6$ K en $T = 4.2$ K. Vanwege de grotere J_c's in vergelijking met korrelgrensjuncties leent de koperoxide-Nb zigzag configuratie zich als een goed instrument voor verdere gedetailleerde ordeparametersymmetrie test experimenten. Het zal interessant zijn om de studies uit te breiden naar andere elektron-gedoteerde samenstellingen zoals $Pr_{2-x}Ce_xCuO_{4-y}$ en $La_{2-x}Ce_xCuO_{4-y}$.

Een ander interessant aspect van de zigzag juncties is dat voor facetlengtes a in de grote limiet, d.w.z., $a \gg \lambda_J$, de laagste energietoestand van het systeem gekarakteriseerd wordt door de spontane opwekking van een magnetisch halve flux quantum op elke hoek. De spontaan opgewekte magnetische halve flux quanta in zigzag juncties zijn vastgelegd door gebruik te maken van een scanning SQUID microscoop in het IBM T.J. Watson onderzoekscentrum door Dr. John Kirtley. De verkregen afbeeldingen toonden duidelijk een spontaan geïnduceerde magnetische flux op elke hoek van de zigzag juncties. Binnen de nauwkeurigheid van het experiment werd de grootte van de flux gecalibreerd op $\frac{1}{2}\Phi_0$ voor elke hoek. De spontane fluxen waren erg goed antiferromagnetisch geordend. Deze antiferromagnetische ordening bleek erg robuust te zijn en trad op voor veel afkoelingen en voor verschillende samples met vergelijkbare geometrieën.

Simpel gezegd leveren de magnetische halve flux quanta een verdere π-faseverschuiving tussen aangrenzende facetten vanwege de relatie tussen de ingevangen flux en de quantum-fase in een supergeleidende ring die opgeteld dan wel afgetrokken moet wonder van de $d_{x^2-y^2}$-geïnduceerde π-faseverschuivingen, afhankelijk van de polariteit van het halve magnetische flux quantum. In beide gevallen leidt dit tot een verlaging van de Josephson koppelings-energie. De antiferromagnetische ordening begint en bevriest tijdens het afkoelproces als $\lambda_J \sim a$. Tijdens deze periode wordt verwacht dat de antiferromagnetische ordening de laagste energietoestand van het systeem vormt.

In bovengenoemde experimenten vindt de ordening van de magnetische halve fluxquanta plaats in een enkelvoudig verbonden supergeleidend systeem. Om de magnetische koppeling tussen de halve magnetische flux quanta te bestuderen zijn elektrisch geïsoleerde Josephson structuren gerealiseerd. Net als bij de verbonden structuren

werd ook bij de elektrisch geïsoleerde structuren een voorkeur voor antiferromagnetische koppeling van magnetische halve flux quanta geöbserveerd, als deze dicht genoeg bij elkaar lagen. Dit biedt een analagon voor het antiferromagnetische Ising-spin systeem, en opent een mogelijkheid om verscheidene twee dimensionale Ising antiferromagnetische systemen te realiseren.

Het eerste twee-dimensionale Ising systeem werd gerealiseerd in een driehoekige configuratie. Deze geometrie is in het bijzonder interessant, want met een voorkeur voor antiferromagnetische koppeling tussen de magnetische halve flux quanta biedt dit een modelvoorbeeld van een sterk gefrustreerd systeem, gekarakteriseerd door een hoog-entropische, hoog ontaarde grondtoestand. Eerder werden dergelijke systemen bijvoorbeeld bestudeerd met arrays van lage-T_c supergeleidende ringen gebiased op een externe magnetische flux van $\frac{1}{2}\Phi_0$ per ring en met lage-T_c Josepshon junctie arrays. Fluctuaties in de dimensies van die ringen, resulterend in variatie in de flux bias en een opheffen van de ontaarding, zijn een groot probleem gebleken in deze studies. De $d_{x^2-y^2}$-geïnduceerde spontaan gegenereerde flux biedt een voordeel in dit opzicht, want de twee flux-toestanden zijn intrinsiek ontaard. Dit is gedemonstreerd door het feit dat hoewel de systemen met spontaan gegenereerde halve flux quanta gerealiseerd waren door elementen die veel verder uit elkaar geplaatst waren, ze hogere antiferromagnetische bond-ordeparameters hebben dan de systemen met conventionele ringen. De waargenomen wanorde in het driehoekige array is misschien deels door het geometrische frustratie effect, en deels het gevolg van de dynamische wanorde effecten.

De natuurlijke manier om het bestaan van Néel lange afstand ordering in twee-dimensionale Ising systemen te onderzoeken is de spins in roosters van een ongefrustreerde geometrie te plaatsen. Om deze reden werd de koppeling van de halve magnetische flux quanta ook onderzocht voor ongefrustreerde geometrieën, zoals het vierkante en het honingraat rooster. Hoewel op een groter oppervlak in het vierkante en honingraat rooster Néel lange afstand ordening werd waargenomen zijn er mooie antiferromagnetische ordeningen waargenomen in enkele kleine gebieden. Een complete Néel lange afstand orde is misschien belemmerd door de dynamische wanorde.

De mogelijkheid om de polariteiten van individuele halve magnetische flux quanta te manipuleren is ook aangetoond. De manipulatie werd uitgevoerd door lokaal een magnetisch veld aan te brengen, waardoor de mogelijkheid werd gecreëerd om informatie op te slaan of gewenste patronen van halve magnetische flux quanta te construeren.

Tenslotte, zal het werk beschreven in dit proefschrift legt een diverse basis voor zowel fundamentele studies als potentiële toepassingen, waaronder verdere onderzoeken naar de details van de orde parameter symmetrie in de hoge-T_c koperoxides, magnetische halve flux quantum effecten, correlaties in twee dimensionale Ising modellen, en om de theoretisch voorgestelde elementen voor supergeleidende (quantum) electronica zoals complementaire Josephson cicuits en qubits te realiseren.

Acknowledgements

I have been working on this thesis for about four years now. Numerous colleges have shared their greatest virtues and supported me in one way or another in that period. Any gratitude that I can show to them, let me do it now. This list will have to be incomplete, so let me start by thanking those who unintentionally will not get mentioned here.

First of all, I would like to thank my promotors, Horst Rogalla and Hans Hilgenkamp, for giving me the opportunity to conduct my research work in their group, and for carefully reading through the draft version of this thesis and giving me valuable comments. I also would like to thank the other members of my graduation committee John Kirtley, Francesco Tafuri, Stephan van Gils, and Dave Blank for agreeing to serve in the committee and reading the final draft of the thesis.

I think it is entirely appropriate to acknowledge my greatest debt to Hans Hilgenkamp, since he has been extraordinarily generous and open-minded in sharing ideas and listening to problems, not only in my work, but also in my social life. I am also grateful to Hans for the very stimulating atmosphere that he has been able to create and maintain within our small task forces, and for his gentle but firm guidance. Hans has also been an indefatigable reader of the proofs and deserves many thanks for that.

My special thanks should be directed to Henk-Jan Smilde who has assisted me from the start. Almost all I know now about high-T_c-low-T_c contacts is due to his huge talent. Henk-Jan, thanks for showing me how to chisel samples.

I want to thank John Kirtley at IBM Yorktown Heights for the close and intense collaboration that has generated a large part of the results presented in this thesis. His excellent scanning SQUID microscopy studies and light-speed analyses have resulted in very exciting results. John, your 'Hold onto your socks' emails have made my years. In the same line, thanks to Dieter Kölle and his group in Tübingen for the LTSEM works.

I very gratefully acknowledge the enormous effort put in by numerous colleagues within the Low Temperature Group in my research. I am indebted to Frank Roesthuis and Dick Veldhuis who have been constant consultants on my technical or 'technicar' problems. It was Darminto who has stimulated us to continuously work on the NCCO compounds. Victor Leca was very helpful by providing us the overdoped-NCCO target. In XRD experiments, I have benefited from the time spent by Sybolt Harkema and Gerrit van Hummel. I am grateful to Harrie Steffens who always takes care of the Helium supplies, and to Ans Veenstra and Inke in de Wal for handling all the adminis-

trative matters, paper-work, and conference trips. For the occasional discussions and helps, I would like to thank also the late Gerrit Gerritsma, Martijn Podt, Dave Blank, Alexander Brinkman, Mark Huijben, Karthikeyan Shunmugavel, Kees Verwijs, Ingrid Oomen, Mathijn Dekkers, Alexander Golubov, Guus Rijnders, Verdran Vonk, Aico Troeman, Joska Broekmaat, and other staff members and graduate students.

I would like to acknowledge fruitful discussions with Roman Mints at Tel Aviv University, John Kirtley and Chang Tsuei at IBM Yorktown Heights, Christof Schneider at Augsburg University, Edwards Goldobin at Tübingen University, and John Free at Harvard University.

My gratitude should also '*in principle*' be addressed to Kees Verwijs who has meticulously translated the summary in Dutch, and for the nice trip to Ischia. Thanks to Karthikeyan Shunmugavel for reading part of my manuscript and correcting the English, and of course for all the snacks I found in your office. To my brother Yan Faizal, thanks for all your efforts to read my manuscript and correct my English during your highly-packed schedule and eye problems.

I am indebted to Pak Barmawi and Pak Pepen for earlier support.

I thank my family for supporting me from the distance, specially for continuously supplying the unforgettable delicious Padang cuisine to Enschede.

Being a foreigner living in the Netherlands, I appreciate very much the friendship I share with people in the Indonesian student organization and other Indonesian people in Enschede. *Terima kasih banyak buat semuanya.*

Finally, it would not have been possible for me to pass through this time without love and patience of *mijn liefde* Liza and *si kleintje* Rian; any bouquets that I have, therefore, I would like to share with you.

List of publications

International Refereed Journals:

- Ariando, D. Darminto, H.J.H. Smilde, V. Leca, D.H.A. Blank, H. Rogalla, H. Hilgenkamp, *Phase-sensitive order-parameter symmetry test experiments utilizing $Nd_{2-x}Ce_xCuO_{4-y}$/Nb zigzag junctions*,
to be published in **Phys. Rev. Lett.** (2005)

- H. Hilgenkamp, Ariando, H.J.H. Smilde, D.H.A. Blank, G. Rijnders, H. Rogalla, J.R. Kirtley, C.C. Tsuei, *Ordering and manipulation of the magnetic moments in large-scale superconducting π-loop arrays*,
Nature 422, 50 (2003)

- H.J.H. Smilde, Ariando, D.H.A. Blank, G.J. Gerritsma, H. Hilgenkamp, H. Rogalla, *d-wave induced Josephson current counterflow in $YBa_2Cu_3O_7$/Nb zigzag junctions*,
Phys. Rev. Lett. 88, 057004 (2002)

- H.J.H. Smilde, Ariando, H. Rogalla, H. Hilgenkamp, *Bistable superconducting quantum interference device with built-in switchable $\pi/2$ phase shift*,
Appl. Phys. Lett. 85, 4091 (2004)

- H.J.H. Smilde, Ariando, D.H.A. Blank, H. Hilgenkamp, H. Rogalla, *π-SQUIDs based on Josephson contacts between high-T_c and low-T_c superconductors*,
Phys. Rev. B 70, 024519 (2004)

- J.R. Kirtley, C.C. Tsuei, Ariando, H.J.H. Smilde, H. Hilgenkamp, *Antiferromagnetic ordering in arrays of superconducting π-rings*,
Submitted to **Phys. Rev. B**

- H.J.H. Smilde, A.A. Golubov, Ariando, G. Rijnders, J.M. Dekkers, S. Harkema, D.H.A. Blank, H. Rogalla, and H. Hilgenkamp, *Untwinned $YBa_2Cu_3O_7$ films: admixtures to $d_{x^2-y^2}$-wave by angle-resolved tunneling*,
Submitted to **Phys. Rev. Lett.**

- B. Chesca, D. Doenitz, T. Dahm, R. Huebener, D. Koelle, R. Kleiner, Ariando, H. Hilgenkamp, *Observation of Andreev bound states in $YBa_2Cu_3O_{7-\delta}$/Au/Nb ramp-type junctions*,
In preparation for **Phys. Rev. B**

- H. Susanto, S.A. van Gils, T.P.P. Visser, Ariando, H.J.H. Smilde, H. Hilgenkamp, *Static semifluxons in a long Josephson junction with π-discontinuity points*,
  Phys. Rev. B 68, 104501 (2003)

Popular Magazines:

- H. Hilgenkamp, H.-J. Smilde, Ariando, M. Crok, *Schrijven met magneetvelden*, **Natuur en Techniek**, June issue, 46-49 (2003)